Dissertation

# Synthesis and properties of magnetic and superconducting iron-compounds with layered structures

Bettina Alexandra Rendenbach

2021

Dissertation zur Erlangung des Doktorgrades

der Fakultät für Chemie und Pharmazie

der Ludwig-Maximilians-Universität München

# Synthesis and properties of magnetic and superconducting iron-compounds with layered structures

Bettina Alexandra Rendenbach

aus

München, Deutschland

2021

Erklärung

Diese Dissertation wurde im Sinne von §7 der Promotionsordnung vom 28. November 2011 von Herrn Prof. Dr. Dirk Johrendt betreut.

Eidesstattliche Versicherung

Diese Dissertation wurde eigenständig und ohne unerlaubte Hilfsmittel erarbeitet.

München, den 07.12.2021

Bettina Rendenbach

Dissertation eingereicht am 07.10.2021

1. Gutachter: Prof. Dr. Dirk Johrendt

2. Gutachter: PD. Dr. Constantin Hoch

Mündliche Prüfung am 30.11.2021

# Danksagung

Mein besonderer Dank gilt Herrn Prof. Dr. Dirk Johrendt für die Möglichkeit meine Doktorarbeit in seiner Arbeitsgruppe anzufertigen. Darüber hinaus möchte ich mich für die Freiheit bei der Umsetzung meiner Forschungsideen, für die förderlichen Fachgespräche und Anregungen zu diesen Themen, sowie für die Gelegenheit an Fachtagungen teilnehmen zu können, bedanken.

Herrn PD. Dr. Constantin Hoch danke ich herzlich für die Übernahme des Koreferats.

Darüber hinaus danke ich Herrn Prof. Dr. Wolfgang Schnick, Prof. Dr. Achim Hartschuh. Herrn Prof. Dr. Thomas Klapötke und Herrn Prof. Dr. Hans-Christian Böttcher. dafür, dass sie sich als Prüfer für mein Rigorosum zur Verfügung gestellt haben.

Ein großer Dank geht an Constantin Hoch und Timotheus Hohl für die Unterstützung und hilfreichen Tipps bei dem Aufbau der Elektrolysemethode. Ohne eure Hilfe wäre das Projekt nicht so schnell umsetzbar gewesen. Vielen Dank an Steffen Klenner und Rainer Pöttgen für die Aufnahmen und Interpretation der Mössbauer-Messungen. Des Weiteren möchte ich mich bei Tobias Rackl, Martin Weidemann und Valentin Weippert für die Messungen zahlreicher magnetischer Proben bedanken.

Meinen Praktikanten Martin Weidemann, Regina Gabler, Sebastian Ambach und Sebastian Klenk bin ich sehr dankbar für Ihre Mitarbeit an meiner Dissertation.

Einen großen Dank für das Korrekturlesen dieser Arbeit möchte ich aussprechen an, Eugenia Elzer, Timotheus Hohl, Arthur Haffner und Valentin Weippert.

Ich bedanke mich bei allen Mitgliedern des AK Johrendt, die ich in den vergangenen Jahren kennenlernen durfte und die den Arbeitsalltag stets bereichert haben: Peiqui Chen, Arthur Haffner, Catrin Löhnert, Ursula Pachmayr, Simon Peschke, Tobias Rackl, Rudolf Schönmann, Marlo Schöneich, Juliane Stahl, Martin Weidemann, Valentin Weippert für die herzliche Aufnahme in den Arbeitskreis, die stete Hilfsbereitschaft und die angenehme Arbeitsatmosphäre. Danke Arthur, dass du unsere Forschung mit deinen genialen Syntheseideen und deinem ausgezeichneten Musikgeschmack bereichert hast. Danke Juliane, dass du immer ein offenes Ohr für meine Fragestellungen hattest und ich in dir eine gute Freundin finden durfte. Danke Valentin für unsere entspannte Zeit im Büro und danke Muddi, dass du den Laden am Laufen hältst und uns immer bei allem unterstützt.

Ganz herzlich möchte ich mich bei allen aktuellen, ehemaligen und adoptierten Kollegen des Labors D2.049: Florian Binder, Jakob Blahusch, Leo Diehl, Arthur Haffner, Anna Hatz, Charlotte Koschnik, Olaf Alberto von Mankowski, Katalin Szendrei-Temesi, Stefan Trenker und Martin Weidemann, für die gute Stimmung, das immer offene Ohr für Fragestellungen und natürlich unsere Laborabende, die leider durch Corona immer weniger wurden, bedanken.

Ich bedanke mich außerdem bei den ehemaligen und aktuellen Mitgliedern der Arbeitskreise Schnick, Hoch und Lotsch für die entspannte Arbeitsatmosphäre, die viele schöne Erlebnisse, und die spannenden und hilfreichen Diskussionen in der Kaffeeküche.

Thomas Miller, Dieter Rau und Wolfgang Wünschheim danke ich dafür, dass sie für die verschiedensten Probleme immer eine Lösung parat hatten und ihre unentwegt geduldige Hilfe. Im Besonderen möchte ich mich bei Wolfgang für sein immer offenes Ohr und zahlreichen Hilfestellungen bei diversen Reparaturen der Huber Geräte ausdrücklich bedanken.

Vor allem möchte ich meiner Familie und meinen Freunden danken, die mich nicht nur während dieser Arbeit, sondern während des gesamten Studiums unterstützt haben. Ohne die lustigen Abende und Urlaube wäre die Zeit des Studiums und der Doktorarbeit nicht so schnell verflogen. Meiner Familie möchte für die finanzielle und emotionale Unterstützung danken. Vielen Dank für die aufbauenden Worte und offenen Ohren bei allerlei Herausforderungen.

Mein ganz spezieller Dank gilt Burkard für viel Verständnis, Geduld und Zuspruch während aller Unwegsamkeit, Hochs und Tiefs des Studiums und dieser Doktorarbeit. Auch dafür, dass ich mich immer auf Ihn verlassen kann.

“Our greatest glory is not in never falling, but in rising every time we fall.”

– Confucius

# Table of Contents

# 1. Introduction

"*What could we do with layered structures with just the right layers?*" asked Richard Feynman in his famous 1959 lecture, "*There's plenty of room at the bottom.*"[1] With the advent of potent atomic investigation and layered materials synthesis techniques, Nobel laureate Richard Feynman speculated on the multitude of new materials and chemical processes that could now be revealed. Since then low dimensional materials are an intensively researched class of the solid condensed matter research. This class is growing steadily and is explored voraciously due to their material properties like high conductivity and high mechanical strength.[2-3] An drastic increase in the number of compounds occurred especially since the discovery of graphene[4] and other two-dimensional (2D) materials, e.g., phosphorene[5], silicene[6], germanene[7], MXenes[8] and transition metal dichalcogenides (TMD)[9]. These materials can be used for a wide range of applications including energy storage and conversion[10-11], superconductors[12-13], and catalysts[14-15].

Oxides are one of the most explored compound classes due to their availability and stability. In contrast, chalcogenides and pnictides have reached less attention in the search for new compounds due to their natural lower abundance and their lower formation enthalpies. As an additional challenge, hydrolysis and oxidation must be avoided. In iron-based chalcogenides and oxyhalides van-der-Waals (vdW) forces can occur between the layers resulting in compounds with interesting properties like superconductivity.[13, 16-17] The study of such magnetic and electronic phenomena covers a large area in solid condensed matter research. The range of the effects includes superconductivity, magnetoresistance, metal-insulator transitions and ferromagnetism.

This thesis focuses on the synthesis and structural analysis of selected iron-based layered chalcogenide and oxyhalide compounds in conjunction with the characterisation of their magnetic and electronic properties. The main part of the thesis deals with the synthesis of FeSe-based structures by solid-state reactions at low temperatures or electrochemical intercalation and the analysis of their superconducting behaviour (see Chapter 2 and 3). The second part covers additional studies on the magnetic and electronic properties of the layered iron oxyhalide $CaFeO_2Cl$ (see Chapter 4) as the unique crystal structure suggests promising magnetic properties.

## 1.1 FeSe-based superconductors

Focusing on layered chalcogenides and pnictides, the interest in intercalation as a powerful tool for the fabrication and processing of 2D structures has risen strongly. Intercalation usually comprises the insertion of a guest molecule, a neutral or charged species, into a host lattice with weakly bonded layers.[18-19] It has aroused great interest for its manifold applications in transparent conductive films,[20] electrochromic materials[21] and inducing unconventional or topological superconductivity.[22-25] In neutral layered host materials, e.g., metal nitride halides (e.g., HfNCl, ZrNCl)[24, 26-27], metal oxychlorides (e.g., FeOCl)[28-29] and metal chalcogenides (e.g., $\beta$-FeSe)[30], the intercalation of positively charged species is eased by developing interactions with the outmost anion layers. This is possible because the negatively charged non-metal layers encapsulate the inner metal layers. The layered compounds are often held together by vdW forces, which decrease steadily with $1/r^6$. Over the years different intercalation methods have been established like liquid phase (e.g. hydrothermal reaction and solvent diffusion), the vapour phase, and electrochemical method (see Figure 1-1).

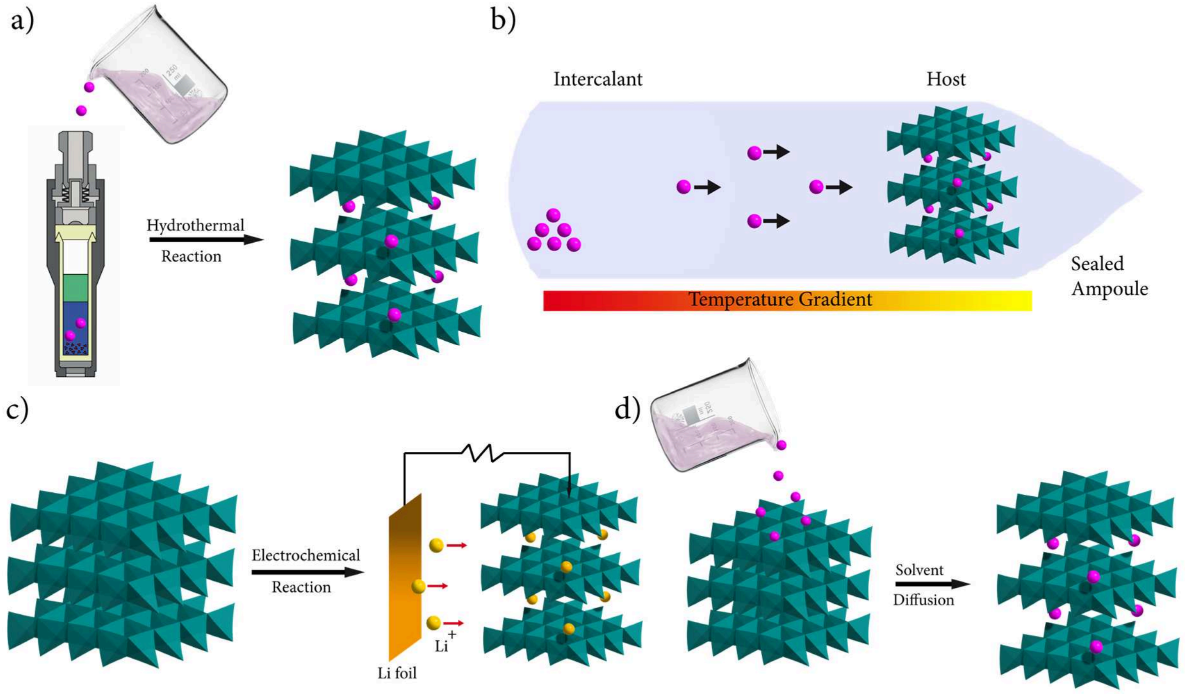

**Figure 1-1**. Various intercalation methods like **a**: hydrothermal intercalation, **b**: vapour phase intercalation, **c**: electrochemical intercalation and **d**: intercalation by solvent diffusion.

The vapour phase uses heat with a temperature gradient to control the intercalation either using isothermal or two-zone transport (see Figure 1-1b).[31-32] This method is known for the intercalation of alkaline metals in host materials such as graphene and TMD's.[31] For the liquid phase method the source can either be a solution containing intercalants (see Figure 1-1a and 1-1d) or the molten state of the intercalants itself. In particular, liquid ammonia, which dissolves alkaline and alkaline-earth metals, is used here to intercalate them into $MoS_2$[33] and black phosphorus[34]. The electrochemical method is a current or voltage driven intercalation process (see Figure 1-1c). This intercalation method is very beneficial, because the staging can be easily regulated by an external source (e.g., by controlling the electrochemical potential of the electrons in the host material) and allows direct observation of the stoichiometry of the intercalating compounds by chronopotentiometry or chronoamperometry.[35] A more detailed description of the electrochemical method, its theoretical considerations and synthesis parameters appears in Chapter 2.1.

Many intercalations processes intercalate lithium ions into layered materials due to the possibility to use these materials in large scales for lithium ion battery technology.[36] The intercalation of anions, such as sulfates or nitrates, play a minor role and examples are scarce.[37-38] In contrast to the anion intercalation, the intercalation of organic ions is quickly rising due to various advantages including the lower charge density (than alkaline ions) and possible low dimensional structures (large organic ion sizes).[39] Intercalation can also be successfully used for property tuning by effective and controlled electrical charge doping. The controllability makes the electrochemical intercalation a prime candidate for the tuning of superconducting properties of 2D materials. The superconducting research field is very extensive. However, this thesis is focused on intercalated FeSe-based superconductors.

The era of iron-based superconductors began with LaFeOP as the first superconducting iron-based material.[40] Kamihara discovered these fascinating characteristics in 2006 when studying its semiconducting properties. Until this discovery superconductivity of iron-based materials was largely ruled out because it was believed that the large magnetic moment of iron would be strong enough to disrupt the pairing of electrons responsible for superconductivity and that magnetism and superconductivity would be mutually exclusive. Following soon, a critical temperature of 26 K was observed in $La[O_{1-x}F_x]FeAs$ ($x = 0.05$–$0.12$)[41] and an even higher $T_c$ was reached in $Sm[O_{1-x}F_x]FeAs$ ($x = 0.1$; $T_c = 55$ K)[42]. These findings marked the beginning of a new era establishing a second class of unconventional high-temperature superconductors besides the cuprates.[43-44] Iron-based superconductors share some characteristics with the cuprate family including the layered crystal structure, the relatively high $T_c$ and inducing superconductivity by tuning parameters (e.g. chemical doping and pressure).

However, there are also significant differences. The doping of a Mott insulator induces the superconductivity in cuprates whereas the parent compound of the iron-based superconductors is a “poor metal”. In the pnictide and chalcogenide tetrahedra the anions are above and below the iron plane rather than in the plane like in copper oxide materials.[45] These differences indicate that our fundamental understanding of superconductivity still needs to be significantly revised. The discovery of new iron-based superconductors and a detailed analysis of their structural features contribute to further understanding of this phenomenon. The resulting intensive research has revealed two families: the iron pnictides (Fe*Pn*; *Pn* = As and P) and the iron chalcogenides (Fe*Ch*; *Ch* = S, Se and Te).[13, 30] Edge-sharing Fe$X_{4/4}$ ($X$ = *Pn* or *Ch*) tetrahedra layers are the common structural feature in both families. Various different interlayers separate the layers. Based on their crystal structure the compound classes can be categorized into 11, 111, 1111, 122 type, and some more. They are abbreviated by their stoichiometry (see Figure 1-2).

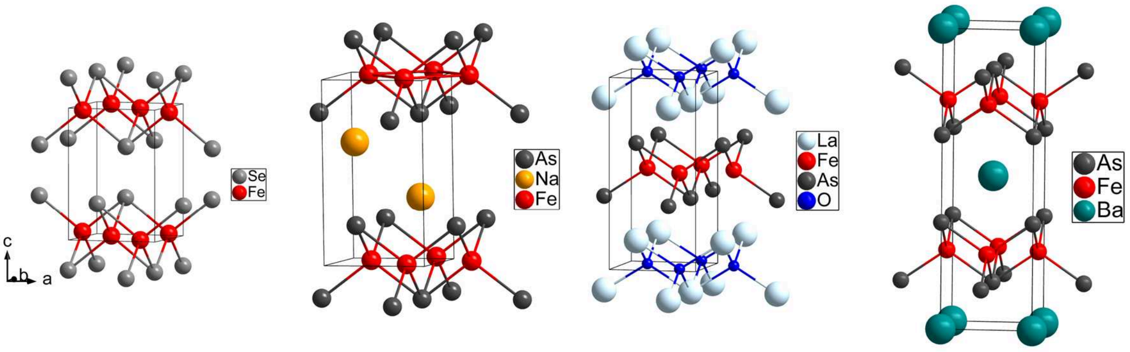

11
FeSe

111
NaFeAs

1111
LaFeAsO

122
$BaFe_2As_2$

**Figure 1-2.** Crystal structures of some iron-based superconductors.

The 11 type (Fe*Ch*; *Ch* = S-Te) is the simplest representative because it only consists of tetrahedra layers without any interlayer species.[30, 46-47] In the 111 type (*A*Fe*Pn*; *A* = alkaline metal) double layers of alkaline metals are located between the sheets.[48] The 1111 compounds (*RE*Fe*Pn*O, *RE* = rare-earth) adopt the ZrCuSiAs-type structure where edge-sharing tetrahedra layers (*anti*-PbO-type structure) alternate with slabs of rare-earth oxides tetrahedra with PbO-type structure. The 122 type ($AE\text{Fe}_2\text{As}_2$, $A\text{Fe}_2\text{As}_2$ and $A_x\text{Fe}_{2-y}Ch_2$; *A* = Na, K, Rb, Cs; *AE* = Ca, Sr, Ba) consists of single layers of alkaline or alkaline-earth cations between the tetrahedra layers.[49] This thesis focuses on the 11 type with its layers in *anti*-PbO structure type and 122 type related compounds.

In 2008 Hsu *et al.* discovered superconductivity in the layered structure $\beta$-FeSe ($T_c = 8$ K).[30] The parent compound is superconducting without doping or substitution. Over the years it has become clear that the superconducting properties of this structurally simple compound are not so easily explained and reproduced because the properties also depend on the synthesis method, the composition or reaction conditions.[50-51] The critical temperature can be increased to 37 K by external pressure[52], to values higher than 40 K through intercalation[53] and furthermore by ionic liquid gating[54] and potassium deposition[55]. The highest critical temperatures were reached by growing monolayer FeSe on $SrTiO_3$ substrate ($T_c$ exceeding 65 K).[56] High superconducting transition temperatures are also evident in alkaline intercalated FeSe-based superconductors by solid-state reactions such as $K_{0.8}Fe_2Se_2$[57] and $Rb_{0.88}Fe_{1.81}Se_2$[58]. First reported by Guo *et al.* they show that a critical temperature of 31 K can be reached by electron doping of FeSe.[59] However, $A_xFe_{2-y}Se_2$ (e.g. $A$ = K, Rb, Cs) compounds proved to be phase-separated and the nature of the actual superconducting fraction is still unclear.[58-60] Low temperature synthesis like the liquid ammonia method, hydrothermal, sonochemical or electrochemical syntheses allow access to metastable phases that cannot be achieved with high-temperature methods. Reactions in liquid ammonia have already proven successful. The reactions yielded compounds such as $A_x(NH_2)_y(NH_3)_{1-y}Fe_2Se_2$[61-63] or $A_x(NH_3)_yFe_2Se_2$[64-66] ($A$ = Li–Cs, Ca–Ba, Eu and Yb) with $T_c$ up to 46 K. Reactions using solvents like pyridine[67], ethylenediamine[68], hydrazine[69] or 1,3-propanediamine[70] led to $A_x(C_5H_5N)_yFe_{2-z}Se_2$ ($A$ = Li, Na, K, Rb), $Li_x(C_2H_8N_2)_yFe_2Se_2$, $Li_x(C_6H_{16}N_2)_yFe_{2-z}Se_2$ and $Li_x(C_3H_{10}N_2)_{0.32}FeSe$. The cointercalation of alkaline metals and amines drastically increased the $T_c$ which was attributed to the enlargement of the $c$-axis after intercalation e.g., in $Li_x(C_2H_8N_2)_yFe_2Se_2$ ($x = 0 \sim 0.8$; $T_c = 45$ K)[71]. For a long time, a direct correlation between the layer distance and the critical temperature was assumed. However, it became apparent that even at large layer spacing (55.7 Å), the critical temperature saturates around 45–50 K.[72-73] Electron doping, which occurs during the intercalation of cations, might be more crucial for higher superconducting transition temperatures.

A promising, but up to now scarcely implemented approach for the preparation of new compounds with FeSe layers is the electrochemical synthesis. In the last decade some headway was reached in the study of new superconductors with critical temperatures around 40±5 K by intercalating alkaline metals (Li, Na, and K) into $\beta$-FeSe *via* electrochemical synthesis.[74-78] Tuning the electric quantity controls the precise content of the inserted metals, which is advantageous over other methods (ammono-, hydro- and solvothermal). Challenges can arise by cointercalation of organic molecules, phase impurities and small superconducting volume fractions.[74-76] These challenges can partially circumvented by utilizing quaternary ammonium cations in contrast to alkaline ions. These cations usually have large diameters, as in the case of tetramethylammonium ($TMA^+$, 0.56 nm) or in tetraethylammonium ($TEA^+$, 0.67 nm).[79] Furthermore, quaternary ammonium cations are inert towards reduction at electrodes and have a wide electrochemical window.[79-80] The feasibility of intercalation of quaternary ammonium ions (cetyl-trimethylammonium ions ($CTA^+$)[81-82] and tetrabutylammonium ions ($TBA^+$)[83]) into layered $\beta$-FeSe single crystals was demonstrated by Shi *et al.* ($T_c$ up to 50 K). The interlayer distance of $TBA^+$ and $CTA^+$ intercalated materials were verified by TEM measurements, but the exact crystal structures have yet not been elucidated. A determination of the crystal structure may broaden the understanding of the chemistry behind these intercalated materials.

The main part of the thesis focuses on FeSe-based structures and superconductors that are synthesized by low temperature solid-state synthesis and electrochemical intercalation. With regard to electrolysis, this thesis presents in Chapter 2.1 the constructional and experimental work that went into the design and assembly of this fascinating method. The constructional and synthesis optimizations addressed the apparatus requirements, electrode material, solvent (electrolyte), supporting electrolyte and reactions conditions. We chose a galvanostatic electrolysis approach and the electrolysis chamber was equipped with a tungsten anode and mercury cathode. The constructional and tuning efforts led to a full functioning electrolysis setup in which new FeSe-based superconductors have been synthesized. In addition, the design has been adapted to increase the sample amount, which opens up the possibility to further analyse physical and magnetic properties.

Chapter 2.2 presents electrochemical synthesis of $(TMA)_{0.5}Fe_2Se_2$ and the determination of the ordered model of the intercalated compound validated by powder X-Ray diffraction and DFT calculations. It forms a derivative of $ThCr_2Si_2$ type structure, which is also known as the "122 type" in the family of iron superconductors. The properties and the composition are determined among others by elemental analysis, infrared spectroscopy and high temperature powder X-Ray diffractometry. The compound is characterised by magnetization and electrical resistivity measurements showing superconductivity with a critical temperature as high as 43 K. These results may pave the way to new intercalation products with potentially higher critical temperatures.

Chapter 3 focuses on the low temperature solid-state synthesis of [(Li,Fe)OH]FeSe. Lu *et al.* reported the hydrothermal synthesis of $LiFeO_2(FeSe)_2$ with alternating stacked layers of edge-sharing $FeSe_{4/4}$ tetrahedra and $Li_{0.5}Fe_{0.5}O$.[84] Later it was discovered that the compound is a hydroxide instead of an oxide.[53] After the successful hydrothermal route became known Hu *et al.* presented a low temperature solid-state route to $[(Li_{0.6}Fe_{0.4})OH]FeSe$.[85] This low temperature route opened up the possibility to new [(Li,Fe)OH]FeSe compounds as well as to similar layered compounds. In Chapter 3 the synthesis and analysis of non-superconducting $[(Li_{0.88}Fe_{0.12})OH]FeSe$ and $[LiOH](Fe)_zFeSe$ phases are presented. The analysis of the lithium occupation might explain the absence of superconductivity in $[(Li_{0.88}Fe_{0.12})OH]FeSe$. The possible reasons for the elongation of the lattice parameter $c$ in $[LiOH](Fe)_zFeSe$ were analysed by structural investigation. The phases expand the [(Li,Fe)OH]FeSe family and enlarge FeSe-based structure family.

## 1.2 Layered alkaline-earth iron oxyhalides

The layered oxide-based material class represent an area of research in solid-state and materials chemistry as well as solid-state sciences. These inorganic materials find wide applications in batteries[86-87], catalysts[88], magnets[89] and superconductors[90], thus contributing to the world's technological progress. An excellent example for fascinating oxide materials was the discovery of copper oxide superconductors, which led to a race to synthesize new inorganic materials as well as varying already known compounds to become superconducting.[40, 91-92] However, the discovery of new inorganic materials is becoming increasingly difficult because many combinations of elements have been nearly exhausted for oxides. The exchange or combination of anions offers new possibilities, as the choice of anion can also control structural and physical properties. This adds a completely new dimension to inorganic materials and a great versatility to their synthesis.

One of the new material classes are the mixed-anion compounds. They are mostly based on the fact that anions have specific characteristics such as ionic radius, electronegativity, valance state and polarizability and functional properties can be customized *via* insertion or exchange of a second anion.[93] Anion engineering focuses on combining the advantageous properties of individual anion species or on creating new phenomena by incorporating multiple anions in ordered arrangements.[94] In the literature, they are also described as heteroanionic compounds. Consequently it has been explored, how this technique can be applied to classes of compounds that are already of interest, especially as transition metal compounds.[95] To date, the main approach to tuning properties has been to vary the chemical composition or atomic structure of a known ternary oxide in bulk or thin film form by combining chemical substitution, geometric modifications, or external influences such as pressure or external fields.[94, 96] Anion engineering is less common in transition metal compounds. However, the incorporation of different anions in one compound enables researchers to synthesize compounds with physical and chemical properties and optical or electronic applications, which are not present in pure oxides, resulting for example in superconductivity in the LaFeAsO family.[97] Applications include energy conversion and catalysis[98], battery electrodes[99], thermoelectrics[100] and superconducting materials.[41, 101-102] Nevertheless, difficulties in the synthesis and the control of the anion distribution still present challenges and limit the studies of mixed anion compounds.[94] Among others oxyhydrides[103], oxychalcogenides[104], oxynitrides[94] and oxyhalides[105-107] emerge as new mixed anion compound classes (see Figure 1-3).

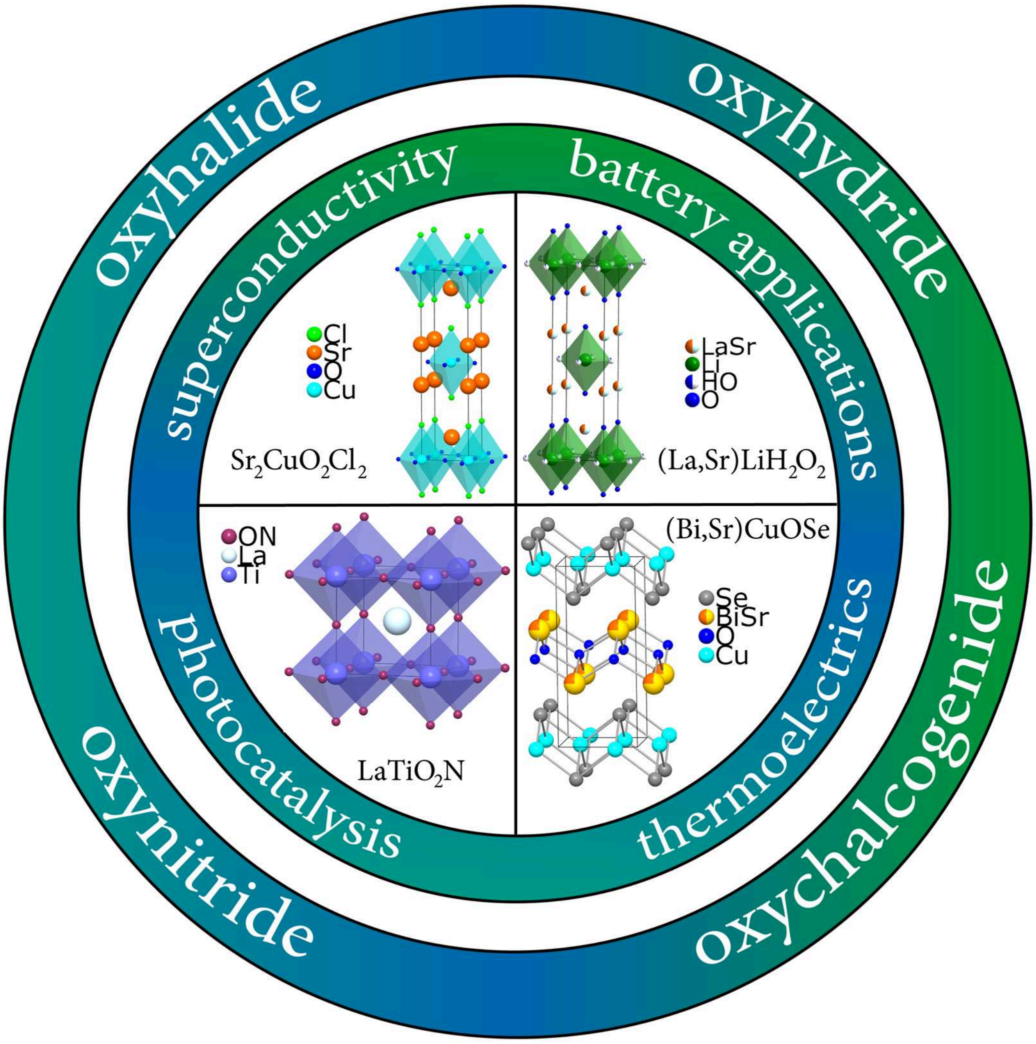

**Figure 1-3.** Overview of the mixed anion oxyhalide, oxyhydride, oxychalcogenide and oxynitride classes with examples for their typical structures, applications and special physical properties.[108-111]

For each class there are fascinating examples with outstanding properties such as pure hydride anion conductivity in $La_{2-x-y}Sr_{x+y}LiH_{1-x+y}O_{3-y}$ ($0 \leq x < 1$; $0 \leq y \leq 2$)[108]. Furthermore, more captivating properties are evident as promising thermoelectric materials in $Bi_{1-x}Sr_xCuSeO$ ($0 \leq x \leq 0.15$)[110], as superior electrochemical energy storage performance materials in *TM*ON (*TM* = Fe, Co, Ni, V)[112] and as superconducting materials in e.g., $Bi_3O_2S_2Cl$[106] and $Ca_{2-x}Na_xCuO_2Cl_2$ ($0 \leq x \leq 0.2$)[113]. An important feature of the transition metal oxyhalides is that these compounds exhibit anionically ordered structures in which the different anions are sequestered in separate layers, due to the large differences in size and polarizability between the oxide and halide anions.[114]

Considering the aforementioned properties, this thesis focuses also on oxyhalides, a layered new material class showing promising representatives with widely studied properties. Examples for this are the halooxocuprates with the 02($n$−1)$n$ structure $AE_2Ca_{n-1}Cu_n(O,X)_{2(n+1)+\delta}$ ($n$ = 1–5) and the 0222 structure $AELnCuO_3Cl$ ($AE$ = Ca, Sr, Ba; $Ln$ = Nd, Sm, Gd, Er) (superconductors)[115], $(CuCl)LaNb_2O_7$ (frustrated magnet)[116] and $Cu_2OCl_2$ (high-$T_c$ multiferroic)[117]. Together with some recently reported materials, such as $FeTe_2O_5X$ ($X$ = Cl, Br)[118], they show novel structures and special magnetic properties at low temperatures.[119-120] The group of the transition metal oxyhalides includes among others the following structural representatives: the $TMOX$ phases ($TM$ = Ti, V, Cr, Fe; $X$ = Cl, Br)[28, 121-123] and oxyfluorides (e.g., $(AE_{3-x}AE_x)MO_4F$ family ($AE$ = Sr, Ca, Ba; $M$ = Al, Ga; $0 \leq x \leq 1$)) like $(Sr,Ba)_{2.975}Ca_{0.025}AlO_4F$[124]. Furthermore, while concentrating on transition metal oxyhalides with alkaline-earth cations, the derivatives of the Ruddlesden-Popper phases or structural analogues to the $K_2NiF_4$-type phases (e.g., $AE_2FeO_3X$ ($AE$ = Ca, Sr; $X$ = F, Cl, Br)[120, 125] have been reported.

A part of the transition metal oxyhalide representatives is related to the Ruddlesden-Popper phases which took their beginning in oxide compounds with the synthesis and the characterization of the mixed metal oxide $Sr_3Ti_2O_7$ in 1958.[126] Since then, the class of Ruddlesden-Popper phases and its derivates has been growing steadily. The general formula is $A_{n+1}B_nX_{3n+1}$, where $A$ and $B$ stand for cations and $X$ for anions. The structures often consist of $n$ layers of $BX_6$ octahedra separated by layers of $AX$ assuming rock salt structure. The Ruddlesden-Popper phases derive from the parent perovskite phase by adding the $AX$ layer.

Phases with $n = \infty$ consist of an infinite number of corner sharing $BX_6$ octahedra layers and are analogous to the simple perovskite structure $ABX_3$. Figure 1-4 shows the structural similarity of perovskite and Ruddlesden-Popper phases by depicting structures $A_{n+1}B_nX_{3n+1}$ with $n$ = 1, 2, 3 and ∞. Members with $n = 1$ are also referred to as $K_2NiF_4$-structure type, e.g., $AE_2CuO_2X_2$ ($AE$ = Sr, Ca; $X$ = Cl, Br) where four oxide and two halide ions occupy the equatorial and apical sites of the octahedra, respectively.[127]

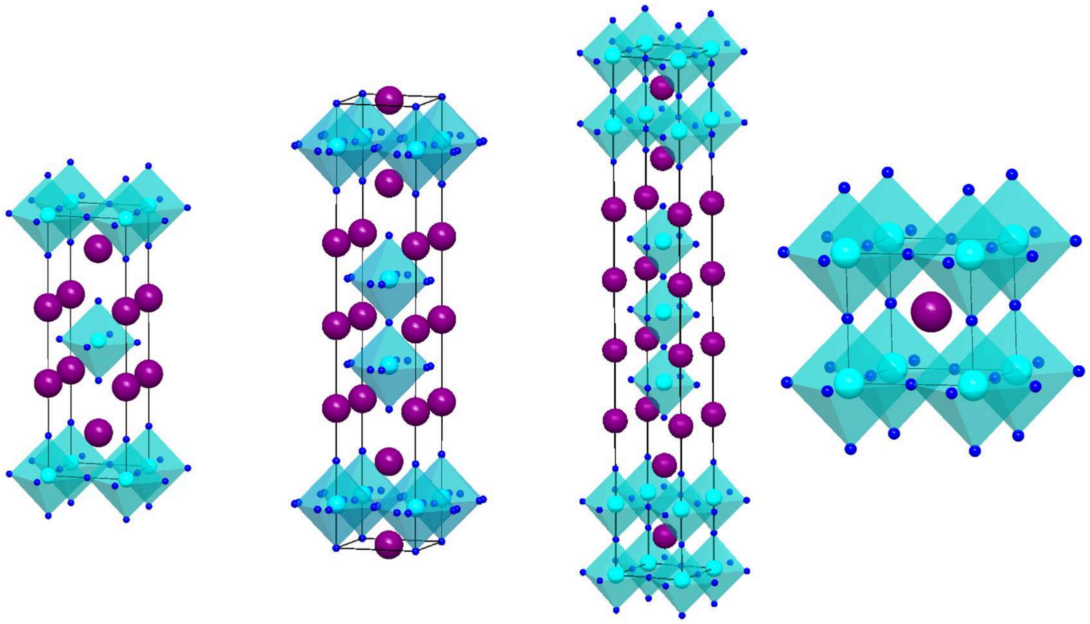

$n = 1$ $n = 2$ $n = 3$ $n = \infty$

**Figure 1-4.** Ruddlesden-Popper phases showing structures $A_{n+1}B_nX_{3n+1}$ with $n = 1, 2, 3$ and $\infty$ with the $A$ site in violet, the $B$ site in turquoise and the $X$ site in dark blue.

In most phases alkaline, alkaline-earth or rare-earth elements occupy the *A* site, whereas the *B* site consists usually of a transition metal. Ruddlesden-Popper phases are flexible not only regarding the cation substation, but also anion-doped phases are gathering more attention. Partial substitution by halogenides lead to the preparation of oxyhalides which initially has been successfully achieved for Cu compounds,[128] but later on as well for other transition metals.[129-130] In 1984 Leib and Müller-Buschbaum reported the first Ruddlesden-Popper alkaline-earth iron oxychloride, $Sr_3Fe_2O_5Cl_2$.[131]

The search for phases with first row transition metals expanded the oxyhalide chemistry, $Ca_2FeO_3Cl$ and $Sr_3Fe_2O_5Br_2$ reported by Ackerman,[132] and cobalt(II) phases $Sr_2CoO_2X_2$ ($X$ = Cl, Br) as well as manganese oxychlorides $Sr_2MnO_3Cl$.[129-130] These materials, especially iron oxyhalides with alkaline-earth cations, often adopt Ruddlesden-Popper and $K_2NiF_4$-type related structures where one or both of the apical oxygen of the perovskite block are exchanged for a halide. Changing the molar ratio (oxide : halide) from 2:2 to 3:1, the compounds show a square pyramidal coordination instead, e.g., $Sr_2FeO_3X$ ($X$ = F, Cl, Br).[125] The magnetic properties of some of the alkaline-earth iron oxyhalides have been increasingly investigated since the discovery of the superconductivity in copper-based oxyhalides.

Structural and magnetic investigations showed that in many $K_2NiF_4$-type oxyhalides, e.g., $Sr_2FeO_3X$ ($X$ = F, Cl, Br), the $La_2CuO_4$-type magnetic structure is favoured where the overall ferromagnetic moment is parallel to the planes.[125] The magnetic measurements of the oxyhalides showed antiferromagnetically ordered phases where $T_N$ is above 300 K. Only in the fluoride, the magnetic behaviour varies below 100 K resulting in a new magnetic structure type with a four-layer stacking arrangement.[120] The Ruddlesden-Popper related compounds $Sr_3Fe_2O_3X$ ($X$ = Cl, Br) show G-type antiferromagnetic spin structure where each iron moment aligns antiparallel to its five nearest neighbours.[133] A special case of layered transition metal alkaline-earth oxyhalides is the monoclinic $CaFeO_2Cl$. In contrast to most of the transition metal oxyhalogenides including the Ruddlesden-Popper phases, $CaFeO_2Cl$ contains corrugated layers of $FeO_{2/2}O_{3/3}$ square pyramids which are separated by CaCl-sheets in a way that no Fe-Cl contacts occur. The iron atoms build up a distorted honeycomb-lattice on the *ab*-plane (see Figure 1-5).

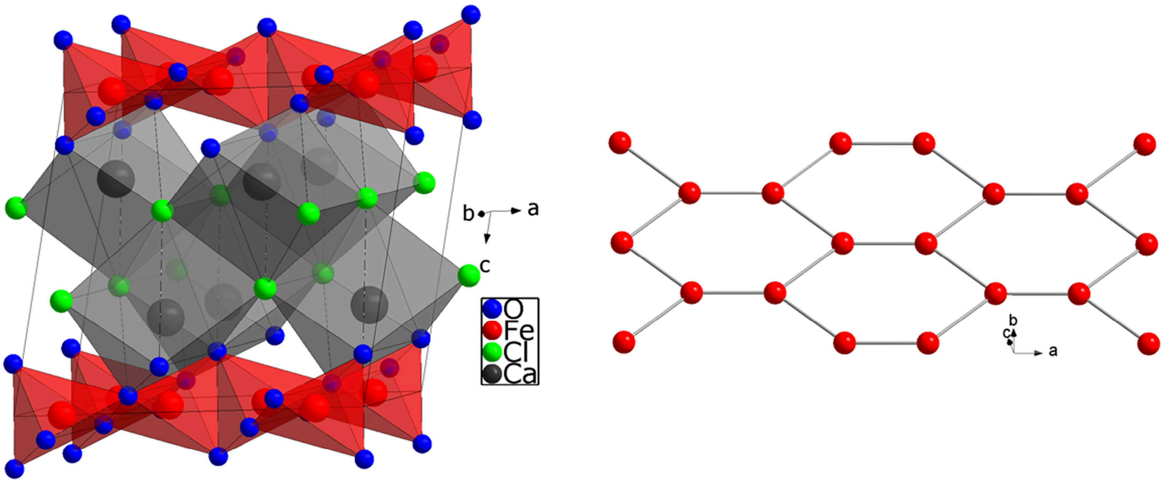

**Figure 1-5**. Crystal structure of $CaFeO_2Cl$ with layers of $FeO_{2/2}O_{3/3}$ square pyramids (red polyhedra) and the distorted honeycomb-lattice of the iron atoms.

Despite the extraordinary crystal structure of $CaFeO_2Cl$ the magnetic and physical properties of $CaFeO_2Cl$ are unknown so far. Therefore, Chapter 4 focuses on the optical and magnetic properties. There we report the successful synthesis and the validation of the crystal structure. Furthermore, magnetic measurements together with DFT calculations and Mössbauer measurements elucidate the magnetic properties of this antiferromagnetic Mott insulator. Based on these results, we propose a magnetic ordering pattern.

## 1.3 References

[1] R. Feynman, *Eng. Sci.* **1960**, *23:5*, 22–36.

[2] A. Raza, U. Qumar, J. Hassan, M. Ikram, A. Ul-Hamid, J. Haider, M. Imran, S. Ali, *Appl. Nanosci.* **2020**, *10*, 3875–3899.

[3] M.-C. Wang, C.-C. Huang, C.-H. Cheung, C.-Y. Chen, S. G. Tan, T.-W. Huang, Y. Zhao, Y. Zhao, G. Wu, Y.-P. Feng, H.-C. Wu, C.-R. Chang, *Ann. Phys.* **2020**, *532*, 1900452.

[4] K. S. Novoselov, A. K. Geim, S. V. Morozov, D. Jiang, Y. Zhang, S. V. Dubonos, I. V. Grigorieva, A. A. Firsov, *Science* **2004**, *306*, 666–669.

[5] M. Qiu, W. X. Ren, T. Jeong, M. Won, G. Y. Park, D. K. Sang, L.-P. Liu, H. Zhang, J. S. Kim, *Chem. Soc. Rev.* **2018**, *47*, 5588–5601.

[6] P. Vogt, P. De Padova, C. Quaresima, J. Avila, E. Frantzeskakis, M. C. Asensio, A. Resta, B. Ealet, G. Le Lay, *Phys. Rev. Lett.* **2012**, *108*, 155501.

[7] M. E. Dávila, L. Xian, S. Cahangirov, A. Rubio, G. Le Lay, *New J. Phys.* **2014**, *16*, 095002.

[8] J.-C. Lei, X. Zhang, Z. Zhou, *Front. Phys.* **2015**, *10*, 276–286.

[9] W. Zhang, Y. Zhang, J. Qiu, Z. Zhao, N. Liu, *InfoMat* **2021**, *3*, 133–154.

[10] B. Xu, S. Qi, M. Jin, X. Cai, L. Lai, Z. Sun, X. Han, Z. Lin, H. Shao, P. Peng, Z. Xiang, J. E. ten Elshof, R. Tan, C. Liu, Z. Zhang, X. Duan, J. Ma, *Chin. Chem. Lett.* **2019**, *30*, 2053–2064.

[11] P. Xiong, B. Sun, N. Sakai, R. Ma, T. Sasaki, S. Wang, J. Zhang, G. Wang, *Adv. Mater.* **2020**, *32*, 1902654.

[12] X. Geng, J. Yi, "The Development of High-Temperature Superconductors and 2D Iron-Based Superconductors" in *Nano-Sized Multifunctional Materials*, 1st ed. (Ed.: N. H. Hong), Elsevier, Amsterdam, Netherlands, **2019**, pp. 117–144.

[13] S. A. Rasaki, T. Thomas, M. Yang, *Prog. Solid State Chem.* **2020**, *59*, 100282.

[14] A. Kumar, Q. Xu, *ChemNanoMat* **2018**, *4*, 28–40.

[15] Y. Pan, R. Abazari, J. Yao, J. Gao, *Journal of Physics: Energy* **2021**, *3*, 032010.

[16] B. Rendenbach, T. Hohl, S. Harm, C. Hoch, D. Johrendt, *J. Am. Chem. Soc.* **2021**, *143*, 3043–3048.

[17] X. J. Wu, C. Q. Jin, P. Laffez, T. Tatsuki, T. Tamura, S. Adachi, H. Yamauchi, N. Koshizuka, *Physica C Supercond.* **1996**, *258*, 143–152.

[18] A. J. Jacobson, L. F. Nazar, "Intercalation Chemistry" in *Encyclopedia of Inorganic and Bioinorganic Chemistry* (Ed.: R. A. Scott), John Wiley & Sons, Ltd., Hoboken, New Jersey, USA, **2011**.

[19] R. Schöllhorn, "Materials and Models: Faces of Intercalation Chemistry" in *Progress in Intercalation Research* (Eds.: W. Müller-Warmuth, R. Schöllhorn), Springer Netherlands, Dordrecht, **1994**, pp. 1–81.

[20] J. Halim, M. R. Lukatskaya, K. M. Cook, J. Lu, C. R. Smith, L.-Å. Näslund, S. J. May, L. Hultman, Y. Gogotsi, P. Eklund, M. W. Barsoum, *Chem. Mater.* **2014**, *26*, 2374–2381.

[21] D. M. DeLongchamp, P. T. Hammond, *Chem. Mater.* **2004**, *16*, 4799–4805.

[22] L. A. Wray, S.-Y. Xu, Y. Xia, Y. S. Hor, D. Qian, A. V. Fedorov, H. Lin, A. Bansil, R. J. Cava, M. Z. Hasan, *Nat. Phys.* **2010**, *6*, 855–859.

[23] Y.-T. Hsu, A. Vaezi, M. H. Fischer, E.-A. Kim, *Nat. Commun.* **2017**, *8*, 14985.

[24] S. Yamanaka, K. Hotehama, H. Kawaji, *Nature* **1998**, *392*, 580–582.

[25] S. Yamanaka, T. Yasunaga, K. Yamaguchi, M. Tagawa, *J. Mater. Chem.* **2009**, *19*, 2573–2582.

[26] H. Kawaji, K. Hotehama, S. Yamanaka, *Chem. Mater.* **1997**, *9*, 2127–2130.

[27] S. Yamanaka, *J. Mater. Chem.* **2010**, *20*, 2922–2933.

[28] I. Kargina, D. Richeson, *Chem. Mater.* **1996**, *8*, 480–485.

[29] T. Yu, R. Yang, X. Zhao, X. Shen, *ChemElectroChem* **2019**, *6*, 1761–1767.

[30] F.-C. Hsu, J.-Y. Luo, K.-W. Yeh, T.-K. Chen, T.-W. Huang, P. M. Wu, Y.-C. Lee, Y.-L. Huang, Y.-Y. Chu, D.-C. Yan, M.-K. Wu, *Proc. Natl. Acad. Sci. U.S.A.* **2008**, *105*, 14262–14264.

[31] M. S. Stark, K. L. Kuntz, S. J. Martens, S. C. Warren, *Adv. Mater.* **2019**, *31*, 1808213.

[32] M. S. Dresselhaus, G. Dresselhaus, *Adv. Phys.* **2002**, *51*, 1–186.

[33] R. Zhang, I. L. Tsai, J. Chapman, E. Khestanova, J. Waters, I. V. Grigorieva, *Nano Lett.* **2016**, *16*, 629–636.

[34] R. Zhang, J. Waters, A. K. Geim, I. V. Grigorieva, *Nat. Commun.* **2017**, *8*, 15036.

[35] W. Müller-Warmuth, R. Schöllhorn, *Progress in Intercalation Research*, 1 ed., Springer Science & Business Media Dordrecht, Netherlands, **1994**, pp. 1–271.

[36] A. Manthiram, *Nat. Commun.* **2020**, *11*, 1550.

[37] V. V. Avdeev, O. A. Tverezovskaya, N. E. Sorokina, I. V. Nikol'skaya, A. I. Finaenov, *Inorg. Mater.* **2000**, *36*, 214–218.

[38] T. Placke, G. Schmuelling, R. Kloepsch, P. Meister, O. Fromm, P. Hilbig, H.-W. Meyer, M. Winter, *Z. Anorg. Allg. Chem.* **2014**, *640*, 1996–2006.

[39] C. Wan, X. Gu, F. Dang, T. Itoh, Y. Wang, H. Sasaki, M. Kondo, K. Koga, K. Yabuki, G. J. Snyder, R. Yang, K. Koumoto, *Nat. Mater.* **2015**, *14*, 622–627.

[40] Y. Kamihara, H. Hiramatsu, M. Hirano, R. Kawamura, H. Yanagi, T. Kamiya, H. Hosono, *J. Am. Chem. Soc.* **2006**, *128*, 10012–10013.

[41] Y. Kamihara, T. Watanabe, M. Hirano, H. Hosono, *J. Am. Chem. Soc.* **2008**, *130*, 3296–3297.

[42] Z.-A. Ren, W. Lu, J. Yang, W. Yi, X.-L. Shen, Z.-C. Li, G.-C. Che, X.-L. Dong, L.-L. Sun, F. Zhou, Z.-X. Zhao, *Chin. Phys. Lett.* **2008**, *25*, 2215.

[43] M. Rotter, M. Pangerl, M. Tegel, D. Johrendt, *Angew. Chem. Int. Ed.* **2008**, *47*, 7949–7952.

[44] G. Biswal, K. L. Mohanta, *Mater. Today Proc.* **2020**, *35*, 207–215.

[45] P. Carretta, G. Prando, *Riv. Nuovo Cimento* **2020**, *43*, 1–43.

[46] X. Lai, H. Zhang, Y. Wang, X. Wang, X. Zhang, J. Lin, F. Huang, *J. Am. Chem. Soc.* **2015**, *137*, 10148–10151.

[47] H. Ipser, K. L. Komarek, H. Mikler, *Monatsh. Chem.* **1974**, *105*, 1322–1334.

[48] D. R. Parker, M. J. Pitcher, P. J. Baker, I. Franke, T. Lancaster, S. J. Blundell, S. J. Clarke, *Chem. Commun.* **2009**, *16*, 2189–2191.

[49] P. Quebe, L. J. Terbüchte, W. Jeitschko, *J. Alloys Compd.* **2000**, *302*, 70–74.

[50] K. Zhou, J. Wang, Y. Song, L. Guo, J.-g. Guo, *Crystals* **2019**, *9*, 560.

[51] A. E. Böhmer, F. Hardy, F. Eilers, D. Ernst, P. Adelmann, P. Schweiss, T. Wolf, C. Meingast, *Phys. Rev. B* **2013**, *87*, 180505.

[52] S. Medvedev, T. M. McQueen, I. A. Troyan, T. Palasyuk, M. I. Eremets, R. J. Cava, S. Naghavi, F. Casper, V. Ksenofontov, G. Wortmann, C. Felser, *Nat. Mater.* **2009**, *8*, 630–633.

[53] U. Pachmayr, F. Nitsche, H. Luetkens, S. Kamusella, F. Brückner, R. Sarkar, H.-H. Klauss, D. Johrendt, *Angew. Chem. Int. Ed.* **2015**, *54*, 293–297.

[54] B. Lei, J. H. Cui, Z. J. Xiang, C. Shang, N. Z. Wang, G. J. Ye, X. G. Luo, T. Wu, Z. Sun, X. H. Chen, *Phys. Rev. Lett.* **2016**, *116*, 077002.

[55] C. H. P. Wen, H. C. Xu, C. Chen, Z. C. Huang, X. Lou, Y. J. Pu, Q. Song, B. P. Xie, M. Abdel-Hafiez, D. A. Chareev, A. N. Vasiliev, R. Peng, D. L. Feng, *Nat. Commun.* **2016**, *7*, 10840.

[56] J.-F. Ge, Z.-L. Liu, C. Liu, C.-L. Gao, D. Qian, Q.-K. Xue, Y. Liu, J.-F. Jia, *Nat. Mater.* **2015**, *14*, 285–289.

[57] J. G. Guo, S. F. Jin, G. Wang, S. C. Wang, K. X. Zhu, T. T. Zhou, M. He, X. L. Chen, *Phys. Rev. B* **2010**, *82*, 180520.

[58] A. F. Wang, J. J. Ying, Y. J. Yan, R. H. Liu, X. G. Luo, Z. Y. Li, X. F. Wang, M. Zhang, G. J. Ye, P. Cheng, Z. J. Xiang, X. H. Chen, *Phys. Rev. B* **2011**, *83*, 060512.

[59] J. Guo, S. Jin, G. Wang, S. Wang, K. Zhu, T. Zhou, M. He, X. Chen, *Phys. Rev. B* **2010**, *82*, 180520.

[60] A. Krzton-Maziopa, Z. Shermadini, E. Pomjakushina, V. Pomjakushin, M. Bendele, A. Amato, R. Khasanov, H. Luetkens, K. Conder, *J. Phys. Condens. Matter* **2011**, *23*, 052203.

[61] M. Burrard-Lucas, D. G. Free, S. J. Sedlmaier, J. D. Wright, S. J. Cassidy, Y. Hara, A. J. Corkett, T. Lancaster, P. J. Baker, S. J. Blundell, S. J. Clarke, *Nat. Mater.* **2012**, *12*, 15–19.

[62] F. R. Foronda, S. Ghannadzadeh, S. J. Sedlmaier, J. D. Wright, K. Burns, S. J. Cassidy, P. A. Goddard, T. Lancaster, S. J. Clarke, S. J. Blundell, *Phys. Rev. B* **2015**, *92*, 134517.

[63] S. J. Sedlmaier, S. J. Cassidy, R. G. Morris, M. Drakopoulos, C. Reinhard, S. J. Moorhouse, D. O'Hare, P. Manuel, D. Khalyavin, S. J. Clarke, *J. Am. Chem. Soc.* **2014**, *136*, 630–633.

[64] E.-W. Scheidt, V. R. Hathwar, D. Schmitz, A. Dunbar, W. Scherer, F. Mayr, V. Tsurkan, J. Deisenhofer, A. Loidl, *Eur. Phys. J. B* **2012**, *85*, 279.

[65] P. Shahi, J. P. Sun, S. H. Wang, Y. Y. Jiao, K. Y. Chen, S. S. Sun, H. C. Lei, Y. Uwatoko, B. S. Wang, J. G. Cheng, *Phys. Rev. B* **2018**, *97*, 020508.

[66] J.-H. Lee, T. Kakuto, K. Ashida, S. Shibasaki, T. Kambe, *AIP Adv.* **2018**, *8*, 065213.

[67] A. Krzton-Maziopa, E. V. Pomjakushina, V. Y. Pomjakushin, F. von Rohr, A. Schilling, K. Conder, *J. Phys. Condens. Matter* **2012**, *24*, 382202.

[68] Z. Gao, B. Zhu, H.-S. Xu, W. Xu, Q. Luo, K. Tang, *ChemistrySelect* **2019**, *4*, 8201–8206.

[69] S. Hosono, T. Noji, T. Hatakeda, T. Kawamata, M. Kato, Y. Koike, *J. Phys. Soc. Jpn.* **2015**, *85*, 013702.

[70] R.-J. Sun, S.-F. Jin, J. Deng, M.-N. Hao, L.-L. Zhao, X. Fan, X.-N. Sun, J.-G. Guo, L. Gu, *Chinese Phys. B* **2019**, *28*, 067401.

[71] L. Zhao, D. Wang, Q. Huang, H. Wu, R. Sun, X. Fan, Y. Song, S. Jin, X. Chen, *Phys. Rev. B* **2019**, *99*, 094503.

[72] C. Sakamoto, T. Noji, K. Sato, T. Kawamata, M. Kato, *J. Phys. Soc. Jpn.* **2020**, *89*, 115002.

[73] T. Hatakeda, T. Noji, K. Sato, T. Kawamata, M. Kato, Y. Koike, *J. Phys. Soc. Jpn.* **2016**, *85*, 103702.

[74] H. Abe, T. Noji, M. Kato, Y. Koike, *Physica C Supercond.* **2010**, *470*, S487–S488.

[75] T. Kajita, T. Kawamata, T. Noji, T. Hatakeda, M. Kato, Y. Koike, T. Itoh, *Physica C Supercond.* **2015**, *519*, 104–107.

[76] S.-J. Shen, T.-P. Ying, G. Wang, S.-F. Jin, H. Zhang, Z.-P. Lin, X.-L. Chen, *Chinese Phys. B* **2015**, *24*, 117406.

[77] A. M. Alekseeva, O. A. Drozhzhin, K. A. Dosaev, E. V. Antipov, K. V. Zakharov, O. S. Volkova, D. A. Chareev, A. N. Vasiliev, C. Koz, U. Schwarz, H. Rosner, Y. Grin, *Sci. Rep.* **2016**, *6*, 25624.

[78] Y. Cui, Z. Hu, J.-S. Zhang, W.-L. Ma, M.-W. Ma, Z. Ma, C. Wang, J.-Q. Yan, J.-P. Sun, J.-G. Cheng, S. Jia, Y. Li, J.-S. Wen, H.-C. Lei, P. Yu, W. Ji, W.-Q. Yu, *Chin. Phys. Lett.* **2019**, *36*, 077401.

[79] M. P. S. Mousavi, S. Kashefolgheta, A. Stein, P. Bühlmann, *J. Electrochem. Soc.* **2015**, *163*, H74–H80.

[80] J. S. Mayell, A. J. Bard, *J. Am. Chem. Soc.* **1963**, *85*, 421–425.

[81] M. Z. Shi, N. Z. Wang, B. Lei, C. Shang, F. B. Meng, L. K. Ma, F. X. Zhang, D. Z. Kuang, X. H. Chen, *Phys. Rev. Mater.* **2018**, *2*, 074801.

[82] J. P. Sun, M. Z. Shi, B. Lei, S. X. Xu, Y. Uwatoko, X. H. Chen, J. G. Cheng, *EPL-Europhys. Lett.* **2020**, *130*, 67004.

[83] M. Z. Shi, N. Z. Wang, B. Lei, J. J. Ying, C. S. Zhu, Z. L. Sun, J. H. Cui, F. B. Meng, C. Shang, L. K. Ma, X. H. Chen, *New J. Phys.* **2018**, *20*, 123007.

[84] X. F. Lu, N. Z. Wang, G. H. Zhang, X. G. Luo, Z. M. Ma, B. Lei, F. Q. Huang, X. H. Chen, *Phys. Rev. B* **2014**, *89*, 020507(R).

[85] G. B. Hu, N. Z. Wang, M. Z. Shi, F. B. Meng, C. Shang, L. K. Ma, X. G. Luo, X. H. Chen, *Phys. Rev. Mater.* **2019**, *3*, 064802.

[86] X. Zhang, Z. Wei, K. N. Dinh, N. Chen, G. Chen, F. Du, Q. Yan, *Small* **2020**, *16*, 2002700.

[87] Y. Liang, C.-Z. Zhao, H. Yuan, Y. Chen, W. Zhang, J.-Q. Huang, D. Yu, Y. Liu, M.-M. Titirici, Y.-L. Chueh, H. Yu, Q. Zhang, *InfoMat* **2019**, *1*, 6–32.

[88] G. P. Smestad, A. Steinfeld, *Ind. Eng. Chem. Res.* **2012**, *51*, 11828–11840.

[89] A. Okamoto, "The Invention of Ferrites and Their Contribution to the Miniaturization of Radios", *2009 IEEE Globecom Workshops*, **2009**, 1–6.

[90] J. G. Bednorz, K. A. Müller, *Z. Phys. B Condens. Matter* **1986**, *64*, 189–193.

[91] H. Takahashi, K. Igawa, K. Arii, Y. Kamihara, M. Hirano, H. Hosono, *Nature* **2008**, *453*, 376–378.

[92] M. K. Wu, J. R. Ashburn, C. J. Torng, P. H. Hor, R. L. Meng, L. Gao, Z. J. Huang, Y. Q. Wang, C. W. Chu, *Phys. Rev. Lett.* **1987**, *58*, 908–910.

[93] J. K. Harada, N. Charles, K. R. Poeppelmeier, J. M. Rondinelli, *Adv. Mater.* **2019**, *31*, 1805295.

[94] H. Kageyama, K. Hayashi, K. Maeda, J. P. Attfield, Z. Hiroi, J. M. Rondinelli, K. R. Poeppelmeier, *Nat. Commun.* **2018**, *9*, 772.

[95] Y. Tsujimoto, Y. Matsushita, N. Hayashi, K. Yamaura, T. Uchikoshi, *Cryst. Growth Des.* **2014**, *14*, 4278–4284.

[96] H. Kageyama, T. Yajima, Y. Tsujimoto, T. Yamamoto, C. Tassel, Y. Kobayashi, *Bull. Chem. Soc. Jpn.* **2019**, *92*, 1349–1357.

[97] M. Rotter, M. Tegel, D. Johrendt, *Phys. Rev. Lett.* **2008**, *101*, 107006.

[98] A. Miyoshi, K. Maeda, *Sol. RRL* **2020**, *5*, 2000521.

[99] D. Deng, *ChemNanoMat* **2017**, *3*, 146–159.

[100] R. Freer, A. V. Powell, *J. Mater. Chem. C* **2020**, *8*, 441–463.

[101] M. E. Arroyo y de Dompablo, E. Morán, M. Á. Alario-Franco, F. Drymiotis, A. D. Bianchi, Z. Fisk, *Int. J. Inorg. Mater.* **2000**, *2*, 581–588.

[102] M. Al-Mamouri, P. P. Edwards, C. Greaves, M. Slaski, *Nature* **1994**, *369*, 382–384.

[103] Y. Kobayashi, O. Hernandez, C. Tassel, H. Kageyama, *Sci. Technol. Adv. Mater.* **2017**, *18*, 905–918.

[104] S. J. Clarke, P. Adamson, S. J. C. Herkelrath, O. J. Rutt, D. R. Parker, M. J. Pitcher, C. F. Smura, *Inorg. Chem.* **2008**, *47*, 8473–8486.

[105] J. Olchowka, H. Kabbour, M. Colmont, M. Adlung, C. Wickleder, O. Mentré, *Inorg. Chem.* **2016**, *55*, 7582–7592.

[106] B.-B. Ruan, K. Zhao, Q.-G. Mu, B.-J. Pan, T. Liu, H.-X. Yang, J.-Q. Li, G.-F. Chen, Z.-A. Ren, *J. Am. Chem. Soc.* **2019**, *141*, 3404–3408.

[107] Y. Tsujimoto, K. Yamaura, N. Hayashi, K. Kodama, N. Igawa, Y. Matsushita, Y. Katsuya, Y. Shirako, M. Akaogi, E. Takayama-Muromachi, *Chem. Mater.* **2011**, *23*, 3652–3658.

[108] G. Kobayashi, Y. Hinuma, S. Matsuoka, A. Watanabe, M. Iqbal, M. Hirayama, M. Yonemura, T. Kamiyama, I. Tanaka, R. Kanno, *Science* **2016**, *351*, 1314–1317.

[109] H. Yang, Q. Liu, R. Yu, F. Li, C. Jin, *Supercond. Sci. Technol.* **2005**, *18*, 813–817.

[110] L. D. Zhao, D. Berardan, Y. L. Pei, C. Byl, L. Pinsard-Gaudart, N. Dragoe, *Appl. Phys. Lett.* **2010**, *97*, 092118.

[111] G. Lin, X. Xu, *ACS Sustain. Chem. Eng.* **2020**, *8*, 9641–9649.

[112] S. Wang, L. Li, Y. Shao, L. Zhang, Y. Li, Y. Wu, X. Hao, *Adv. Mater.* **2019**, *31*, 1806088.

[113] N. D. Zhigadlo, J. Karpinski, S. Weyeneth, R. Khasanov, S. Katrych, P. Wägli, H. Keller, *J. Phys. Conf. Ser.* **2008**, *97*, 012121.

[114] H. Wu, S. Pan, K. R. Poeppelmeier, H. Li, D. Jia, Z. Chen, X. Fan, Y. Yang, J. M. Rondinelli, H. Luo, *J. Am. Chem. Soc.* **2011**, *133*, 7786–7790.

[115] S. Adachi, T. Tatsuki, T. Tamura, K. Tanabe, *Chem. Mater.* **1998**, *10*, 2860–2869.

[116] A. A. Tsirlin, H. Rosner, *Phys. Rev. B* **2009**, *79*, 214416.

[117] L. Zhao, M. T. Fernández-Díaz, L. H. Tjeng, A. C. Komarek, *Sci. Adv.* **2016**, *2*, e1600353.

[118] R. Becker, M. Johnsson, R. K. Kremer, H.-H. Klauss, P. Lemmens, *J. Am. Chem. Soc.* **2006**, *128*, 15469–15475.

[119] E. Constable, S. Raymond, S. Petit, E. Ressouche, F. Bourdarot, J. Debray, M. Josse, O. Fabelo, H. Berger, S. deBrion, V. Simonet, *Phys. Rev. B* **2017**, *96*, 014413.

[120] A. L. Hector, C. S. Knee, A. I. MacDonald, D. J. Price, M. T. Weller, *J. Mater. Chem.* **2005**, *15*, 3093–3103.

[121] M. Lind, *Acta Crystallogr. Sec. B* **1970**, *26*, 1058–1062.

[122] X. Zhao, Z. Zhao-Karger, D. Wang, M. Fichtner, *Angew. Chem. Int. Ed.* **2013**, *52*, 13621–13624.

[123] P. Gao, M. A. Reddy, X. Mu, T. Diemant, L. Zhang, Z. Zhao-Karger, V. S. K. Chakravadhanula, O. Clemens, R. J. Behm, M. Fichtner, *Angew. Chem. Int. Ed.* **2016**, *55*, 4285–4290.

[124] S. Park, T. Vogt, *J. Phys. Chem. C* **2010**, *114*, 11576–11583.

[125] A. L. Hector, J. A. Hutchings, R. L. Needs, M. F. Thomas, M. T. Weller, *J. Mater. Chem.* **2001**, *11*, 527–532.

[126] S. N. Ruddlesden, P. Popper, *Acta Crystallogr.* **1958**, *11*, 54–55.

[127] H. Müller-Buschbaum, *Angew. Chem. Int. Ed.* **1977**, *16*, 674–687.

[128] Z. Hiroi, N. Kobayashi, M. Takano, *Nature* **1994**, *371*, 139–141.

[129] C. S. Knee, M. T. Weller, *J. Solid State Chem.* **2002**, *168*, 1–4.

[130] C. S. Knee, A. A. Zhukov, M. T. Weller, *Chem. Mater.* **2002**, *14*, 4249–4255.

[131] W. Leib, H. Müller-Buschbaum, *Z. Anorg. Allg. Chem.* **1984**, *518*, 115–119.

[132] J. F. Ackerman, *J. Solid State Chem.* **1991**, *92*, 496–513.

[133] C. S. Knee, M. A. L. Field, M. T. Weller, *Solid State Sci.* **2004**, *6*, 443–450.

# 2. Electrochemical intercalation of iron selenide

## 2.1 Theoretical considerations and experimental procedure

In 1800 Alessando Volta invented the first electric battery capable of supplying current to a circuit, initiating the era of electrochemistry.[1] In the same year Nicholson reported the decomposition of water into oxygen and hydrogen while applying a electric current, which is now considered the first electrochemical reaction.[2] Independent from each other Jöns Jacob Berzelius (1806) and Humphry Davy (1807) published their first electrolytic results based on Volta's achievements.[3-4] During this process they advanced Faraday's work on electricity.[5] Both utilized a liquid mercury pool on which common salts were dispersed as cathode. In the late 19th century preparative electrolysis gained momentum as an industrial process for the production of bulk chemicals on a multi-ton scale. Typical examples include the chlor-alkali[6-8] and the Hall-Héroult[9-10] process. Whereas the first encompasses the electrolysis of aqueous sodium chloride to yield chlorine gas and sodium hydroxide, the second process uses $Al_2O_3$ to produce elemental aluminium. Only in the last 30–40 years the number of publications and industrial applications have been increasing rapidly, as the sources for the electrical current became more reliable and the analytical methods improved drastically.[11] The increase is not only due to the enhancement of the equipment but also to the numerous advantages of the synthetic method. Reactive intermediates can be obtained from neutral precursors and precise regulation of the electric current allows an accurate control of the reaction. The method allows the avoidance of aggressive and hazardous reagents, mild reaction conditions, and the driving force of the reaction is the electrode potential instead of the thermodynamic control.[12] The main disadvantages are partially occurring inhomogeneities of the electrical field and limited lifetime of parts of the cell such as the electrodes, before being replaced at high costs. The field of electrochemistry is growing quickly and has applications in both organic[13-14] as well as inorganic[15-17] chemistry. Especially regarding intercalation into layered materials, the electrochemical synthesis has generated a big interest.[18-20] This intercalation method extends the interlayer spacer thus expanding this materials class with interesting properties such as supercapacitors[21], superconductors[22-23] and batteries[24]. For FeSe-based superconductors this synthetic approach has led to the successful intercalation of alkaline ions[25-26] like Li in $Li_x$FeSe[27] and organic ions[28-29] such as tetrabutylammonium ($TBA^+$) in $(TBA)_{0.3}$FeSe[28].

The following chapter introduces and discusses the prerequisites and limitations for the in this thesis successfully applied electrolysis. The chapter consists of a step-by-step experimental procedure, the apparative requirements, utilized electrodes, electrolyte composition, and reaction conditions.

### Detailed synthesis procedure

The electrolysis chamber (see Figure 2-1) was assembled while still hot, coming directly from a 100 °C drying oven, and was subsequently evacuated for 15 min (pressure $< 1 \cdot 10^{-3}$ mbar) and flooded with dry argon. These two steps were repeated three times. The argon was dried over molecular sieve (three Å) and $P_4O_{10}$. The continuously heated BTS catalyst (170 °C) removed traces of oxygen. An inert gas condition can be ensured for the filling and operation of the device by means of a Schlenk attachment to the chamber. The anode, a tungsten rod, as well as the cathode, an amalgamated copper spoon attached to a platinum wire, are each sealed in a glass tube. To avoid cathodic side reactions, it is essential that only the cathode material and not the connecting wires be in contact with the electrolyte. The respective iodide was dissolved in the dry solvent, here *N*,*N*-dimethyl formamide (DMF), in a Schlenk tube. DMF was purified and dried at elevated temperatures by distillation and degassing. Depending on the utilized alkylammonium iodide ($R_4N^+I^-$) different solubilities are apparent. For $R = CH_3$ the solution was heated up to 150 °C to dissolve the corresponding salt in dry DMF. When $R$ represents a longer chain, like in tetrabutylammonium iodide ($R = C_4H_9$), the salt can easily be dissolved by stirring for 30 min under Schlenk conditions at room temperature. The copper spoon was amalgamated with a solution of half-concentrated $HNO_3$ in which a drop of Hg was dissolved. Afterwards the amalgamated spoon was rinsed with ethanol and dried at room temperature. The for all synthetic steps utilized mercury was purified by filtering over a pleated filter to remove major physical impurities and treating it with half-concentrated $HNO_3$ to dissolve all less noble compounds. The solution was strongly stirred until it appeared colourless and insoluble $Hg_2(NO_3)_2$ was formed. All remaining impurities were removed by filtration and rinsed with distilled water. Subsequently it was distilled twice in vacuum at 120 °C. Under argon counter flow the FeSe crystals which were slightly ground in an agate mortar beforehand were dispersed on an Hg drop in the amalgamated spoon. The electrolyte was filled into the electrolysis apparatus through the anode chamber under an argon counter flow and the electrodes were installed. A terminal voltage of three to fifteen Volt can be applied for one to four days. In most syntheses, a voltage of three Volt and a duration of three to four days was chosen. At the end of the reaction, the solvent was extracted from the electrolysis chamber via purging with argon pressure from the Schlenk line. Successively the cathode was rinsed with new dry solvent, in this case dry DMF. The final product was subsequently loaded into an argon-filled Schlenk tube and then dried from residual DMF at high vacuum. Further preparation for analyses were executed in an argon-filled glovebox.

### Setup requirements and further development of the electrolysis

In collaboration with the group around PD Constantin Hoch the electrolysis chamber as shown in Figure 2-1 was constructed.[17] The electrolysis reaction depends on a variety of parameters which are also co-dependent such as redox potential, electrode materials and reaction conditions (electrolyte concentration, duration, current density).

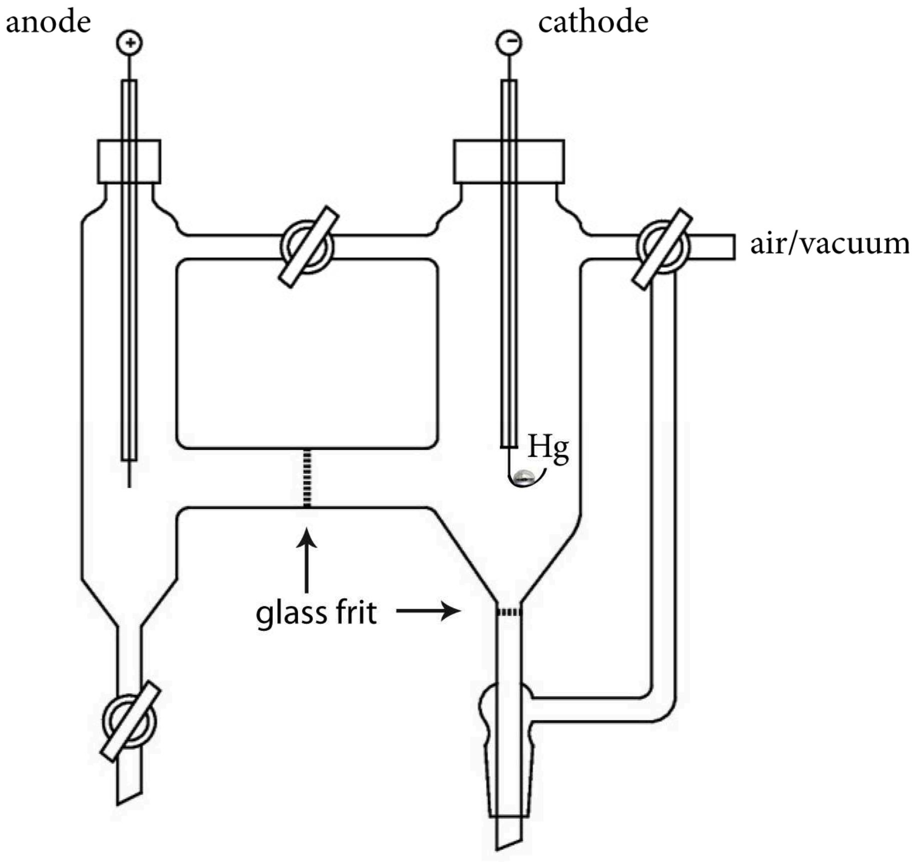

**Figure 2-1**. Schematic design of the electrolysis apparatus.

*Apparative requirements*

Two different electrolysis methods are known for preparative electrochemical reactions: the galvanostatic method, i.e. applying a constant voltage, and the potentiostatic method, maintaining a constant potential at the working electrode during the electrolysis.[30-31] During our electrolysis experiments, we applied a defined voltage, choosing the galvanostatic method. Hereby, the potential of the electrodes fluctuates while the voltage is maintained at a constant value (three to fifteen Volt). Our setup consists of a working electrode, a counter electrode and a power supply. This provides a simpler, more straightforward but less sophisticated approach compared to potential-controlled electrochemistry, as there is no feedback from the reference electrode to the potentiostatic electrode.[32] If no reactive species other than the desired one is present, more than 90% of the starting material converts.[33-34] Consequently, we chose this method even though the selectivity is lower, but usually the full conversion rate is faster. Additionally, the potentiostatic method requires a reference electrode and a more costly electronic periphery.[31] For future applications, the apparatus can be extended with a reference electrode and therefore enable the potentiostatic method. Thus, it would be possible to record both the terminal voltages and the actual electrode potentials. This procedure would provide a better and quantitative reaction control.[13, 35]

In the next step, the cell design had to be chosen. Simple cell designs, such as undivided cells, are strongly preferred to minimize laboratory efforts. However, anodic or cathodic transformations at their respective counter electrode limit these setups.[36] If the substrate, intermediates or the product are not stable toward the reaction in the counter chamber, separators have to be installed, which in turn leads to a significant voltage drop.[32] While choosing the separator materials one has to keep in mind that for a working cell a movement of the ions is essential and a passage of charge is a necessary requirement (anions from cathode to anode and/or cations from anode to cathode).[37] Materials can be non-functionalized glass, ceramic or polymer materials and more. As depicted in Figure 2-1, a glass frit was chosen as separator, which divides the cathode and anode compartments. It shows a good chemical resistance, but demonstrates a limited scalability. It separates the chemical process of both electrodes and suppresses non-desired diffusion to the counter electrode. For this electrolysis, the formation of the $I_3^-$ needs to be separated from the intercalation of $TMA^+$ into FeSe (shown in Figure 2-2).[35, 38] Since most FeSe-based superconductors are sensitive to hydrolysis and oxygen,[39-41] the apparatus was designed to operate under Schlenk conditions. The small glass frit beneath the cathode in the designed apparatus allows the separation of the product inside the chamber, the filtration of the remaining electrolyte solution and a washing step with purified solvent (see Figure 2-1 and Figure 2-2).

**Figure 2-2.** Electrolysis setup where the development of $I_3^-$, visible in the anode chamber (left), is separated with a glass frit during the electrolysis.

Most electrolysis reactions utilize room temperature and ambient pressure conditions.[42] However, our setup may also be enhanced with an additional jacket for constant and controllable reaction temperatures via an external thermostat. This would present future researchers broader varieties of reaction temperatures and thereby widen the possible field for new high-temperature iron-based superconductors.

*Electrode material*

The outcome of the reaction strongly depends on the material utilized for the electrodes.[43-44] While choosing the right material some aspects need to be considered such as physical and chemical stability as well as electrical conductivity.[32] Four different types of electrodes are often used in electrolysis: inert, active, high surface and sacrificial electrodes.[43, 45] The active ones are mostly used in conversions in which electron transfer is catalysed by immobilized high valence metal species generated by the electrodes. The species are regenerated by the electric current. Examples for these are nickel or molybdenum in fluorinated alcohols, NiOOH in alkaline media, or $PbO_2$ in acids.[46] High surface electrodes often consist of foams or mesh materials. Sacrificial electrodes are consumed during electrolysis. In most common setups, the electrodes must be structurally strong and chemically inert to the electrolyte as well as to reaction partners. These requirements are mostly met in noble metal anodes, such as platinum and gold.[31] Other anode materials are also described in literature such as carbon, lead oxide and nickel.[13, 47-48] When using platinum as anodic electrode in combination with an aprotic solvent, the product forms a tarry material, which electrically insulates the electrode from the solution by covering it. Therefore, the electrode needs to be cleaned and maintained to achieve a reproducible and clean electrode surface. Sometimes this might be avoided by using pulse electrolysis.[49] The corrosive effects of the electrolysis are less prominent for cathodes, which give rise to a bigger variety of possible materials such as lead, tin, platinum or mercury. The last was one is among the earliest in use.[50]

Under standard conditions mercury is a liquid and hence usable as electrode in various forms, such as the hanging mercury drop electrode (HMDE)[51-52], the dropping mercury electrode (DME)[53-54], the static mercury drop electrode (SMDE)[55], and the mercury film electrode (MFE)[56-57]. The advantages are the clean reproducible surface of the electrode, the low capacitance compared to other metals and its wide cathodic window.[58-59] But its liquid state also provides some restrictions originating from the difficulty of forming electrodes with the required geometry. However, this challenge can be circumvented with amalgamated copper electrodes. Furthermore, mercury electrodes have become less prominent in research and industrial applications due to the potential risk of poisoning and environmental contamination.[60] In some countries the use of mercury has been completely banned.[61] Still some of the benefits cannot be neglected and when the right safety measures have been taken, mercury is still an advantageous electrode to use.[62-63]

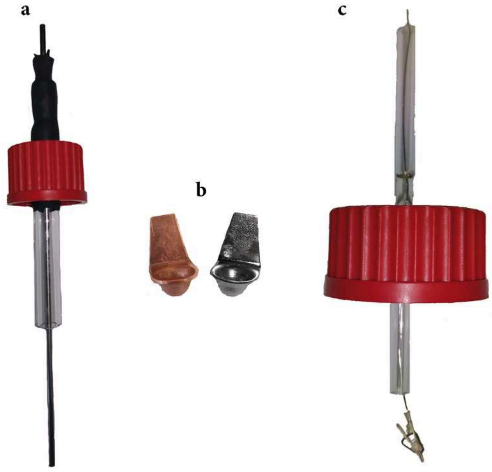

**Figure 2-3.** Electrode material used in the electrolysis. **a:** the tungsten anode; **b:** the copper spoon on the left and the amalgamated spoon on the right. **c:** the platinum electrode with a crocodile clip which connects the copper spoon to the electrode.

Having the aforementioned considerations in mind, we set our electrolysis up with a tungsten rod anode and a mercury cathode, employing an amalgamated copper spoon with a drop of mercury (see Figure 2-3). For other materials and reaction conditions, the anode can also consist of a platinum wire or foil depending on the respective cathode material. The amalgamated copper spoon spatially hinders the scalability of the intercalation reaction.

### *Solvent (Electrolyte)*

Electrolysis is only feasible with the right electrolyte consisting of a solvent and a dissolved salt. A prerequisite is that the solvent conducts the electric current since electrolysis only takes place at the interface between the electrode and the medium. Therefore, the solvent plays a key role for the outcome of the electrolysis.[32, 64] Big factors are potential range, dissolvability of salts, proton activity, dielectric constant, toxicity, price, vapour pressure, usable temperature range, ion pair formation and many more. When determining the right solvent, one can choose from the following groups: protic solvents, aprotic solvents, salts, and supercritical fluids.[49] Protic solvents are defined as those which can dissociate protons or build intramolecular hydrogen bonds e.g., acids, alcohols, water and some basic solvents. An example for an acidic protic solvent is sulphuric acid. It is widely used in electrolysis reaction because it can dissolve many organic substrates, dissociates and thereby exhibits good electrical conductivity thereby eliminating the need of a support electrolyte to carry the electrical charge. An example for the use of sulfuric acid is the cation intercalation in *MX*enes like $Ti_3C_2T_x$ ($M_{n+1}X_nT_x$ with $M$ = Ti, V, Nb, Mo, Ta, Hf; $X$ = N, C; $T$ = OH, O, F, Cl).[65] On the downside, the work up procedure is more difficult due to the high boiling point, as well as a possible sulfonation and protonation of substrates.[66] Other possible acidic solvents are acetic acid and hydrogen fluoride.[67-68] Considering neutral solvents water is the main utilized solvent, due to its high dielectric constant, high ability to dissolve supporting electrolytes and lack of toxicity.[69] Water is the preferred solvent, but sometimes its properties are undesirable or inadequate. Choosing aprotic solvents avoids adsorption phenomena and complicated reaction mechanisms while at the same time simplifying the process. The lack of protons guarantees longer life times of intermediates, as well as fewer side reactions. Furthermore, a wider range of potentials is applicable for the reactions in contrast to aqueous solvents. The most commonly used aprotic solvents in electrochemical reactions are acetonitrile (MeCN), dimethyl formamide (DMF), and dimethyl sulfoxide (DMSO).[70-71] FeSe-based electrochemical intercalation reactions employed quite a variety of solvents such as N,N-dimethyl formamide (DMF),[28] N-methyl-2-pyrrolidone (NMP),[23] propylene carbonate (PC),[25] polyethylene glycol (PEG),[72] mixtures of dimethyl carbonate (DMC), and ethylene carbonate (EC)[25, 27, 73-74] or ionic liquids like diethylmethyl(2-methoxyethyl)ammonium bis(trifluoromethylsulfonyl)imide (DEME-TFSI)[75] or 1–ethyl–3–methylimidazolium tetrafluoroborate (EMIM-$BF_4$).[76]

We chose DMF as solvent because it has a high polarity ($\mu$ = 3.8 D), a low melting and a high boiling temperature. Therefore, it provides a wide operating range. The only slight disadvantage of DMF is that it is susceptible to hydrolysis which yields dimethylamine and formic acid. Working under Schlenk conditions and purifying the staring material avoids this process.[28]

*Supporting electrolyte*

One prerequisite for the supporting electrolyte is that it must be inert to electrode reactions in the range of the working potential. Within a non-metallic liquid, the flow of the electric current depends on the ions. Important factors are the dissociation constant, solubility, mobility of the ions and discharge potential.[64] Supporting electrolytes consist of two groups: anionic and cationic. [77] Oxidizable anions are chosen for indirect electrolytic oxidation. If the anionic supporting electrolytes should not be easily oxidizable, anions such as perchlorate[78], tetrafluoroborate[79], hexafluorophosphate[80] or nitrates[81] should be chosen due to their high discharge potential. Thus in anionic oxidation they will not be oxidized before the substrate. When considering cathodic reactions the limiting factor for cationic and anionic electrolytes is the discharge potential. Discharge should not occur before the desired reaction. Alkaline and alkaline-earth cations are favourable in inorganic salts.[27, 82] In organic electrochemistry, tetraalkylammonium salts ($R_4N^+X^-$, $R$ = alkyl; $X$ = anion) are prevalently used. Tetraethyl (TEA)- and tetrabutylammonium (TBA) salts are most common whereas the anion can consist of tetrafluoroborates, perchlorates or halides.[83] Tetraalkylammonium ions are hydrophobic and build hydration shells in aqueous solvents which can prevent the direct contact of cation with the electrode surface.[84-85] The ions are also soluble in non-aqueous solvents such as tetrahydrofuran (THF), DMF or MeCN.[86] Furthermore, quaternary ammonium cations are inert towards reduction at electrodes and have a wide electrochemical window, which is due to the saturated alkyl substituents on the nitrogen atom.[87-88] Contrary to lithium salts, these salts are safe to handle and not combustible in organic solvents even when operating at high temperatures. Additionally, Cooper *et al.*, Sirisaksoontron *et al.*

and Shi *et al.* proved that these cations are effective for chemical expansion and intercalation.[23, 28, 83, 89]

Considering all of the above mentioned points, we selected tetraalkylammonium salts as our supporting electrolyte. A salt deposit was placed under the anode if the solubility of the salt was lower than 1 mol $L^{-1}$. During electrolysis, the deposit resupplied educt when it was consumed. Halides were chosen due to their availability and high solubility in DMF. Iodides were preferably selected because the formation of $I_3^-$ is easily observable at the anode. Furthermore, complex fluoride ($BF_4^-$, $PF_6^-$), chloride or bromide anions are reactive towards the glass container and the anode materials (tungsten, platinum).

*Reaction conditions*

The aforementioned considerations are the starting point for synthesis optimization. However, quite a few additional parameters have to be kept in mind and modified depending on the desired result. After choosing a galvanostatic approach and the required electrodes, a certain voltage has to be choosen (three to fifteen Volt). Most experiments in this thesis were conducted at three Volt. In the next step, the desired duration and temperature have to be selected to avoid side reactions and the decomposition of the solvent together with the supporting electrolyte. The duration of the electrolysis is dependent on the utilized electrolyte salt and the mobility of the ions. For the electrolysis with a FeSe educt, the electrolysis took three to four days for a complete intercalation. Further parameters which directly influence the electrolyses are educts, electrolyte concentration and mass transport through the solution.

Since we found the right synthesis conditions for the intercalation reaction and the resulting compound to be phase pure (see Chapter 2.2), the main objective was to scale up the reaction to achieve a greater yield and thus being able to further analyse the properties. Thus, a modified electrolysis chamber was constructed to scale up the synthesis. Therefore, the mercury was directly applied on top of the frit in the cathode chamber, eliminating the need of the copper spoon. On the side of the chamber, a new port is added where a platinum wire is melted into a glass rod. The platinum electrode needs to be fully emerged in the mercury “lake” because electrical contacts between the electrode and the solvent would lead to side reactions and the decomposition of the solvent (see Figure 2-4).

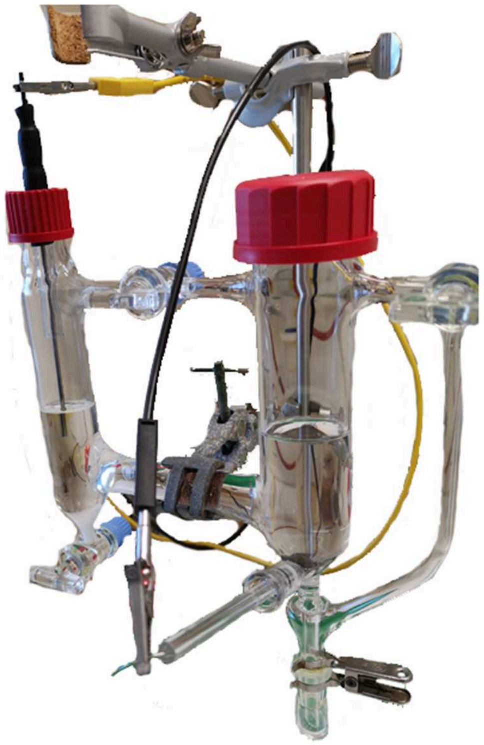

**Figure 2-4.** Electrolysis chamber with changed cathode and mercury lake.

This modification of the chamber leads to an increase in yield of intercalated product, because the surface of mercury drop, which serves as the electrical contact for the educt, is two to three times larger compared to the amalgamated copper spoon.

## 2.2 Electrochemical synthesis and crystal structure of the organic ion intercalated superconductor $(TMA)_{0.5}Fe_2Se_2$ with $T_c$ = 43 K

Bettina Rendenbach, Timotheus Hohl, Sascha Harm, Constantin Hoch and Dirk Johrendt

Published in: *Journal of the American Chemical Society*, **2021**, *143*, 3043–3048.

Reprinted and adapted with permission from American Chemical Society.

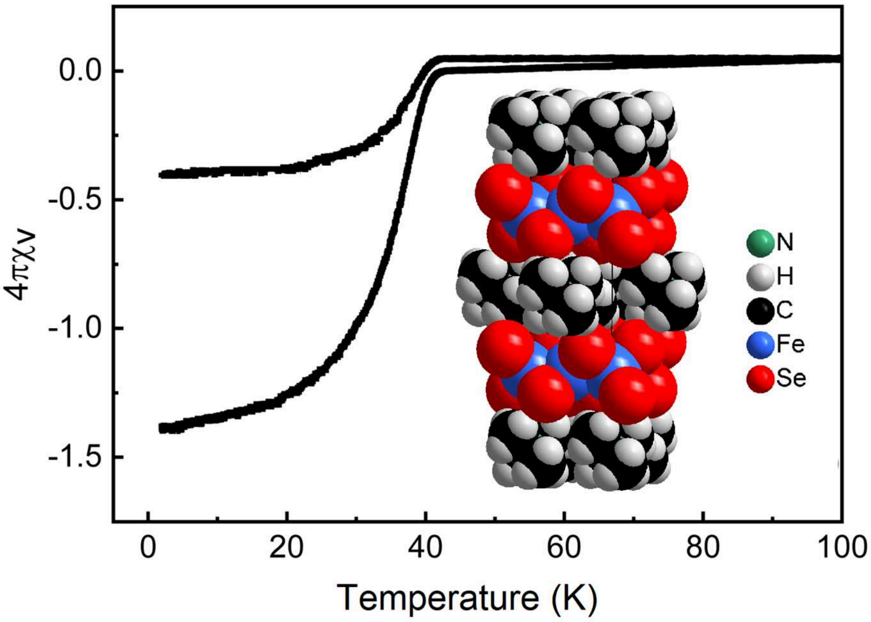

### Abstract

Intercalation of organic cations in superconducting iron selenide can significantly increase the critical temperature ($T_c$). We present an electrochemical method using $\beta$-FeSe crystals ($T_c \approx 8$ K) floating on a mercury cathode to intercalate tetramethylammonium ions ($TMA^+$) quantitatively to obtain bulk samples of $(TMA)_{0.5}Fe_2Se_2$ with $T_c = 43$ K. The layered crystal structure is closely related to the $ThCr_2Si_2$-type with disordered $TMA^+$ ions between the FeSe layers. Although the organic ions are not detectable by X-Ray diffraction, packing requirements as well as first principle DFT calculations constrain the specified structure. Our synthetic route enables electrochemical intercalations of other organic cations with high yields to greatly optimize the superconducting properties, and to expand this class of high-$T_c$ materials.

## Introduction

In a superconductor electrons form pairs and electric currents flow dissipation-less below a critical temperature ($T_c$). Iron-based superconductors discovered in 2008[90-91] represent the second class of high-temperature superconductors beyond the copper oxides, and attract tremendous interest equally in the physics and chemistry communities.[92] While superconducting wires based on copper oxides begin to capture the market in energy technologies,[93-94] iron-based superconductors are still in an early stage of innovation.[95-97] Their main drawback is the critical temperature below the boiling point of liquid nitrogen (77 K),[98] but in spite of immense efforts no bulk iron-based superconductor has reached the 77 K landmark so far. However, the finding of superconductivity up to 99 K[99] in thin $\beta$-FeSe films proved the potential for higher critical temperatures, once the right composition and structure is found. The common structural trait of all iron-based superconductors are layers of edge-sharing $FeX_{4/4}$ tetrahedra ($Fe^{2+}$, $X$ = As, Se), separated by interstitial atoms of various kinds. An impressive family of superconducting compounds[100] emerged by stacking of Fe$X$ layers with layers of alkaline[101], alkaline-earth[102], or rare-earth ions[103], mixtures thereof[104], or with thicker perovskite-like oxide layers[105]. A special case is the $\beta$-polymorph of iron selenide FeSe, which is a superconductor below 8 K without doping.[106] High pressure raises $T_c$ of bulk $\beta$-FeSe to 36.7 K at 8.9 GPa,[107] while one unit cell thin FeSe layers exhibit superconductivity up to 99 K when doped with electrons.[108-109] Likewise the critical temperature of bulk $\beta$-FeSe increases by electron transfer from cationic species in the van-der-Waals gap. Solid-state reactions of $\beta$-FeSe with potassium yielded superconducting samples with $T_c$ around 30 K,[110] which are phase separated.[111] However, intercalation reactions with $\beta$-FeSe as host compound can proceed at low temperatures via soft chemistry methods.[41, 112-115] Examples are the intercalation of lithium ions with amine and amide species in liquid ammonia ($Li_x(NH_2)_y(NH_3)_{1-y}Fe_2Se_2$, $T_c = 43$ K)[116], lithium hydroxide layers by hydrothermal methods ($[(Li_{1-x}Fe_x)OH]FeSe$, $T_c = 42$ K)[117], or alkaline ions with amine molecules by solvothermal reactions ($Na_{0.39}(C_2N_2H_8)_{0.77}Fe_2Se_2$, $T_c = 46$ K)[41]. Another promising approach is the electrochemical intercalation of alkali metal ions. Several studies reported electrochemically intercalated FeSe compounds with critical temperatures around 40±5 K.[25-27, 74, 76] Almost all of these materials suffer from either inhomogeneity, small superconducting volume fractions, or incomplete conversion of the host $\beta$-FeSe. Only recently, Shi *et al.* reported the intercalation of large cetyl-trimethylammonium ions ($CTA^+$)[23, 118] and tetrabutylammonium ions ($TBA^+$)[28] in individual $\beta$-FeSe crystals with superconducting transitions up to 50 K. A drawback of this method is the tiny sample amount, consisting of one tiny crystal on the tip of an indium wire. Furthermore, the knowledge about the structures of the $CTA^+$ and $TBA^+$ intercalates is still incomplete and limited to the distance between the FeSe layers so far,[23, 28] while the detailed structure, even of the FeSe layers therein, remains unknown.

Here, we demonstrate the electrochemical intercalation of tetramethylammonium cations ($TMA^+$) into $\beta$-FeSe. A modified setup of the electrochemical cell yields single phase bulk samples of $(TMA)_{0.5}Fe_2Se_2$ with a superconducting transition at 43 K. We deduce a crystal structure closely related to the 122-type iron arsenide superconductors with $ThCr_2Si_2$-type structure.

## Experimental

Single crystals of the host $\beta$-FeSe were prepared by chemical vapour transport as described in the literature.[119-121] 562.4 mg selenium powder (Chempur, 99.9 %) and 437.8 mg iron powder (CHEMPUR, 99.9 %) in a molar ratio 1 : 1.1 were ground together with $AlCl_3$/KCl (ALFA AESAR, 99.985 % / GRÜSSING, 99.5 %, dried) (7.75 g : 2.25 g). The mixture was sealed under vacuum in a glass ampoule (diameter 5 cm, length 4 cm) and placed in a vertical two-zone furnace and heated to 390 °C at the bottom and 290 °C at the top. This temperature gradient was held for 5–10 days. After cooling the ampoules were opened and the crystals collected from the inner top of the ampoules. The flux was washed away with water and ethanol. An optimized setup allows to grow about 1 gram $\beta$-FeSe crystals per batch within one week. The quality of the host material was checked by powder X-Ray diffraction of the crushed crystals and by magnetic susceptibility measurements. A portion of $\beta$-FeSe crystals was distributed on a drop of mercury in an amalgamated copper spoon serving as the cathode.[17] The apparatus was held under inert conditions using purified argon. The crystals float on the surface of the mercury ensuring the electrical contact between the cathode and the electrolyte consisting of tetramethylammonium iodide (TMAI, SIGMA-ALDRICH, 99 %, 0.1 molar) dissolved in 100 mL dried and destilled DMF. A voltage of three Volt was applied for three to four days. For details, we refer to supporting information in Chapter 2.1ffe and Chapter A.1. During the electrolysis, the $I^-$ in the electrolyte is oxidized to $I_3^-$, while $\beta$-FeSe is reduced electrochemically with the charge compensated by the intercalation of $TMA^+$ ions. After the reaction is completed, the black air-sensitive crystals were easy to separate from the mercury drop, washed with dry DMF and dried under vaccuum. The yield scales with the size of the mercury surface and is about 50 to 200 mg per process cycle.

## Results and discussion

Figure 2-5 shows the powder X-Ray pattern with the Rietveld fit. No impurity phases or residual *β*-FeSe are discernible within the limits of the method (≈ 1 wt. %). Some intensities slightly deviate, which is caused by the preferred orientation of the plate-like crystallites. The crystal structure was solved from the powder X-Ray diffraction data in the space group *I*4/*mmm* with lattice parameters $a$ = 3.8585(2) Å, $c$ = 20.377(3) Å.

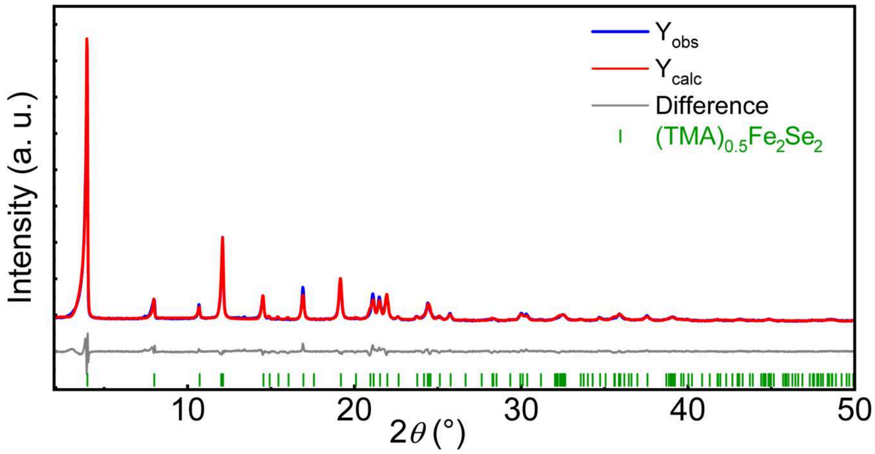

**Figure 2-5.** X-Ray diffraction pattern of $(TMA)_{0.5}Fe_2Se_2$ (blue) with Rietveld fit (red) and difference curve (grey).

Only the iron and selenium atoms contribute significantly to the diffraction pattern, because CHN atoms are weak scatterer and the orientations of the $TMA^+$ ions are very likely disordered. However, the nitrogen atom in the centre of the $TMA^+$ ion is not affected by the disorder and was included in the refinement, though its contribution is expectedly weak. Relevant crystallographic data are compiled in Table 2-1 and Table 2-2.

**Table 2-1.** Crystallographic data of $(TMA)_{0.5}Fe_2Se_2$.

| | |
|---|---|
| Space group | *I*4/*mmm* (no. 139) |
| Lattice parameters (Å) | $a$ = 3.8585(2)<br>$c$ = 20.377(3) |
| Volume (Å$^3$) | $V$ = 303.4(1) |
| $Z$ | 2 |
| Density (g·cm$^{-3}$) | 3.03(1) |
| $R_{exp}/R_{Bragg}$ | 0.815/1.269 |
| $R_p/R_{wp}$ | 1.940/2.789 |
| GooF | 3.423 |

**Table 2-2.** Atomic coordinates and displacement parameters.

| Atom | Wyckoff | $x$ | $y$ | $z$ | SOF | $B_{iso}$ |
|---|---|---|---|---|---|---|

| | | | | | | |
|---|---|---|---|---|---|---|
| Fe | 4*d* | 0 | ½ | ¼ | 1 | 2.0(1) |
| Se | 4*e* | 0 | 0 | 0.3160(4) | 1 | 1.2(1) |
| N | 2*a* | 0 | 0 | 0 | 0.5 | 3.9(1) |
| Bond distances (Å) and angles (°) | | | | | | |
| Fe – 4 Se 2.352(3) | | | | φ Se-Fe-Se | 110.2(3) | |

This atom configuration in the space group *I*4/*mmm* corresponds to the $ThCr_2Si_2$-type structure, known as the “122-type” structure of the iron arsenide superconductors.[102] Even though the cavities in the structure around the N-atom sites at (0,0,0) and (½,½,½) appear large (Figure 2-6a), they are not large enough to be fully occupied by $TMA^+$ ions.

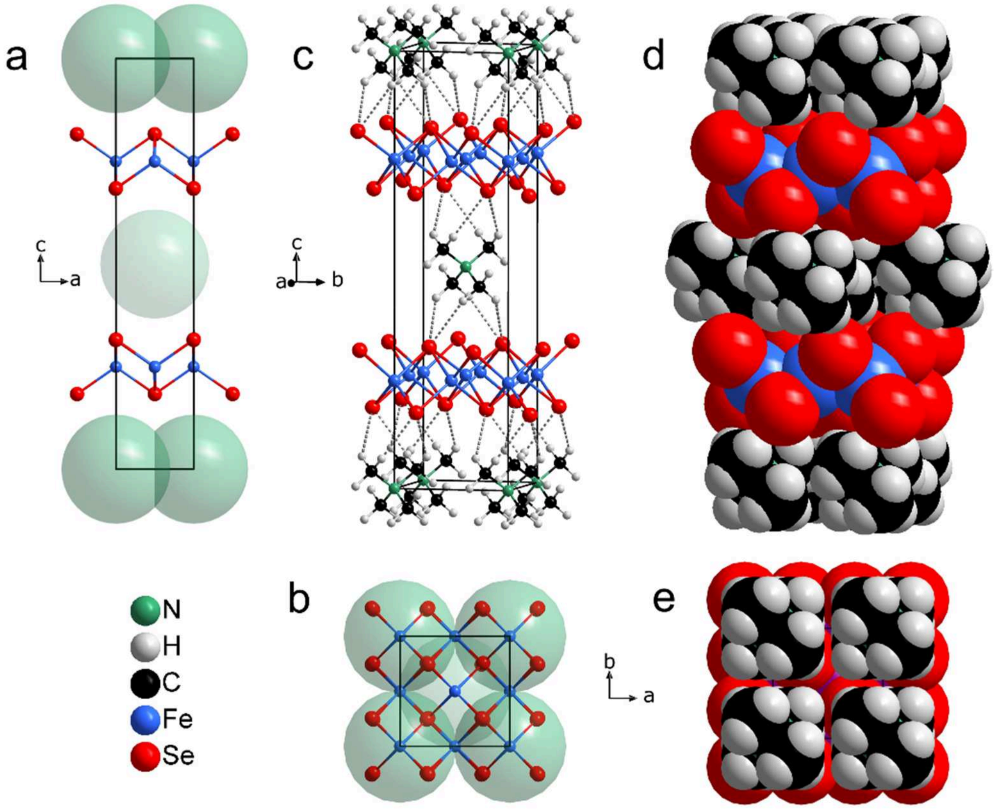

**Figure 2-6**. Crystal structure of $(TMA)_{0.5}Fe_2Se_2$ **a**: Structure determined from powder X-Ray diffraction in space group *I*4/*mmm*. Large green spheres indicate the space required by a $TMA^+$ ion. **b**: Doubled unit cell with $a'=\sqrt{2}a$ , $b'=\sqrt{2}\,b$ with perfectly fitting TMA spheres. **c:** Complete structure of $(TMA)_{0.5}Fe_2Se_2$ in space group $I\bar{4}2m$ with hydrogen bridges shown as dashed bonds. **d**: Space filling model **e**: View perpendicular to the $TMA^+$ layers.

The encasing sphere of a tetrahedrally shaped $TMA^+$ ion has a diameter of 5.5–5.6 Å[122-123] and is therefore incompatible with the lattice parameter $a$ = 3.8585(2) Å. Indeed the diagonal of the unit cell $\sqrt{2}a$ = 5.457 Å has the suitable size to accommodate neighbouring $TMA^+$ ions (Figure 2-6b), thus we assume that the positions (0,0,0) and (½,½,½) are statistically half occupied, resulting in the formula $(TMA)_{0.5}Fe_2Se_2$. An ordered model of the structure in space group $I\bar{4}2m$ is shown in Figure 2-6c as ball-and-stick representation, and in Figure 2-6d with the van-der-Waals radii of the atoms. Figure 2-6e shows how the $TMA^+$ ions almost perfectly fit in the $\sqrt{2}a \times \sqrt{2}a$ supercell. The space filling of this structure as calculated by PLATON[124] is as high as 77 %, similar to a typical compound with $ThCr_2Si_2$-type structure like $BaFe_2As_2$ which has a space filling of 82 %. Each two of the three hydrogen atoms at the $-CH_3$ groups form C-H···Se hydrogen bridges with a H···Se distance of 2.72 Å (Figure 2-6c), similar to the N-D···Se distance of 2.76 Å measured by Burrard-Lucas *et al.* in $Li_x(ND_2)_y(ND_3)_{1-y}Fe_2Se_2$ using neutron diffraction.[116] We do not expect more accurate structural data from neutron diffraction because of the orientational disorder of the $TMA^+$ molecules. In comparable compounds like $Na_{0.39}(C_2N_2H_8)_{0.77}Fe_2Se_2$, the molecules could not be localized by neutron diffraction either.[41]

We have checked the validity of this model by first principle DFT calculations using the VASP code.[125-127] DFT reproduces experimental structures within a certain accuracy that depends on the functional used. We have chosen the SCAN[128] functional, which reproduces the experimental lattice parameters of our compound within 0.1 %. The Fe-Se bond length and Se-Fe-Se bond angle deviate by only +2.2 % and +0.4 % from the experimental values, respectively. Tables 2-3 and Table 2-4 show the calculated structure data in the space group $I\bar{4}2m$ with experimental values in square brackets. Table A-1 compares the experimental parameters with calculated ones using different exchange-correlation functionals. The excellent agreement with the experimental values clearly supports our structure model.

**Table 2-3.** Calculated structure parameters of $(TMA)_{0.5}Fe_2Se_2$ with experimetal values in square brackets.

| | |
|---|---|
| Crystal system | Tetragonal |
| Space group | $I\bar{4}2m$ (no. 121) |
| Lattice parameters (Å) | $a$ = 5.454 [5.457]<br>$c$ = 20.383 [20.377] |
| Volume (Å$^3$) | 606.3 [606.7] |

**Table 2-4.** Atom positions of $(TMA)_{0.5}Fe_2Se_2$ with experimetal values in square brackets.

| Atom | Wyckoff | *x* | *y* | *z* |
|---|---|---|---|---|
| Se | 8*i* | 0.7570 [¾] | *x* | 0.6797 [0.6840] |
| Fe1 | 4*e* | 0 | 0 | ¾ [ ¾ ] |

| | | | | |
|---|---|---|---|---|
| Fe2 | $4d$ | 0 | ½ | ¼ [ ¼ ] |
| N | $2a$ | 0 [0] | 0 [0] | 0 [0] |
| C | $8i$ | 0.1595 | $x$ | 0.9583 |
| H1 | $8i$ | 0.2706 | $x$ | 0.9912 |
| H2 | $16j$ | 0.0435 | 0.7270 | 0.0729 |

To get an idea of the thermodynamic stability, we have calculated the phonon dispersions and phonon density-of-states. A crystal is stable if its potential energy increases against any combinations of atomic displacements, which means that all phonons have real (positive) frequencies.[129] Calculations using the space group $I\bar{4}2m$ reveal only minor imaginary modes (Figure 2-7a).

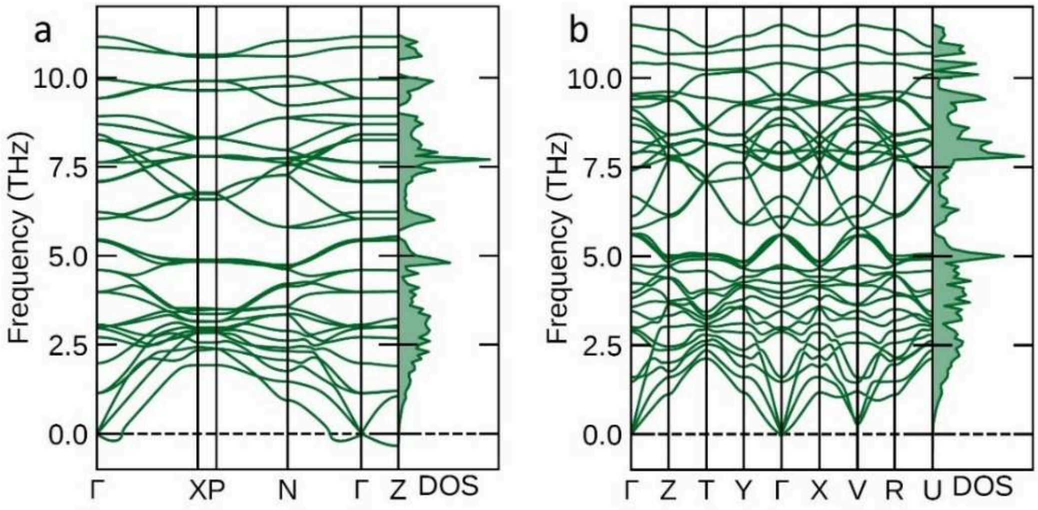

**Figure 2-7.** Phonon dispersion and DOS of $(TMA)_{0.5}Fe_2Se_2$. **a**: Structure in space group $I\bar{4}2m$. **b**: Triclinic structure in $P1$ after optimization without symmetry constraints.

This reflects the fact that our structure model is not perfect and neglects the disorder of the organic cations, which is not treatable by DFT methods. The $TMA^+$ ions are possibly ordered over half the sites in the layers due to space requirements, but order is lost along the $c$ axis. Interestingly, no imaginary modes occur after structure optimizations without symmetry constraints (Figure 2-7b). Even though this triclinic structure is chemically reasonable, its unit cell is incompatible with the X-Ray diffraction pattern.

Chemical C-H-N analysis, EDS, and FT-IR spectroscopy confirm the composition $(TMA)_{0.5}Fe_2Se_2$ within the errors of these methods, respectively. The molar ratio of C:H:N was determined to 4.1:13.1:1 (see Chapter A.1, Table A-2) which is consistent with $C_4H_{12}N^+$ and confirms the integrity of the $TMA^+$

ion. The CHN mass fraction with respect to FeSe was 12.02 %. This corresponds to a value of 0.24 $TMA^+$ molecules per FeSe and confirms the composition $(TMA)_{0.5}Fe_{2.}Se_2$. The EDS analysis shows a ratio of Fe:Se of 1.1(1):1(1) (see Chapter A.1, Table A-3).

Figure 2-8 shows the infrared spectra of tetramethylammonium iodide (TMAI) and $(TMA)_{0.5}Fe_2Se_2$ together with the spectrum calculated by DFPT. $\beta$-FeSe is not infrared active. The $TMA^+$ ion has $T_d$ symmetry, and 7 of the 19 fundamental vibrations are infrared active.[130] Raman measurements were not possible due to the strong absorption of the product (black colour). The $TMA^+$ ions in $(TMA)_{0.5}Fe_2Se_2$ are located between $\beta$-FeSe layers. Therefore, in comparison to TMAI, the infrared active species in our samples are strongly diluted by the strong IR absorber $\beta$-FeSe. This may be the main factor for the weak intensity of the bands in the spectra. The FT-IR spectra of TMAI and $(TMA)_{0.5}Fe_2Se_2$ are nevertheless compatible with intercalation of $TMA^+$ into $\beta$-FeSe.

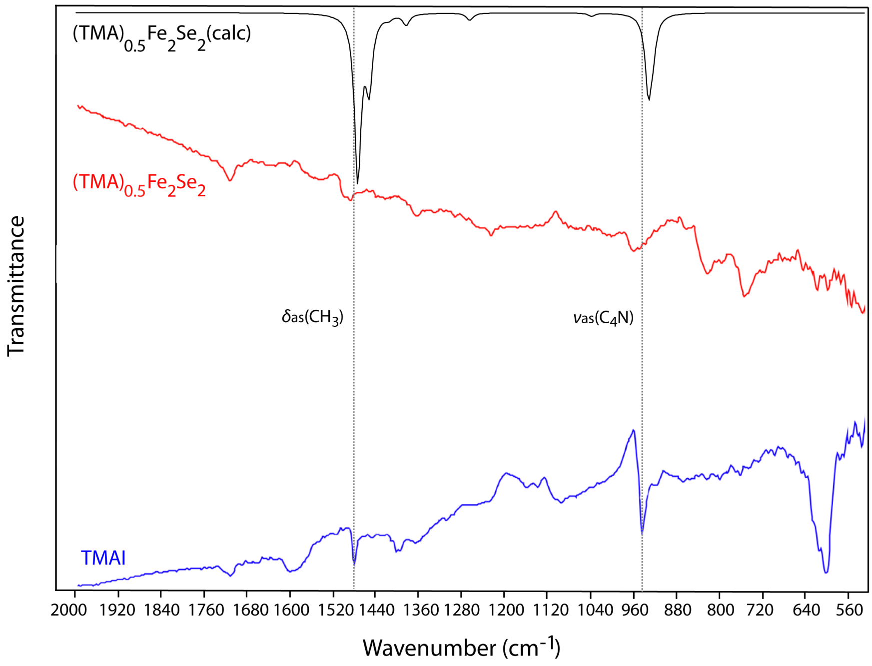

**Figure 2-8.** FT-IR spectra of TMAI and $(TMA)_{0.5}Fe_2Se_2$ and the spectrum calculated from DFPT.

This indicates the asymmetric deformation mode vibrations of the methyl group $\delta_{as}(CH_3)$ at 1481 $cm^{-1}$ and 1501 $cm^{-1}$ in both spectra (TMAI and $(TMA)_{0.5}Fe_2Se_2$), respectively. The bands are in accordance with literature and only a slight shift to higher wavenumber is apparent (1483 $cm^{-1}$).[131] Furthermore, around 958 $cm^{-1}$ a band is visible in both spectra, which could be assigned to the asymmetric stretching mode of the skeletal $C_4N$. The strong band at ~600 $cm^{-1}$ in the TMAI spectra might be assigned to methyl iodide which could originate from a side reaction during the measurement process. This band is not visible in the product spectrum. Note that the DFPT calculated spectrum matches the measured one well except for a slight zero point shift.

Furthermore, the intercalation is topotactic and reversible. High-temperature powder X-Ray diffraction reveals the complete recovery of tetragonal $\beta$-FeSe after heating to 200 °C, and the transformation to the hexagonal polymorph at 550 °C (Figure 2-9).

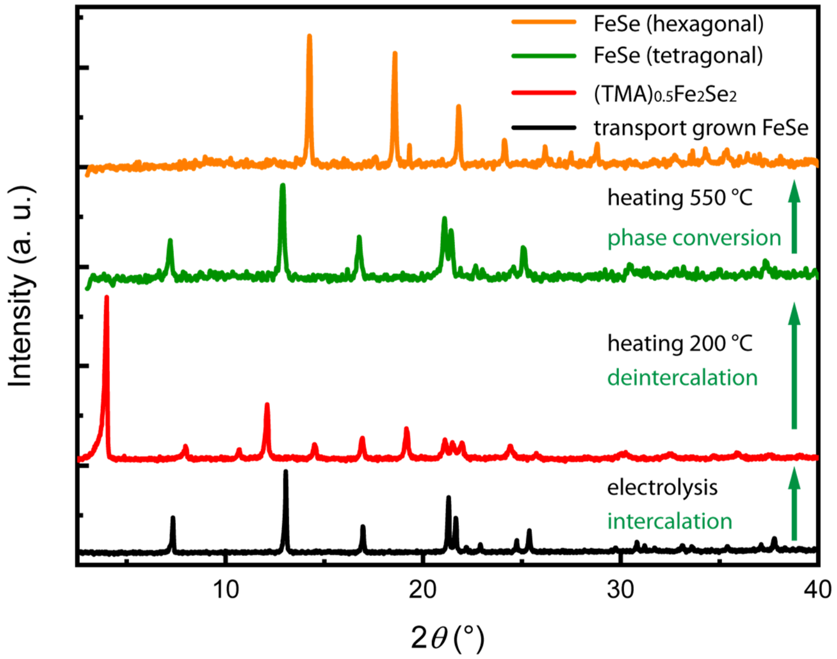

**Figure 2-9.** Powder X-Ray diffraction patterns (Mo-K$_{\alpha1}$ radiation) of the host $\beta$-FeSe (black), (TMA)$_{0.5}$Fe$_2$Se$_2$ after electrochemical intercalation (red), recovered $\beta$-FeSe after deintercalation (green) and after conversion to hexagonal FeSe (orange).

The regained $\beta$-FeSe has the same lattice parameters ($a$ = 3.771(3) Å, $c$ = 5.524(7) Å) as the starting material. The susceptibilities curves show that the regained $\beta$-FeSe is superconducting at 8 K, which is consistent with the original properties of $\beta$-FeSe (see Chapter A.1, Figure A-2 and Figure A-3).

The magnetic susceptibility of (TMA)$_{0.5}$Fe$_2$Se$_2$ shows a bulk superconducting transition at 43 K (Figure 2-10). Field-cooled and zero-field cooled curves slightly split above $T_c$ due to traces of ferromagnetic impurities not detectable by X-Ray diffraction.

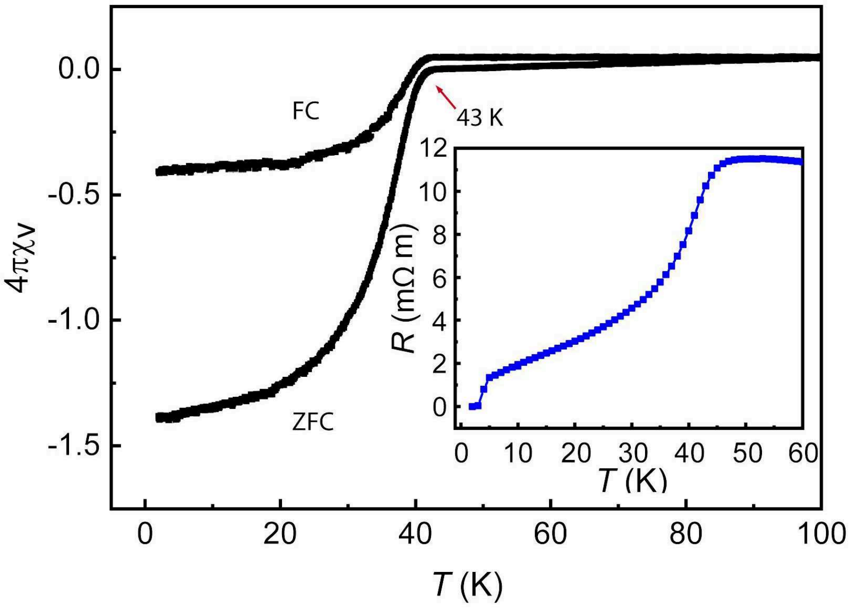

**Figure 2-10.** Magnetic susceptibility of $(TMA)_{0.5}Fe_2Se_2$ at 15 Oe. Insert: DC resistivity of a cold pressed pellet.

The large shielding fraction above 100 % at low temperatures comes from the uncorrected demagnetization of the plate-like crystallites oriented perpendicular to the magnetic field. No further drop of the susceptibility near 8 K is visible, which confirms that the intercalation is complete and no residual host *β*-FeSe remains. Measuring the electrical resistivity turned out difficult due to degradation of the sample during pressing, and furthermore the deintercalation temperature around 200 °C allowed no sintering of the pellet.

The result is shown in the insert of Figure 2-10, where the onset of the superconductivity is near 45 K followed by a broad transition until an additional drop to zero resistivity occurs at 6 K. The latter is caused by ~ 8 wt.-% deintercalated FeSe. Isothermal magnetization measurements (Figure 2-11) show the “butterfly” pattern typical for a hard type-II superconductor. The ripples in the curve only occur at increasing field, which indicates that they are flux jumps.

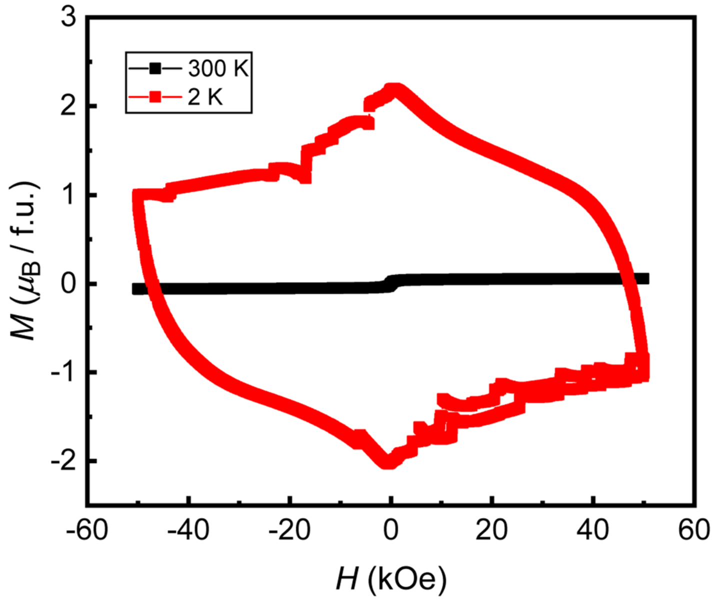

**Figure 2-11.** Magnetization isotherms of (TMA)$_{0.5}$Fe$_2$Se$_2$ at 2 K and at 300 K.

### Conclusion

In conclusion, we demonstrate that the electrochemical intercalation of tetramethylammonium ions (TMA$^+$) into the van-der-Waals gap of $\beta$-FeSe is feasible with high yields. Powder X-Ray diffraction combined with DFT calculations reveal a reliable ordered model of the crystal structure. (TMA)$_{0.5}$Fe$_2$Se$_2$ forms a variant of the ThCr$_2$Si$_2$-type structure, also known as the “122-type” in the family of iron arsenide superconductors. The TMA$^+$ ions are closely packed between the FeSe layers but disordered over two equivalent positions and in different orientations. Magnetization and electrical resistivity measurements show bulk superconducting transitions at 43 K and identify (TMA)$_{0.5}$Fe$_2$Se$_2$ as type-II superconductor. Our results provide the first insights into the crystal structure of a superconducting FeSe-alkylammonium intercalate and pave the way to further exploit the electrochemical route towards related compounds with potentially higher critical temperatures.

## 2.3 References

[1] A. Volta, *Philos. Trans. R. Soc. London* **1800**, *90*, 403–431.

[2] W. Nicholson, *J. Nat. Phil. Chem. Arts* **1800**, *4*, 179–191.

[3] J. J. Berzelius, *Föreläsningar i djurkemien, Vol. 1*, Carl Delén, Stockholm, **1806**, pp. 1–276.

[4] H. Davy, *Philos. Trans. R. Soc. London* **1807**, *97*, 1–56.

[5] S. Ross, M. Faraday, H. B. Hartley, *Notes Rec. R. Soc. London* **1961**, *16*, 187–220.

[6] T. F. O'Brien, T. V. Bommaraju, F. Hine, "History of the Chlor-Alkali Industry" in *Handbook of Chlor-Alkali Technology*, Springer, Boston, MA, USA, **2005**, pp. 17–36.

[7] R. T. Baldwin, *J. Chem. Educ.* **1927**, *4*, 313–319.

[8] I. Moussallem, J. Jörissen, U. Kunz, S. Pinnow, T. Turek, *J. Appl. Electrochem.* **2008**, *38*, 1177–1194.

[9] K. Grjotheim, C. Krohn, M. Malinovsky, K. Matiasovsky, J. Thonstad, *Aluminium electrolysis: fundamentals of the Hall-Héroult process*, 2nd ed., Aluminium Verlag, Düsseldorf, Germany, **1982**.

[10] W. E. Haupin, *J. Chem. Educ.* **1983**, *60*, 279–282.

[11] C. A. C. Sequeira, D. M. F. Santos, *J. Braz. Chem. Soc.* **2009**, *20*, 387–406.

[12] M. Ciobanu, J. P. Wilburn, M. L. Krim, D. E. Cliffel, "Fundamentals" in *Handbook of Electrochemistry*, 1th ed. (Ed.: C. G. Zoski), Elsevier, Amsterdam, Netherlands, **2007**, pp. 3–29.

[13] D. Pollok, S. R. Waldvogel, *Chem. Sci.* **2020**, *11*, 12386–12400.

[14] E. J. Biddinger, M. A. Modestino, *Electrochem. Soc. Interface* **2020**, *29*, 43–47.

[15] J.-Y. Huang, K.-Q. Zhang, Y.-K. Lai, *Int. J. Photoenergy* **2013**, *2013*, 761971.

[16] M. Nakayama, T. Kanaya, J.-W. Lee, B. N. Popov, *J. Power Sources* **2008**, *179*, 361–366.

[17] F. Tambornino, J. Sappl, F. Pultar, T. M. Cong, S. Hübner, T. Giftthaler, C. Hoch, *Inorg. Chem.* **2016**, *55*, 11551–11559.

[18] E. Hitz, J. Wan, A. Patel, Y. Xu, L. Meshi, J. Dai, Y. Chen, A. Lu, A. V. Davydov, L. Hu, *ACS Appl. Mater. Interfaces* **2016**, *8*, 11390–11395.

[19] C. Song, G. Noh, T. S. Kim, M. Kang, H. Song, A. Ham, M. Jo, S. Cho, H.-J. Chai, S. R. Cho, K. Cho, J. Park, S. Song, I. Song, S. Bang, J. Y. Kwak, K. Kang, *ACS Nano* **2020**, *14*, 16266–16300.

[20] N. Wang, H. Tang, M. Shi, H. Zhang, W. Zhuo, D. Liu, F. Meng, L. Ma, J. Ying, L. Zou, Z. Sun, X. Chen, *J. Am. Chem. Soc.* **2019**, *141*, 17166–17173.

[21] G.-R. Li, H. Xu, X.-F. Lu, J.-X. Feng, Y.-X. Tong, C.-Y. Su, *Nanoscale* **2013**, *5*, 4056–4069.

[22] N. Z. Wang, M. Z. Shi, C. Shang, F. B. Meng, L. K. Ma, X. G. Luo, X. H. Chen, *New J. Phys.* **2018**, *20*, 023014.

[23] M. Z. Shi, N. Z. Wang, B. Lei, C. Shang, F. B. Meng, L. K. Ma, F. X. Zhang, D. Z. Kuang, X. H. Chen, *Phys. Rev. Mater.* **2018**, *2*, 074801.

[24] B. Chen, D. Chao, E. Liu, M. Jaroniec, N. Zhao, S.-Z. Qiao, *Energ. Environ. Sci.* **2020**, *13*, 1096–1131.

[25] T. Kajita, T. Kawamata, T. Noji, T. Hatakeda, M. Kato, Y. Koike, T. Itoh, *Physica C Supercond.* **2015**, *519*, 104–107.

[26] H. Abe, T. Noji, M. Kato, Y. Koike, *Physica C Supercond.* **2010**, *470*, S487–S488.

[27] A. M. Alekseeva, O. A. Drozhzhin, K. A. Dosaev, E. V. Antipov, K. V. Zakharov, O. S. Volkova, D. A. Chareev, A. N. Vasiliev, C. Koz, U. Schwarz, H. Rosner, Y. Grin, *Sci. Rep.* **2016**, *6*, 25624.

[28] M. Z. Shi, N. Z. Wang, B. Lei, J. J. Ying, C. S. Zhu, Z. L. Sun, J. H. Cui, F. B. Meng, C. Shang, L. K. Ma, X. H. Chen, *New J. Phys.* **2018**, *20*, 123007.

[29] N.-Z. Wang, M.-Z. Shi, B. Lei, X.-H. Chen, *Acta Phys. Sin.* **2018**, *67*, 207408.

[30] A. J. Bard, M. Stratmann, H. J. Schäfer, *Encyclopedia of electrochemistry: Organic electrochemistry, Vol. 8*, Wiley-VCH, Weinheim, Germany, **2004**.

[31] T. J. Smith, K. J. Stevenson, "Reference Electrodes" in *Handbook of Electrochemistry*, 1th ed. (Ed.: C. G. Zoski), Elsevier, Amsterdam, Netherlands, **2007**, pp. 73–110.

[32] G. Hilt, *ChemElectroChem* **2020**, *7*, 395–405.

[33] M. M. Baizer, *Naturwissenschaften* **1969**, *56*, 405–409.

[34] R. Parsons, *Chem. Rev.* **1990**, *90*, 813–826.

[35] T. Fuchigami, M. Atobe, S. Inagi, *Fundamentals and applications of organic electrochemistry: synthesis, materials, devices*, 1st ed., John Wiley & Sons, Chichester, West Sussex, United Kingdom, **2014**, pp. 1–238.

[36] S. Chen, "Practical Electrochemical Cells" in *Handbook of Electrochemistry*, 1th ed. (Ed.: C. G. Zoski), Elsevier, Amsterdam, Netherlands, **2007**, pp. 33–56.

[37] D. Pletcher, R. A. Green, R. C. D. Brown, *Chem. Rev.* **2018**, *118*, 4573–4591.

[38] S. R. Waldvogel, S. Lips, M. Selt, B. Riehl, C. J. Kampf, *Chem. Rev.* **2018**, *118*, 6706–6765.

[39] U. Pachmayr, D. Johrendt, *Chem. Commun.* **2015**, *51*, 4689–4692.

[40] M. Burrard-Lucas, D. G. Free, S. J. Sedlmaier, J. D. Wright, S. J. Cassidy, Y. Hara, A. J. Corkett, T. Lancaster, P. J. Baker, S. J. Blundell, S. J. Clarke, *Nat. Mater.* **2012**, *12*, 15–19.

[41] S. Jin, X. Fan, X. Wu, R. Sun, H. Wu, Q. Huang, C. Shi, X. Xi, Z. Li, X. Chen, *Chem. Commun.* **2017**, *53*, 9729–9732.

[42] W. Jud, C. O. Kappe, D. Cantillo, *ChemElectroChem* **2020**, *7*, 2777–2783.

[43] A. M. Couper, D. Pletcher, F. C. Walsh, *Chem. Rev.* **1990**, *90*, 837–865.

[44] A. Economou, P. R. Fielden, *Analyst* **2003**, *128*, 205–213.

[45] T. Fuchigami, "Methods for Organic Electrosynthesis" in *Fundamentals and Applications of Organic Electrochemistry*, 1st ed. (Eds.: T. Fuchigami, S. Inagi, M. Atobe), John Wiley & Sons, Ltd, Chichester, West Sussex, United Kingdom, **2015**, pp. 33–44.

[46] S. B. Beil, T. Müller, S. B. Sillart, P. Franzmann, A. Bomm, M. Holtkamp, U. Karst, W. Schade, S. R. Waldvogel, *Angew. Chem. Int. Ed.* **2018**, *57*, 2450–2454.

[47] D. M. Heard, A. J. J. Lennox, *Angew. Chem. Int. Ed.* **2020**, *59*, 18866–18884.

[48] D. Pletcher, *Electrochem. Commun.* **2018**, *88*, 1–4.

[49] O. Hammerich, H. Lund, "Practical Problems in Electrochemistry" in *Organic Electrochemistry*, 4th ed., Taylor & Francis, Boca Raton, Florida, USA, **2000**, pp. 223–292.

[50] S. Möhle, M. Zirbes, E. Rodrigo, T. Gieshoff, A. Wiebe, S. R. Waldvogel, *Angew. Chem. Int. Ed.* **2018**, *57*, 6018–6041.

[51] W. Kemula, Z. Kublik, *Anal. Chim. Acta* **1958**, *18*, 104–111.

[52] T. Berzins, P. Delahay, *J. Am. Chem. Soc.* **1955**, *77*, 6448–6453.

[53] R. H. Müller, J. F. Petras, *J. Am. Chem. Soc.* **1938**, *60*, 2990–2993.

[54] J. J. Lingane, I. M. Kolthoff, *J. Am. Chem. Soc.* **1939**, *61*, 825–834.

[55] J. E. Anderson, A. M. Bond, R. D. Jones, *Anal. Chem.* **1981**, *53*, 1016–1020.

[56] S. A. Moros, *Anal. Chem.* **1962**, *34*, 1584–1587.

[57] T. R. Copeland, J. H. Christie, R. K. Skogerboe, R. A. Osteryoung, *Anal. Chem.* **1973**, *45*, 995–996.

[58] J. Gajdar, E. Horakova, J. Barek, J. Fischer, V. Vyskocil, *Electroanal.* **2016**, *28*, 2659–2671.

[59] V. Vyskocil, I. Jiránek, J. Barek, K. Pecková, J. Zima, "Are mercury electrodes still useful sensors? Polarographic and voltammetric determination of polarographically reducible

environmental carcinogens" in *Sensing in Electroanalysis*, 2 ed. (Eds.: K. Vytřas, K. Kalcher), University of Pardubice, Pardubice, Czech Republic, **2007**, pp. 105–119.

[60] T. Navrátil, I. Švancara, K. Mrázová, K. Nováková, I. Šestáková, M. Heyrovský, D. Pelclová, *Sensing in electroanalysis* **2011**, *6*, 23–54.

[61] E. Gustafsson, *Water Air Soil Poll.* **1995**, *80*, 99–102.

[62] P. Zuman, *J. Solid State Electr.* **2011**, *15*, 1753–1759.

[63] Ø. Mikkelsen, K. H. Schrøder, *Electroanal.* **2003**, *15*, 679–687.

[64] S. Creager, "Solvents and Supporting Electrolytes" in *Handbook of Electrochemistry*, 1th ed. (Ed.: C. G. Zoski), Elsevier, Amsterdam, Netherlands, **2007**, pp. 57–72.

[65] A. Al-Temimy, K. Prenger, R. Golnak, M. Lounasvuori, M. Naguib, T. Petit, *ACS Appl. Mater. Interfaces* **2020**, *12*, 15087–15094.

[66] D. Fraenkel, *J. Phys. Chem. B* **2012**, *116*, 11662–11677.

[67] Y.-S. Kim, K. D. Harris, B. Limoges, V. Balland, *Chem. Sci.* **2019**, *10*, 8752–8763.

[68] H. Takenaka, M. Kawaguchi, M. Lerner, N. Bartlett, *J. Chem. Soc., Chem. Commun.* **1987**, 1431–1432.

[69] R. K. Guduru, J. C. Icaza, *Nanomaterials* **2016**, *6*, 41.

[70] B. A. Frontana-Uribe, R. D. Little, J. G. Ibanez, A. Palma, R. Vasquez-Medrano, *Green Chem.* **2010**, *12*, 2099–2119.

[71] C. Wan, X. Gu, F. Dang, T. Itoh, Y. Wang, H. Sasaki, M. Kondo, K. Koga, K. Yabuki, G. J. Snyder, R. Yang, K. Koumoto, *Nat. Mater.* **2015**, *14*, 622–627.

[72] Y. Takahei, K. Tomita, Y. Itoh, K. Ashida, J.-H. Lee, N. Nishimoto, T. Kimura, K. Kudo, M. Nohara, Y. Kubozono, T. Kambe, *Sci. Rep.* **2016**, *6*, 18931.

[73] D. Chen, X. Wang, J. Chen, Z. Ren, M. Xue, G. Chen, *Adv. Mater.* **2015**, *27*, 4224–4228.

[74] S.-J. Shen, T.-P. Ying, G. Wang, S.-F. Jin, H. Zhang, Z.-P. Lin, X.-L. Chen, *Chinese Phys. B* **2015**, *24*, 117406.

[75] S. Kouno, Y. Sato, Y. Katayama, A. Ichinose, D. Asami, F. Nabeshima, Y. Imai, A. Maeda, K. Ueno, *Sci. Rep.* **2018**, *8*, 14731.

[76] Y. Cui, Z. Hu, J.-S. Zhang, W.-L. Ma, M.-W. Ma, Z. Ma, C. Wang, J.-Q. Yan, J.-P. Sun, J.-G. Cheng, S. Jia, Y. Li, J.-S. Wen, H.-C. Lei, P. Yu, W. Ji, W.-Q. Yu, *Chin. Phys. Lett.* **2019**, *36*, 077401.

[77] K. Gong, Q. Fang, S. Gu, S. F. Y. Li, Y. Yan, *Energ. Environ. Sci.* **2015**, *8*, 3515–3530.

[78] R. Yivlialin, G. Bussetti, L. Brambilla, C. Castiglioni, M. Tommasini, L. Duò, M. Passoni, M. Ghidelli, C. S. Casari, A. Li Bassi, *J. Phys. Chem. C* **2017**, *121*, 14246–14253.

[79] S. Zhao, Y. Huang, Y. Wang, D. Zhu, L. Zhang, H. Wang, *ACS Appl. Energy Mater.* **2021**, *4*, 737–744.

[80] K. M. Choi, K. H. Kim, *J. Appl. Polym. Sci.* **1992**, *44*, 751–763.

[81] Z. Yan, H. Sun, X. Chen, H. Liu, Y. Zhao, H. Li, W. Xie, F. Cheng, J. Chen, *Nat. Commun.* **2018**, *9*, 2373.

[82] N. T. Hahn, D. M. Driscoll, Z. Yu, G. E. Sterbinsky, L. Cheng, M. Balasubramanian, K. R. Zavadil, *ACS Appl. Energy Mater.* **2020**, *3*, 8437–8447.

[83] A. J. Cooper, N. R. Wilson, I. A. Kinloch, R. A. W. Dryfe, *Carbon* **2014**, *66*, 340–350.

[84] A. Yamakata, M. Osawa, *J. Am. Chem. Soc.* **2009**, *131*, 6892–6893.

[85] Y. Marcus, *J. Solution Chem.* **2008**, *37*, 1071–1098.

[86] H. O. House, E. Feng, N. P. Peet, *J. Org. Chem.* **1971**, *36*, 2371–2375.

[87] M. P. S. Mousavi, S. Kashefolgheta, A. Stein, P. Bühlmann, *J. Electrochem. Soc.* **2015**, *163*, H74–H80.

[88] J. S. Mayell, A. J. Bard, *J. Am. Chem. Soc.* **1963**, *85*, 421–425.

[89] W. Sirisaksoontorn, A. A. Adenuga, V. T. Remcho, M. M. Lerner, *J. Am. Chem. Soc.* **2011**, *133*, 12436–12438.

[90] Y. Kamihara, T. Watanabe, M. Hirano, H. Hosono, *J. Am. Chem. Soc.* **2008**, *130*, 3296–3297.

[91] M. Rotter, M. Pangerl, M. Tegel, D. Johrendt, *Angew. Chem. Int. Ed.* **2008**, *47*, 7949–7952.

[92] Q. Si, R. Yu, E. Abrahams, *Nat. Rev. Mater.* **2016**, *1*, 16017.

[93] A. Bergen, R. Andersen, M. Bauer, H. Boy, M. ter Brake, P. Brutsaert, C. Bührer, M. Dhallé, J. Hansen, H. ten Kate, J. Kellers, J. Krause, E. Krooshoop, C. Kruse, H. Kylling, M. Pilas, H. Pütz, A. Rebsdorf, M. Reckhard, E. Seitz, H. Springer, X. Song, N. Tzabar, S. Wessel, J. Wiezoreck, T. Winkler, K. Yagotyntsev, *Supercond. Sci. Technol.* **2019**, *32*, 125006.

[94] Z. Melhem, *High Temperature Superconductors (HTS) for Energy Applications*, Woodhead Publishing Ltd., **2012**, pp. 432.

[95] C. Yao, Y. Ma, *Supercond. Sci. Technol.* **2019**, *32*, 023002.

[96] H. Hosono, K. Tanabe, E. Takayama-Muromachi, H. Kageyama, S. Yamanaka, H. Kumakura, M. Nohara, H. Hiramatsu, S. Fujitsu, *Sci. Technol. Adv. Mater.* **2015**, *16*, 033503.

[97] H. Hosono, A. Yamamoto, H. Hiramatsu, Y. Ma, *Mater. Today* **2018**, *31*, 278–302.

[98] V. Zestrea, V. Y. Kodash, V. Felea, P. Petrenco, D. V. Quach, J. R. Groza, V. Tsurkan, *J. Mater. Sci.* **2008**, *43*, 660–664.

[99] J.-F. Ge, Z.-L. Liu, C. Liu, C.-L. Gao, D. Qian, Q.-K. Xue, Y. Liu, J.-F. Jia, *Nat. Mater.* **2015**, *14*, 285–289.

[100] G. R. Stewart, *Rev. Mod. Phys.* **2011**, *83*, 1589–1652.

[101] J. H. Tapp, Z. J. Tang, B. Lv, K. Sasmal, B. Lorenz, P. C. W. Chu, A. M. Guloy, *Phys. Rev. B* **2008**, *78*, 060505.

[102] M. Rotter, M. Tegel, D. Johrendt, *Phys. Rev. Lett.* **2008**, *101*, 107006.

[103] Z. A. Ren, G. C. Che, X. L. Dong, J. Yang, W. Lu, W. Yi, X. L. Shen, Z. C. Li, L. L. Sun, F. Zhou, Z. X. Zhao, *Epl* **2008**, *83*, 17002.

[104] A. Iyo, K. Kawashima, T. Kinjo, T. Nishio, S. Ishida, H. Fujihisa, Y. Gotoh, K. Kihou, H. Eisaki, Y. Yoshida, *J. Am. Chem. Soc.* **2016**, *138*, 3410–3415.

[105] X. Zhu, F. Han, G. Mu, P. Cheng, B. Shen, B. Zeng, H.-H. Wen, *Phys. Rev. B* **2009**, *79*, 220512.

[106] F.-C. Hsu, J.-Y. Luo, K.-W. Yeh, T.-K. Chen, T.-W. Huang, P. M. Wu, Y.-C. Lee, Y.-L. Huang, Y.-Y. Chu, D.-C. Yan, M.-K. Wu, *Proc. Natl. Acad. Sci. U.S.A.* **2008**, *105*, 14262–14264.

[107] S. Medvedev, T. M. McQueen, I. A. Troyan, T. Palasyuk, M. I. Eremets, R. J. Cava, S. Naghavi, F. Casper, V. Ksenofontov, G. Wortmann, C. Felser, *Nat. Mater.* **2009**, *8*, 630–633.

[108] Y. J. Zhou, A. J. Millis, *Phys. Rev. B* **2016**, *93*, 224506.

[109] Y. Miyata, K. Nakayama, K. Sugawara, T. Sato, T. Takahashi, *Nat. Mater.* **2015**, *14*, 775–779.

[110] J. Guo, S. Jin, G. Wang, S. Wang, K. Zhu, T. Zhou, M. He, X. Chen, *Phys. Rev. B* **2010**, *82*, 180520.

[111] D. P. Shoemaker, D. Y. Chung, H. Claus, M. C. Francisco, S. Avci, A. Llobet, M. G. Kanatzidis, *Phys. Rev. B* **2012**, *86*, 184511.

[112] A. Krzton-Maziopa, E. Pesko, R. Puzniak, *J. Phys. Condens. Matter* **2018**, *30*, 243001.

[113] X. Dong, H. Zhou, H. Yang, J. Yuan, K. Jin, F. Zhou, D. Yuan, L. Wei, J. Li, X. Wang, G. Zhang, Z. Zhao, *J. Am. Chem. Soc.* **2015**, *137*, 66–69.

[114] R. Sun, S. Jin, L. Gu, Q. Zhang, Q. Huang, T. Ying, Y. Peng, J. Deng, Z. Yin, X. Chen, *J. Am. Chem. Soc.* **2019**, *141*, 13849–13857.

[115] H.-S. Xu, X.-X. Wang, L.-L. Tang, K.-P. Yang, D. Yang, Y.-Z. Long, K.-B. Tang, *ChemistrySelect* **2018**, *3*, 7757–7762.

[116] M. Burrard-Lucas, D. G. Free, S. J. Sedlmaier, J. D. Wright, S. J. Cassidy, Y. Hara, A. J. Corkett, T. Lancaster, P. J. Baker, S. J. Blundell, S. J. Clarke, *Nat. Mater.* **2013**, *12*, 15–19.

[117] U. Pachmayr, F. Nitsche, H. Luetkens, S. Kamusella, F. Brückner, R. Sarkar, H.-H. Klauss, D. Johrendt, *Angew. Chem. Int. Ed.* **2015**, *54*, 293–297.

[118] J. P. Sun, M. Z. Shi, B. Lei, S. X. Xu, Y. Uwatoko, X. H. Chen, J. G. Cheng, *EPL-Europhys. Lett.* **2020**, *130*, 67004.

[119] A. E. Böhmer, F. Hardy, F. Eilers, D. Ernst, P. Adelmann, P. Schweiss, T. Wolf, C. Meingast, *Phys. Rev. B* **2013**, *87*, 180505.

[120] A. E. Böhmer, V. Taufour, W. E. Straszheim, T. Wolf, P. C. Canfield, *Phys. Rev. B* **2016**, *94*, 024526.

[121] D. Chareev, E. Osadchii, T. Kuzmicheva, J.-Y. Lin, S. Kuzmichev, O. Volkova, A. Vasiliev, *CrystEngComm* **2013**, *15*, 1989–1993.

[122] Q. Gao, O. Giraldo, W. Tong, S. L. Suib, *Chem. Mater.* **2001**, *13*, 778–786.

[123] Z.-h. Liu, Z.-M. Wang, X. Yang, K. Ooi, *Langmuir* **2002**, *18*, 4926–4932.

[124] A. Spek, *J. Appl. Crystallogr.* **2003**, *36*, 7–13.

[125] G. Kresse, J. Furthmüller, *Comput. Mater. Sci.* **1996**, *6*, 15–50.

[126] G. Kresse, J. Furthmüller, *Phys. Rev. B* **1996**, *54*, 11169–11186.

[127] G. Kresse, D. Joubert, *Phys. Rev. B* **1999**, *59*, 1758–1775.

[128] J. Sun, A. Ruzsinszky, J. P. Perdew, *Phys. Rev. Lett.* **2015**, *115*, 036402.

[129] A. Togo, I. Tanaka, *Scripta Mater.* **2015**, *108*, 1–5.

[130] G. L. Bottger, A. L. Geddes, *Spectrochim. Acta* **1965**, *21*, 1701–1708.

[131] A. Kornath, O. Blecher, F. Neumann, R. Ludwig, *J. Mol. Spectrosc.* **2003**, *219*, 170–174.

# 3. Solid-state synthesized [(Li$_{0.88}$Fe$_{0.12}$)OH]FeSe and [LiOH](Fe)$_z$FeSe

## Introduction

The discovery of iron-based superconductors led to an intensive search for new high-temperature superconducting materials, wide investigations of their superconducting mechanism and the development of various applications.[1-6] Among the iron-based 11-type superconductors $\beta$-FeSe[2] is interesting due to its fascinating properties like coexistence of superconductivity with nematic order or absence of antiferromagnetic (AFM) transition at ambient temperatures.[7-14] $\beta$-FeSe is a structurally simple binary superconductor, consisting of layers of edge-sharing $FeSe_{4/4}$ tetrahedra (*anti*-PbO type), with a critical temperature ($T_c$) of 8 K at ambient pressure.[2] Furthermore, researchers also found that chemical substitution of selenium by sulfur and tellurium enhanced the $T_c$ to 10–15 K.[15-17] However, doping $\beta$-FeSe with small amounts (three wt. %) of copper or cobalt suppresses the superconductivity. Williams *et al.* discovered that the superconductivity of $\beta$-FeSe is extremely sensitive to the content and disorder of iron and that a selenium deficiency might play a role.[18-19]

The $T_c$ is remarkably modifiable, e.g., increasing it up to 37 K by applying external pressure[20] or growing monolayers of $\beta$-FeSe on $SrTiO_3$ and reaching critical temperatures as high as 65–100 K.[21-24] Critical temperatures up to 50 K are possible by cointercalating organic molecules as spacer and alkaline metals as electron donors into $\beta$-FeSe.[25-34] Overall, in FeSe-based superconductors, the crystal structure directly influences its magnetism, nemacity and superconductivity.[8, 10, 13-14, 20, 35-37] Various mechanisms have been suggested as decisive parameters for superconducting properties, like the separation of the $FeSe_{4/4}$ layers,[38] the distortion of the $FeSe_{4/4}$ unit and the deviation of the anion height from the optimum value (1.38 Å).[39] A global understanding of FeSe-based superconductors is still missing. Therefore, it is desirable to develop new compounds to enhance the understanding of the favourable synthesis and superconducting conditions.

Lu *et al.* established in 2014 the synthesis of $LiFeO_2(FeSe)_2$ under hydrothermal conditions.[39] The reported compound is superconducting below 43 K. Shortly after, researchers proved that the structure consists of hydroxide instead of oxide layers between the $FeSe_{4/4}$ layers, $[(Li_{0.8}Fe_{0.2})OH]FeSe$.[40-41] The FeSe-based superconductor [(Li,Fe)OH]FeSe crystalizes in the tetragonal space group *P*4/*nmm* (no. 129 O1) with $a = 3.79$ Å and $c = 9.22$ Å.

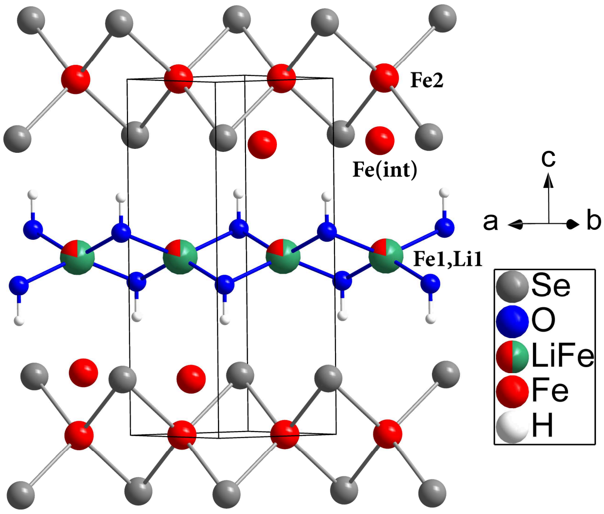

**Figure 3-1.**Crystal structure of $[(Li_{0.8}Fe_{0.2})OH]FeSe$[41] with the mixed occupied site Fe1/Li1, the Fe2 site in the $FeSe_{4/4}$ layer. The Fe(int) site is a probable location site for interstitial iron.[42]

The structure is composed of edge-sharing $FeSe_{4/4}$ tetrahedra layers that alternate with edge-sharing $(Li_{0.8}Fe_{0.2})OH$ tetrahedra layers (see Figure 3-1). The $(Li_{0.8}Fe_{0.2})OH$ layer is structurally very similar to LiOH, which like $\beta$-FeSe also crystallizes in the *anti*-PbO type.[43] The structure consists of two different iron sites (see Figure 3-1), i.e. Fe1 ions in the (Li,Fe)OH layer and Fe2 ions in the $FeSe_{4/4}$ layer. Furthermore, iron vacancies can be found in the $FeSe_{4/4}$ layers and mixed occupation Li/Fe sites (Fe1/Li1, see Figure 3-1) in the (Li,Fe)OH layer. The vacancies [44-45] and the mixed occupation have an influence on the magnetic and superconducting properties of $[(Li_{0.8}Fe_{0.2})OH]FeSe$.[46-47] This compound demonstrates the coexistence of superconductivity and antiferromagnetism (AFM)[40, 48] or ferromagnetism (FM)[41, 49]. Post-synthetic lithiation increases the lithium occupation on the Li1 site and the expelled iron fills iron vacancies in the $FeSe_{4/4}$ layers. This can induce high-temperature superconductivity at 43 K in samples with lower $T_c$ (0–25 K).[44] Furthermore, post-synthetic lithiation has shown that these superconducting samples consist of near stoichiometric $FeSe_{4/4}$ layers ($y < 0.05$ in $[(Li_{0.8}Fe_{0.2})OH]Fe_{1-y}Se$) and the iron in the layers is reduced below the oxidation state +2.[44-45] According to Chen *et al.* higher $T_c$ are reachable through the amount of iron in the hydroxide layer e.g., through a charge transfer of electrons into the $FeSe_{4/4}$ layer.[50-51] Chemical control over the superconducting properties is gained through optimizations steps (synthesis and post-synthetic modifications).[52-57] Some years later (2019) Hu *et al.* reported a new synthesis route to $[(Li_{0.6}Fe_{0.4})OH]FeSe$ with a solid-state reaction of LiOH and $\beta$-FeSe.[58] They induced superconductivity in their samples *via* post-synthetic modifications by iron vacancy tuning. This opened a new synthetic pathway to [(Li,Fe)OH]FeSe and similar intercalated layered compounds.

This chapter reports the low temperature solid-state synthesis of [($Li_{0.88}Fe_{0.12}$)OH]FeSe from $\beta$-FeSe and excess LiOH. Hereby, two different phases have been discovered, [($Li_{0.88}Fe_{0.12}$)OH]FeSe and [LiOH](Fe)$_z$FeSe, where [LiOH](Fe)$_z$FeSe has a significantly elongated $c$-axis. They extend the [(Li,Fe)OH]FeSe structure family. The dependence of the superconductivity in [($Li_{0.88}Fe_{0.12}$)OH]FeSe on the occupation of the (Li,Fe)OH layer and vacancies in the $FeSe_{4/4}$ layer is presented. Furthermore, a possible explanation for the elongation of the $c$-axis in [LiOH](Fe)$_z$FeSe is given.

## Experimental

[(Li,Fe)OH]FeSe phases were synthesized *via* solid-state reaction. The ratio of the educts was varied, but the ratio of 1:3 of $\beta$-FeSe (0.05 g, 0.371 mmol, 1 eq.) to LiOH (0.026 g, 1.113 mmol, 3 eq., ALFA AESAR, 99.995 %) was most successful. First, the polycrystalline starting material $\beta$-FeSe was prepared by mixing iron (437.8 mg, CHEMPUR, 99.9 %) und selenium (562.4 mg, CHEMPUR, 99.999 %) in an atomic ratio of 1.1:1 and sealing it in an evacuated glass ampoule together with a eutectic mixture of $AlCl_3$ (7.75 g, GRÜSSING, 99.5 %) and KCl (2.25 g, ALFA AESAR, 99.985 %). While heating the ampoule to 390 °C at the one end, the other end was kept at 280 °C for 5–10 days. The flux was removed by washing with water and ethanol. The obtained polycrystalline powder was dried over vacuum. Afterwards $\beta$-FeSe and excess LiOH were ground together and then sealed in an evacuated quartz ampoule. The solid-state reaction proceeded at 450 °C for 60 h. Heating rates were either 20 °C/h or higher than 100 °C/h. Depending on various factors of the synthesis different products resulted.

The powder X-Ray patterns were measured either by a STOE Stadi-P diffractometer (Mo-$K_{\alpha1}$) equipped with a STOE Mythen 1k detector or a HUBER G670 diffractometer (Cu-$K_{\alpha1}$) at room temperature. Rietveld refinements were done with TOPAS.[59] Magnetization isotherms and susceptibility measurements were performed on a Physical Property Measurement System (PPMS-9, Quantum Design) with a vibrating sample magnetometer (VSM). Zero-field cooled and field-cooled measurements were conducted between 2 K and 100 K and an applied field of 15 Oe. The isothermal magnetization was measured at 2 K and 300 K ($H = \pm 50$ kOe). M. Döblinger, LMU Munich, performed transmission electron microscopy measurements (TEM) on a Cs-corrected transmission electron microscope FEI TITAN THEMIS with field emission cathode and CMOS camera FEI CETA. With a windowless four-quadrant

SUPERX detector EDS measurements were carried out. Results were analysed with the program ESVISON.[60]

## Results and Discussion

According to the literature $[(Li,Fe)OH]FeSe$ can be prepared either hydrothermally, *via* ion exchange or *via* solid-state synthesis.[41, 53, 58, 61] Focusing on the solid-state route Hu *et al.* synthesized $[(Li_{0.6}Fe_{0.4})OH]Fe_{0.7}Se$ at 250–300 °C for five to ten days with a stoichiometric amount of $\beta$-FeSe and LiOH.[58] Attempts to reproduce $[(Li_{0.6}Fe_{0.4})OH]Fe_{0.7}Se$ using the literature protocol by Hu *et al.* did not result in the desired product. Apparently, the synthesis is very sensitive to various parameters like heating rate, ratio of the educts, holding temperature and holding time. However, a solid-state synthesis route to $[(Li_{0.88}Fe_{0.12})OH]FeSe$ and $[LiOH](Fe)_zFeSe$ could be established starting from $\beta$-FeSe and excess LiOH. One important aspect in this synthesis is the crucible material or the lack thereof. Standard solid-state reactions often take place in some sort of crucibles, e.g., $Al_2O_3$, niobium or glassy carbon. However, reactions in any kind of crucible produced several other products like $Li_2FeSeO$,[62] but not the desired product. Therefore, all reactions took directly place in quartz ampoules. Furthermore, the synthesis is prone to side phases. Impurities like $LiFeO_2$, $Fe_3Se_4$ and hexagonal $\delta$-FeSe (NiAs-type)[63-64] can occur.

On the one hand, the binary phase diagram of iron-selenium[65-66] shows that the tetragonal $\beta$-FeSe phase has a narrow phase width and has only a very small range of stability ($300\ K < T < 450\ K$).[19] It also converts easily to $\delta$-FeSe at 500 °C.[67] Therefore, the compounds contained iron selenide side phases after annealing. On the other hand, most of the other impurities were lithium-containing side phases due to the excess of LiOH. These side phases are likely the thermodynamically favoured products formed between 300–500 °C. Below 300 °C side phases diminish, but also the yields of $[(Li_{0.88}Fe_{0.12})OH]FeSe$ are low. However, through solid-state synthesis, yields up to 81 wt. % for $[(Li_{0.88}Fe_{0.12})OH]FeSe$ could be achieved. The ratio of FeSe to LiOH was 1:3 and the optimal temperature was 450 °C. During the optimization of the synthesis two $[(Li,Fe)OH]FeSe$ phases arose, $[(Li_{0.88}Fe_{0.12})OH]FeSe$ and $[LiOH](Fe)_zFeSe$. The optimization process clearly depicts that $[LiOH](Fe)_zFeSe$ only occurs with an excess of LiOH and a heating rate greater or equal to 100 °C/h. Separating the second phase *via* synthesis from $[(Li_{0.88}Fe_{0.12})OH]FeSe$ was not possible. In some samples both phases are evident. Others contained just $[(Li_{0.88}Fe_{0.12})OH]FeSe$ and other side phases (see Figure 3-2). The coexistence of both [(Li,Fe)OH]FeSe phases could be attributed to an excess of lithium ions, which leads to phases with higher lithium content.

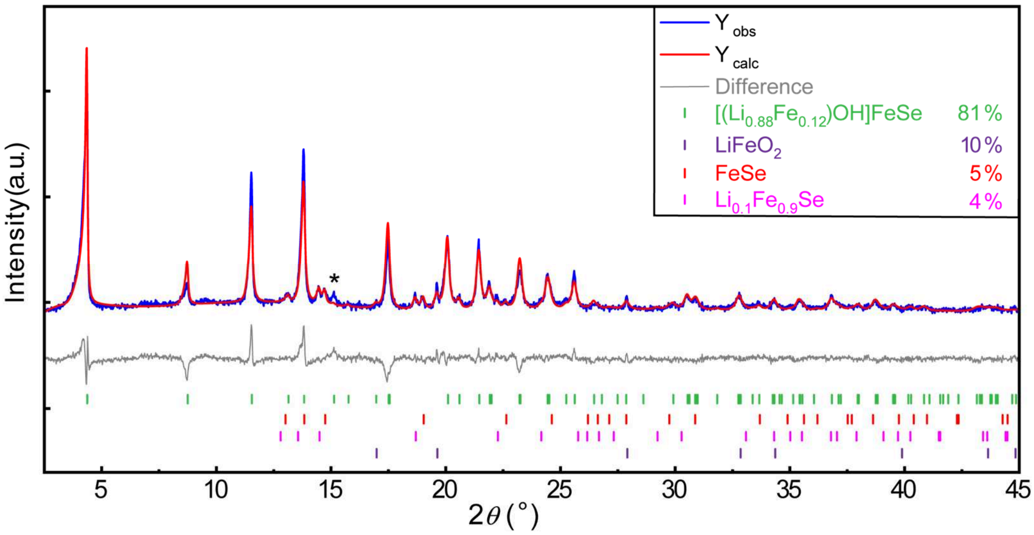

**Figure 3-2**. Powder X-Ray pattern of [($Li_{0.88}Fe_{0.12}$)OH]FeSe (Mo-$K_{\alpha1}$) sample (green ticks) with Rietveld-fit (red line) and difference curve (grey line) with impurities of $LiFeO_2$ (purple ticks), hexagonal FeSe (red ticks) and $Li_{0.1}Fe_{0.9}Se$ (magenta ticks). An unassignable reflection is marked with an asterisk.

To determine the crystal structure of the two [(Li,Fe)OH]FeSe phases, powder X-Ray diffraction experiments were conducted. The powder X-Ray diffractogram in Figure 3-3 depicts the [($Li_{0.88}Fe_{0.12}$)OH]FeSe and [LiOH](Fe)$_z$FeSe besides LiOH.

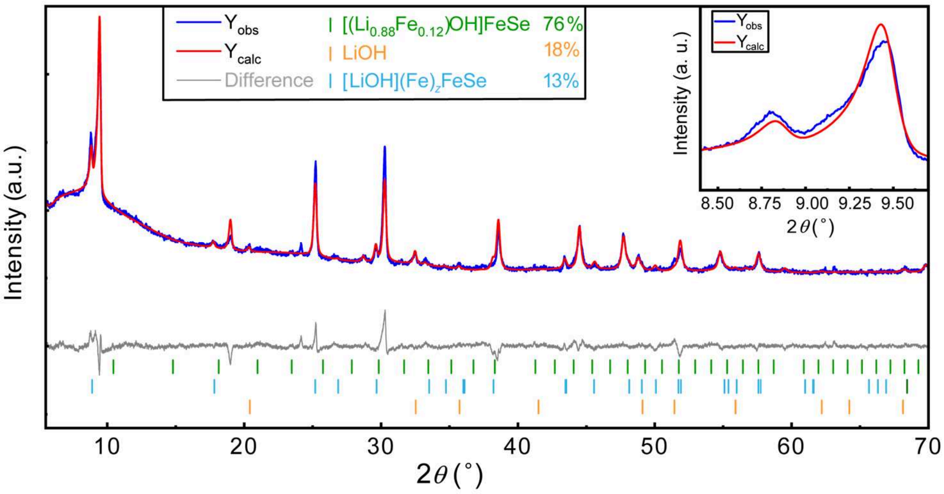

**Figure 3-3**. Powder X-Ray pattern containing both phases [($Li_{0.88}Fe_{0.12}$)OH]FeSe (Cu-$K_{\alpha1}$) (green ticks) and [LiOH](Fe)$_z$FeSe (blue ticks) with a Rietveld-fit (red line) and difference curve (grey line) with the impurity of LiOH (orange ticks). The inset shows the enlargement of the [001] reflection at 9.34° $2\theta$.

Rietveld refinements showed that both phases could be indexed with tetragonal symmetry and subsequently refined in the space group *P*4/*nmm*. Additional TEM measurements (Chapter A.2, Figure A-4) confirmed the tetragonal symmetry. Furthermore, Rietveld refinement confirmed the structure model of [(Li,Fe)OH]FeSe for both phases. However, they vary in lattice parameters and composition (see Table 3-1). The lattice parameters for $[(Li_{0.88}Fe_{0.12})OH]FeSe$ are $a = 3.81$ Å and $c = 9.31$ Å. Additional peaks were indexed with a different unit cell and refined to the composition of $[LiOH](Fe)_zFeSe$. Further details are listed in Table A–4 to Table A–8.

**Table 3-1.** Crystallographic parameters, occupation, volume and superconductivity of the [(Li,Fe)OH]FeSe samples in comparison with literature data.[41, 58]

| | $[(Li_{0.88}Fe_{0.12})OH]FeSe$ | $[LiOH](Fe)_zFeSe$ | $[(Li_{0.8}Fe_{0.2})OH]FeSe$ | $[(Li_{0.6}Fe_{0.4})OH]FeSe$ |
|---|---|---|---|---|
| ***a* (Å)**[a] | 3.80548(5) | 3.7774(4) | 3.8038(1) | 3.82856(2) |
| ***c* (Å)**[a] | 9.3077(5) | 9.945(3) | 9.2210(6) | 9.16239(9) |
| **Occ. Li**[a] | 0.879(5) | 1.000(4) | 0.795(5) | 0.585(0) |
| **Occ. Fe1**[a] | 0.121 | 0 | 0.205 | 0.415 |
| **Occ. Fe2** [a] | 1.000(2) | 1.000(3) | 0.922(3) | 0.703(0) |
| ***c*/*a*** | 2.46 | 2.62 | 2.43 | 2.39 |
| ***V* (Å³)** | 134.9(1) | 141.8(1) | 133.1(1) | 130.3(1) |
| **$T_c$ (K)**[b] | – | – | 43 | – |

The phase compositions of $[(Li_{0.88}Fe_{0.12})OH]Fe_{1.0}Se$ and $[Li_{1.0}OH](Fe)_zFe_{1.0}Se$ were extracted from refined powder X-Ray diffraction data. The energy dispersive X-Ray spectroscopy (EDS) measurements confirmed the composition of iron, selenium and oxygen (see Chapter A.2, Table A-9 and Figure A-5). Iron occupations at the Fe1 site (see Figure 3-1) in $[(Li_{0.88}Fe_{0.12})OH]FeSe$, revealed less iron (0.121 vs 0.205 and 0.415) in comparison to literature data. No iron vacancies are evident in the $FeSe_{4/4}$ layer. For $[LiOH](Fe)_zFeSe$ the powder X-Ray refinement shows no iron in the hydroxide layer and no vacancies in the $FeSe_{4/4}$ layer. The value for *z* could not be determined with these analysis methods. Comparing $[(Li_{0.88}Fe_{0.12})OH]FeSe$ with the hydrothermally synthesized $[(Li_{0.8}Fe_{0.2})OH]FeSe$[41] ($a = 3.80$ and $c = 9.22$ Å) the *a*-axis displays almost no change, but the *c*-axis (9.3077(5) Å) slightly expands. Furthermore, the $LiO_{4/4}$ tetrahedra show no significant expansion

---

[a] Lattice parameters and compositions taken from Rietveld refinement of powder diffraction data.

[b] $T_c$ taken at 100 Oe from zero points of the second derivative of susceptibility measurements.

compared with hydrothermally synthesized $[(Li_{0.8}Fe_{0.2})OH]FeSe$[41] (Li–O: 1.9228(8) Å, 2.1820(9) Å vs. 1.920(7) Å, 2.18(2) Å). The difference in the tetrahedra height is approximately 1.03 %. The second phase, $[LiOH](Fe)_zFeSe$, shows similar values (3.78 Å) for the *a*-axis compared with samples synthesized hydrothermally (3.80 Å)[41] and through solid-state reactions by Hu *et al.* (3.82 Å)[58]. However, the *c*-axis is significantly elongated to 9.95 Å (Δ~7.34 %). This elongation is also prominent in the powder X-Ray pattern where all reflections with $l \neq 0$ shift. The greatest shift is noticeable in the [001] diffraction peak (from 9.35° $2\theta$ to 8.72° $2\theta$) (see inset Figure 3-3). In contrast to $[(Li_{0.88}Fe_{0.12})OH]FeSe$ there is a greater distortion of the $LiO_{4/4}$ tetrahedra. The height of the layer differs around 20 % (Li–O: 1.8934(1) Å, 2.30(1) Å vs. 1.920(7) Å, 2.18(2) Å).

Regarding the $[LiOH](Fe)_zFeSe$ phase, the elongation is significant (9.945(3) Å, Δ~7.34 %). Similar phases have been already reported for some hydrothermally synthesized products (9.7649(6) Å) and for some electric field tuned samples (10.179 Å).[42, 44] However, the crystal structure is not yet solved nor its properties determined. Theses phases mostly arise if the lithium content is significantly increased. There are several different approaches to achieve this such as using excess of LiOH or using an electric field *via* solid ion conductor field-effect transistors (SIC-FET).[42, 44-45, 58] The consensual opinion in the literature is that the excess lithium is preferentially located in the hydroxide layer (equation 1). The occupation refinements validate this scenario (see Table 3-1).

$$[(Li_{1-x}Fe_x)OH]Fe_{1-y}Se + y\,Li \rightarrow [(Li_{1-x+y}Fe_{x-y})OH]FeSe \qquad \text{Equation 1}$$

As a consequence of equation 1 iron is dislocated from the (Li,Fe)OH layer. A probable scenario is that the dislocated iron fills up the vacancies in the $FeSe_{4/4}$ layer. Then once filled up, it is expelled as atomic iron (equation 2).[44]

$$\left[\left(Li_{1-x+y}Fe_{x-y}\right)OH\right]FeSe + z\,Li \rightarrow \left[\left(Li_{1-x+y+z}Fe_{x-y-z}\right)OH\right]FeSe + z\,Fe \qquad \text{Equation 2}$$

However, the utilized starting material *β*-FeSe already contains no vacancies and there is no elemental iron evident in the powder patterns. Therefore, this scenario does not fit the results. Alternatively, the iron could migrate to interstitial sites near the $FeSe_{4/4}$ layer (see Figure 3-1, Fe(int)), as proposed by equation 3.

$$[(Li_{1-x+y}Fe_{x-y})OH]FeSe + z\,Li \rightarrow Fe_z(Li_{1-x+y+z}OH)FeSe \qquad \text{Equation 3}$$

Ma *et al.* described the scenario of equation 3 with the support of DFT calculations. They assumed the existence of $Fe_z(LiOH)FeSe$ ($z = 0.2$) as an insulator (equation 3).[42] Furthermore, the proposed migrations to interstitial sites is probable because in $Fe_{1+x}(Te,Se)$ a similar location of iron at the interstitial sites has been observed by STM.[15-16, 68]

In $[LiOH](Fe)_zFeSe$ the elongation is due to the strong distortion of the $LiO_{4/4}$ tetrahedra. However, the distortion is not sufficient to completely explain the elongation, because the *c* axis is still longer (9.6043 vs. 9.945(3) Å) than in post-synthetically modified hydrothermal Li(OH)FeSe. Even though the literature compound has also full-occupied LiOH layers and no vacancies.[45] This could indicate that $[LiOH](Fe)_zFeSe$ contains – like in the proposal of Ma *et al.* – an additional interstitial site.[42] This site could contain iron, possibly lithium or a mixed occupation of both. The lithium would stem from the excess LiOH (1:3) and it is more available than iron. Some $\beta$-FeSe needs to decompose to gain iron, which than migrates to the interstitial sites or builds up side phases such as $LiFeO_2$. The value of $z$ in $[LiOH](Fe)_zFeSe$ would be smaller than the 0.2, because here the *c* lattice (9.945(3) Å vs. 10.1792 Å) is shorter and less iron is available in the synthesis. For a validation of this proposal, single crystal X-Ray analysis is necessary, but due to the low crystallinity of the samples and the very small sizes of the single crystals it was not possible.

### Magnetism

Magnetic measurements of samples containing only the main phase $[(Li_{0.88}Fe_{0.12})OH]FeSe$ and side phases as well as for samples with both phases were performed (see Chapter A.2, Figure A-7 and Figure A-8). The measured samples differ from the above-plotted ones as they both contain $LiFeO_2$ as magnetic active side phase. The magnetic measurements for samples containing both phases show hardly any differences to phases with only $[(Li_{0.88}Fe_{0.12})OH]FeSe$ and the side phases (see Chapter A.2, Figure A-9). Therefore, the focus lies on the measurements with $[(Li_{0.88}Fe_{0.12})OH]FeSe$ and $[LiOH](Fe)_zFeSe$ because fewer side phases are apparent. Isothermal magnetization plots at 300 and 1.9 K follow a linear trend and appear to be paramagnetic. Furthermore, they display small values of $\mu/\mu_B$ and show no hysteresis (see Figure 3-4).

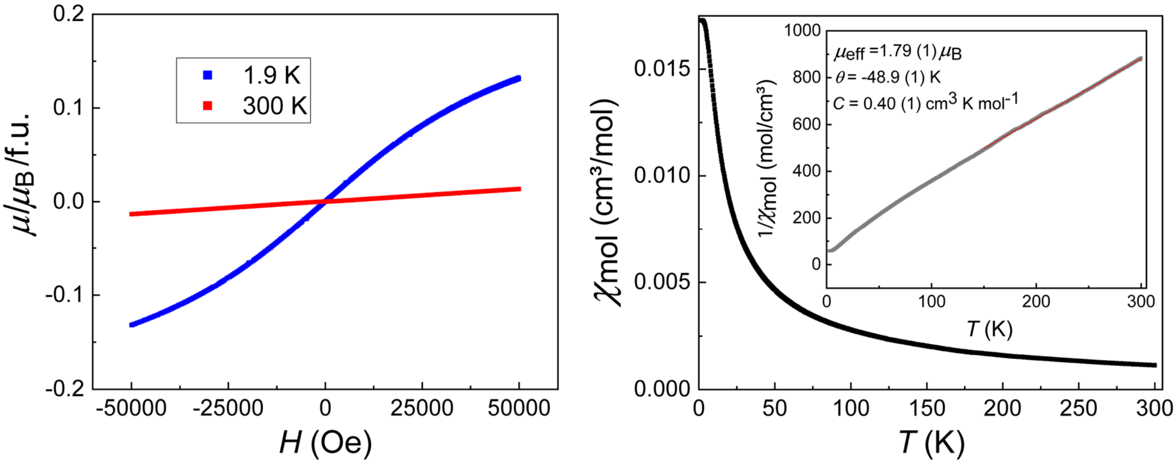

**Figure 3-4**. Isothermal magnetization of [($Li_{0.88}Fe_{0.12}$)OH]FeSe, [LiOH](Fe)$_z$FeSe and side phases at 300 and 1.9 K (left) and magnetic susceptibilities (black) and inverse susceptibilities (inset) (right). $B$ = 3 T. Curie-Weiss fit in red. Parameters obtained from the fit are given in the inset.

A plot of the inverse susceptibility versus temperature permits a Curie-Weiss fit from 150–300 K. The measurement range below 150 K is excluded because the graph significantly diverges here from linear behaviour and thus an ideal paramagnetic one. The resulting effective magnetic moment $\mu_{eff}$ is 1.74(1) $\mu_B$ per formula unit. The side phase $LiFeO_2$[69] also shows paramagnetic properties. [($Li_{0.88}Fe_{0.12}$)OH]FeSe and [LiOH](Fe)$_z$FeSe might have a paramagnetic magnetic contribution but the paramagnetic behaviour can also be attributed to the 10 % side phase $LiFeO_2$. Additionally, ZFC/FC measurements show no superconductivity in [($Li_{0.88}Fe_{0.12}$)OH]FeSe as well as in [LiOH](Fe)$_z$FeSe.

For hydrothermally synthesized samples of [(Li,Fe)OH]FeSe, there are numerous studies on its superconductivity. In the literature there are reports about non-superconducting as well as superconducting [(Li,Fe)OH]FeSe samples with $T_c$ in a range of 15–43 K.[44-45, 52, 54, 56, 70-71] According to Sun *et al.* an iron-rich synthesis is necessary for superconducting samples ($V$ < 133.2 Å³ and $c/a$ > 2.43). Whereas iron-poor synthesis yield non-superconducting samples with a bigger unit cell volume and a smaller $c/a$ ratio.[45] The values of [($Li_{0.88}Fe_{0.12}$)OH]FeSe only meet one of the two criteria (134.9 Å³ and 2.46). This might already indicate an issue for the superconductivity. With regard to the samples containing [LiOH](Fe)$_z$FeSe, the values for both parameters increase (volume and $c/a$, 141.8 Å³and 2.62) and therefore do not fit these criteria.

Furthermore, in hydrothermally synthesized [($Li_{1-x}Fe_x$)OH]$Fe_{1-y}$Se superconductivity only occurs with $x \sim 0.2$ and with iron vacancies ($y$ < 5 %) in the $FeSe_{4/4}$ layer.[25, 45, 72] Essentially, for a sample to become superconducting, it must have sufficient electron doping ($x$) and only a few vacancies in the $FeSe_{4/4}$ layer. In Figure 3–4 [($Li_{0.88}Fe_{0.12}$)OH]FeSe and [LiOH](Fe)$_z$FeSe are classified according to literature compounds with respect to the lattice parameter $c$ and occupation in the ($Li_{1-x}Fe_x$)OH layer.

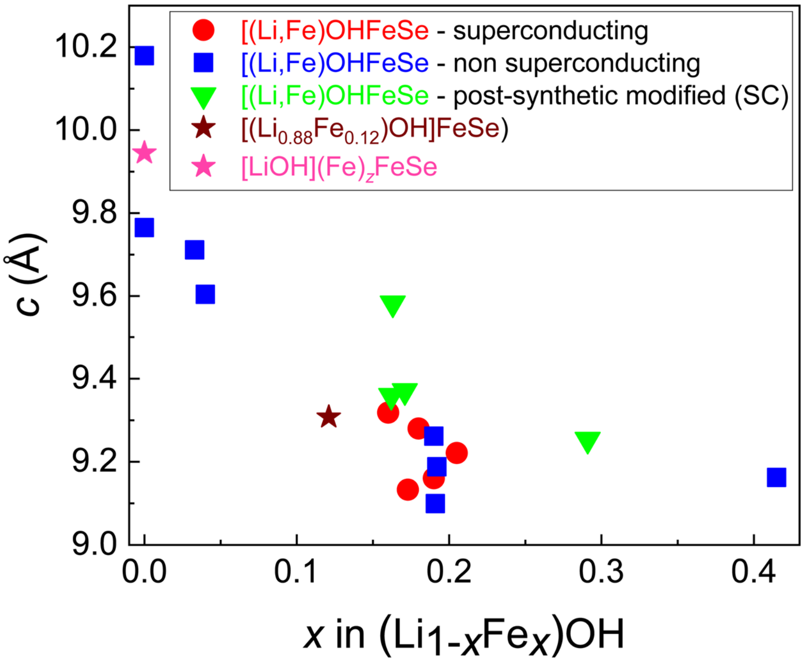

**Figure 3-4.** [($Li_{0.88}Fe_{0.12}$)OH]FeSe (brown asterisk) and [LiOH](Fe)$_z$FeSe (pink asterisk) in comparison with [(Li,Fe)OH]FeSe compounds regarding their $c$ lattice parameter and the iron ($x$) occupation in the ($Li_{1-x}Fe_x$)OH layer. [(Li,Fe)OH]FeSe can be superconducting (red dot), superconducting after post-synthetic modification (green triangle) and non-superconducting (blue square).

The figure shows [($Li_{0.88}Fe_{0.12}$)OH]FeSe besides a clustering of [(Li,Fe)OH]FeSe compounds with $x \sim 0.2$. Looking at the occupancy in the ($Li_{0.88}Fe_{0.12}$)OH layer there is a slightly higher lithium occupation (Li : Fe, 0.879:0.121) compared to superconducting [($Li_{0.8}Fe_{0.2}$)OH]FeSe (0.795:0.205). This lower iron occupancy ($x = 0.121$) in the hydroxide layer diminishes the charge doping effect to the $FeSe_{4/4}$ layer. Furthermore, no iron vacancies (site Fe2) are detected in the $FeSe_{4/4}$ layer. The full occupancy of the iron site in the $FeSe_{4/4}$ layer as well as the lower electron doping from the ($Li_{1-x}Fe_x$)OH layer is not sufficient to support superconductivity. As depicted in Figure 3–4 [LiOH](Fe)$_z$FeSe can be clustered together with other [(Li,Fe)OH]FeSe compounds with long $c$-axis (9.6–10.18 Å) and low iron occupancies ($x = 0$–$0.04$). All these compounds show no superconducting transition. For the [LiOH](Fe)$_z$FeSe, no iron can be refined in the hydroxide layer ($x = 0$). Based on the available data, the reasons for the lack of superconductivity of [LiOH](Fe)$_z$FeSe cannot be determined yet.

### Conclusions

In summary, $[(Li_{0.88}Fe_{0.12})OH]FeSe$ and $[LiOH](Fe)_zFeSe$ were successfully synthesized *via* a solid-state reaction at low temperatures with yields up to 85 wt. % or 30 wt. %, respectively. Hereby the [(Li,Fe)OH]FeSe structure family was extended. They exhibit different properties than the known [(Li,Fe)OH]FeSe compounds. This is particularly evident in crystal structure parameters, occupancies, distortion of the layers, magnetic properties and absence of superconductivity. In $[(Li_{0.88}Fe_{0.12})OH]FeSe$, the absence of superconductivity might be due to a higher lithium occupation in the $(Li_{0.88}Fe_{0.12})OH$ layer and therefore a lower charge doping of the $FeSe_{4/4}$ layer. In $[LiOH](Fe)_zFeSe$, the elongation of the lattice parameter $c$ is due to the strong distortion of the $LiO_{4/4}$ tetrahedra. Additionally, a possible incorporation of interstitial iron/lithium might further explain this increase, but this needs to be further investigated e.g. by single crystal diffractometry experiments.

## References

[1] Y. Kamihara, T. Watanabe, M. Hirano, H. Hosono, *J. Am. Chem. Soc.* **2008**, *130*, 3296–3297.

[2] F.-C. Hsu, J.-Y. Luo, K.-W. Yeh, T.-K. Chen, T.-W. Huang, P. M. Wu, Y.-C. Lee, Y.-L. Huang, Y.-Y. Chu, D.-C. Yan, M.-K. Wu, *Proc. Natl. Acad. Sci. U.S.A.* **2008**, *105*, 14262–14264.

[3] M. Rotter, M. Tegel, D. Johrendt, *Phys. Rev. Lett.* **2008**, *101*, 107006.

[4] M. Ren, Y. Yan, X. Niu, R. Tao, D. Hu, R. Peng, B. Xie, J. Zhao, T. Zhang, D.-L. Feng, *Sci. Adv.* **2017**, *3*, e1603238.

[5] C. Yao, Y. Ma, *Supercond. Sci. Technol.* **2019**, *32*, 023002.

[6] G. Biswal, K. L. Mohanta, *Mater. Today Proc.* **2020**, *35*, 207–215.

[7] M. Bendele, A. Amato, K. Conder, M. Elender, H. Keller, H. H. Klauss, H. Luetkens, E. Pomjakushina, A. Raselli, R. Khasanov, *Phys. Rev. Lett.* **2010**, *104*, 087003.

[8] M. Bendele, A. Ichsanow, Y. Pashkevich, L. Keller, T. Strässle, A. Gusev, E. Pomjakushina, K. Conder, R. Khasanov, H. Keller, *Phys. Rev. B* **2012**, *85*, 064517.

[9] M. D. Watson, T. K. Kim, A. A. Haghighirad, N. R. Davies, A. McCollam, A. Narayanan, S. F. Blake, Y. L. Chen, S. Ghannadzadeh, A. J. Schofield, M. Hoesch, C. Meingast, T. Wolf, A. I. Coldea, *Phys. Rev. B* **2015**, *91*, 155106.

[10] S. Knöner, D. Zielke, S. Köhler, B. Wolf, T. Wolf, L. Wang, A. Böhmer, C. Meingast, M. Lang, *Phys. Rev. B* **2015**, *91*, 174510.

[11] A. E. Böhmer, V. Taufour, W. E. Straszheim, T. Wolf, P. C. Canfield, *Phys. Rev. B* **2016**, *94*, 024526.

[12] K. Liu, Z.-Y. Lu, T. Xiang, *Phys. Rev. B* **2016**, *93*, 205154.

[13] U. S. Kaluarachchi, V. Taufour, A. E. Böhmer, M. A. Tanatar, S. L. Bud'ko, V. G. Kogan, R. Prozorov, P. C. Canfield, *Phys. Rev. B* **2016**, *93*, 064503.

[14] A. E. Böhmer, A. Kreisel, *J. Phys. Condens. Matter* **2017**, *30*, 023001.

[15] T. J. Liu, X. Ke, B. Qian, J. Hu, D. Fobes, E. K. Vehstedt, H. Pham, J. H. Yang, M. H. Fang, L. Spinu, P. Schiffer, Y. Liu, Z. Q. Mao, *Phys. Rev. B* **2009**, *80*, 174509.

[16] J. X. Yin, Z. Wu, J. H. Wang, Z. Y. Ye, J. Gong, X. Y. Hou, L. Shan, A. Li, X. J. Liang, X. X. Wu, J. Li, C. S. Ting, Z. Q. Wang, J. P. Hu, P. H. Hor, H. Ding, S. H. Pan, *Nat. Phys.* **2015**, *11*, 543–546.

[17] Z. Guo, F. Sun, Y. Chen, Y. Mao, L. Wan, X. Yan, Y. Yang, W. Yuan, *CrystEngComm* **2019**, *21*, 2994–2999.

[18] A. J. Williams, T. M. McQueen, R. J. Cava, *Solid State Commun.* **2009**, *149*, 1507–1509.

[19] T. M. McQueen, Q. Huang, V. Ksenofontov, C. Felser, Q. Xu, H. Zandbergen, Y. S. Hor, J. Allred, A. J. Williams, D. Qu, J. Checkelsky, N. P. Ong, R. J. Cava, *Phys. Rev. B* **2009**, *79*, 014522.

[20] S. Medvedev, T. M. McQueen, I. A. Troyan, T. Palasyuk, M. I. Eremets, R. J. Cava, S. Naghavi, F. Casper, V. Ksenofontov, G. Wortmann, C. Felser, *Nat. Mater.* **2009**, *8*, 630–633.

[21] Q.-Y. Wang, Z. Li, W.-H. Zhang, Z.-C. Zhang, J.-S. Zhang, W. Li, H. Ding, Y.-B. Ou, P. Deng, K. Chang, J. Wen, C.-L. Song, K. He, J.-F. Jia, S.-H. Ji, Y.-Y. Wang, L.-L. Wang, X. Chen, X.-C. Ma, Q.-K. Xue, *Chin. Phys. Lett.* **2012**, *29*, 037402.

[22] S. He, J. He, W. Zhang, L. Zhao, D. Liu, X. Liu, D. Mou, Y.-B. Ou, Q.-Y. Wang, Z. Li, L. Wang, Y. Peng, Y. Liu, C. Chen, L. Yu, G. Liu, X. Dong, J. Zhang, C. Chen, Z. Xu, X. Chen, X. Ma, Q. Xue, X. J. Zhou, *Nat. Mater.* **2013**, *12*, 605–610.

[23] J.-F. Ge, Z.-L. Liu, C. Liu, C.-L. Gao, D. Qian, Q.-K. Xue, Y. Liu, J.-F. Jia, *Nat. Mater.* **2015**, *14*, 285–289.

[24] X. Shi, Z. Q. Han, X. L. Peng, P. Richard, T. Qian, X. X. Wu, M. W. Qiu, S. C. Wang, J. P. Hu, Y. J. Sun, H. Ding, *Nat. Commun.* **2017**, *8*, 14988.

[25] M. Burrard-Lucas, D. G. Free, S. J. Sedlmaier, J. D. Wright, S. J. Cassidy, Y. Hara, A. J. Corkett, T. Lancaster, P. J. Baker, S. J. Blundell, S. J. Clarke, *Nat. Mater.* **2012**, *12*, 15–19.

[26] A. Krzton-Maziopa, E. V. Pomjakushina, V. Y. Pomjakushin, F. von Rohr, A. Schilling, K. Conder, *J. Phys. Condens. Matter* **2012**, *24*, 382202.

[27] E.-W. Scheidt, V. R. Hathwar, D. Schmitz, A. Dunbar, W. Scherer, F. Mayr, V. Tsurkan, J. Deisenhofer, A. Loidl, *Eur. Phys. J. B* **2012**, *85*, 279.

[28] T. Hatakeda, T. Noji, T. Kawamata, M. Kato, Y. Koike, *J. Phys. Soc. Jpn.* **2013**, *82*, 123705.

[29] S. Hosono, T. Noji, T. Hatakeda, T. Kawamata, M. Kato, Y. Koike, *J. Phys. Soc. Jpn.* **2014**, *83*, 113704.

[30] Z. Guo, L. Zhou, S. Jin, B. Han, F. Sun, W. Yuan, *RSC Adv.* **2017**, *7*, 17539–17544.

[31] H. S. Xu, X. X. Wang, Z. Gao, H. L. Huang, Y. Z. Long, Y. L. Lu, K. B. Tang, *J. Alloys Compd.* **2018**, *735*, 2053–2057.

[32] Y. Xiaofan, H. Tong, T. Tomoya, L. Huan, W. Yanan, G. Hidenori, E. Ritsuko, M. Takafumi, H. Yamaoka, I. Hirofumi, L. Yen-Fa, K. Yoshihiro, *New J. Phys.* **2019**, *21*, 113010.

[33] L. Zhao, D. Wang, Q. Huang, H. Wu, R. Sun, X. Fan, Y. Song, S. Jin, X. Chen, *Phys. Rev. B* **2019**, *99*, 094503.

[34] R.-J. Sun, S.-F. Jin, J. Deng, M.-N. Hao, L.-L. Zhao, X. Fan, X.-N. Sun, J.-G. Guo, L. Gu, *Chinese Phys. B* **2019**, *28*, 067401.

[35] T. Terashima, N. Kikugawa, A. Kiswandhi, D. Graf, E.-S. Choi, J. S. Brooks, S. Kasahara, T. Watashige, Y. Matsuda, T. Shibauchi, T. Wolf, A. E. Böhmer, F. Hardy, C. Meingast, H. v. Löhneysen, S. Uji, *Phys. Rev. B* **2016**, *93*, 094505.

[36] J. P. Sun, G. Z. Ye, P. Shahi, J. Q. Yan, K. Matsuura, H. Kontani, G. M. Zhang, Q. Zhou, B. C. Sales, T. Shibauchi, Y. Uwatoko, D. J. Singh, J. G. Cheng, *Phys. Rev. Lett.* **2017**, *118*, 147004.

[37] P. Massat, Y. Quan, R. Grasset, M.-A. Méasson, M. Cazayous, A. Sacuto, S. Karlsson, P. Strobel, P. Toulemonde, Z. Yin, Y. Gallais, *Phys. Rev. Lett.* **2018**, *121*, 077001.

[38] A. Zhang, T.-l. Xia, K. Liu, W. Tong, Z. Yang, Q. Zhang, *Sci. Rep.* **2013**, *3*, 1216.

[39] X. F. Lu, N. Z. Wang, G. H. Zhang, X. G. Luo, Z. M. Ma, B. Lei, F. Q. Huang, X. H. Chen, *Phys. Rev. B* **2014**, *89*, 020507(R).

[40] X. F. Lu, N. Z. Wang, H. Wu, Y. P. Wu, D. Zhao, X. Z. Zeng, X. G. Luo, T. Wu, W. Bao, G. H. Zhang, F. Q. Huang, Q. Z. Huang, X. H. Chen, *Nat. Mater.* **2014**, *14*, 325–329.

[41] U. Pachmayr, F. Nitsche, H. Luetkens, S. Kamusella, F. Brückner, R. Sarkar, H.-H. Klauss, D. Johrendt, *Angew. Chem. Int. Ed.* **2015**, *54*, 293–297.

[42] L. Ma, B. Lei, N. Wang, K. Yang, D. Liu, F. Meng, C. Shang, Z. Sun, J. Cui, C. Zhu, T. Wu, Z. Sun, L. Zou, X. Chen, *Sci. Bul.* **2019**, *64*, 653–658.

[43] H. Dachs, *Z. Kristallogr.* **1959**, *112*, 60–67.

[44] D. N. Woodruff, F. Schild, C. V. Topping, S. J. Cassidy, J. N. Blandy, S. J. Blundell, A. L. Thompson, S. J. Clarke, *Inorg. Chem.* **2016**, *55*, 9886–9891.

[45] H. Sun, D. N. Woodruff, S. J. Cassidy, G. M. Allcroft, S. J. Sedlmaier, A. L. Thompson, P. A. Bingham, S. D. Forder, S. Cartenet, N. Mary, S. Ramos, F. R. Foronda, B. H. Williams, X. Li, S. J. Blundell, S. J. Clarke, *Inorg. Chem.* **2015**, *54*, 1958–1964.

[46] C. V. Topping, F. K. K. Kirschner, S. J. Blundell, P. J. Baker, D. N. Woodruff, F. Schild, H. Sun, S. J. Clarke, *Phys. Rev. B* **2017**, *95*, 134419.

[47] X. H. Niu, R. Peng, H. C. Xu, Y. J. Yan, J. Jiang, D. F. Xu, T. L. Yu, Q. Song, Z. C. Huang, Y. X. Wang, B. P. Xie, X. F. Lu, N. Z. Wang, X. H. Chen, Z. Sun, D. L. Feng, *Phys. Rev. B* **2015**, *92*, 060504(R).

[48] R. Khasanov, H. Zhou, A. Amato, Z. Guguchia, E. Morenzoni, X. Dong, G. Zhang, Z. Zhao, *Phys. Rev. B* **2016**, *93*, 224512.

[49] Y. P. Wu, D. Zhao, X. R. Lian, X. F. Lu, N. Z. Wang, X. G. Luo, X. H. Chen, T. Wu, *Phys. Rev. B* **2015**, *91*, 125107.

[50] W. Chen, C. Zeng, E. Kaxiras, Z. Zhang, *Phys. Rev. B* **2016**, *93*, 064517.

[51] D.-Y. Liu, Z. Sun, L.-J. Zou, *New J. Phys.* **2017**, *19*, 023028.

[52] X. Dong, H. Zhou, H. Yang, J. Yuan, K. Jin, F. Zhou, D. Yuan, L. Wei, J. Li, X. Wang, G. Zhang, Z. Zhao, *J. Am. Chem. Soc.* **2015**, *137*, 66–69.

[53] X. Yi, L. Qin, X. Xing, B. Lin, M. Li, Y. Meng, M. Xu, Z. Shi, *J. Phys. Chem. Solids* **2019**, *137*, 109207.

[54] Y. Mao, J. Li, Y. Huan, J. Yuan, Z. Li, K. Chai, M. Ma, S. Ni, J. Tian, S. Liu, H. Zhou, F. Zhou, J. Li, G. Zhang, K. Jin, X. Dong, Z. Zhao, *Chin. Phys. Lett.* **2018**, *35*, 057402.

[55] X. Zhou, C. K. H. Borg, J. W. Lynn, S. R. Saha, J. Paglione, E. E. Rodriguez, *J. Mater. Chem. C* **2016**, *4*, 3934–3941.

[56] G. Yu, G. Y. Zhang, G. H. Ryu, C. T. Lin, *J. Phys. Condens. Matter* **2016**, *28*, 015701.

[57] G.-Y. Zhang, M. M.-C. Chou, C.-T. Lin, *Crystals* **2017**, *7*, 1–26.

[58] G. B. Hu, N. Z. Wang, M. Z. Shi, F. B. Meng, C. Shang, L. K. Ma, X. G. Luo, X. H. Chen, *Phys. Rev. Mater.* **2019**, *3*, 064802.

[59] A. Coelho, *TOPAS-Academic*, Version 4.1, Coelho Software, Brisbane, Australia, **2007**.

[60] *ESVision Vol. 4.0.164*, Emispec Systems Inc., Quebec, Canada, **2002**.

[61] X. Dong, K. Jin, D. Yuan, H. Zhou, J. Yuan, Y. Huang, W. Hua, J. Sun, P. Zheng, W. Hu, Y. Mao, M. Ma, G. Zhang, F. Zhou, Z. Zhao, *Phys. Rev. B* **2015**, *92*, 064515.

[62] K. T. Lai, I. Antonyshyn, Y. Prots, M. Valldor, *J. Am. Chem. Soc.* **2017**, *139*, 9645–9649.

[63] T. Hirone, S. Maeda, N. Tsuya, *J. Phys. Soc. Jpn.* **1954**, *9*, 496–499.

[64] T. Hirone, S. Chiba, *J. Phys. Soc. Jpn.* **1956**, *11*, 666–670.

[65] H. Okamoto, *J. Phase Equilib.* **1991**, *12*, 383–389.

[66] J. E. Dutrizac, M. B. I. Janjua, J. M. Toguri, *Can. J. Chem.* **1968**, *46*, 1171–1174.

[67] P. Terzieff, K. L. Komarek, *Monatsh. Chem.* **1978**, *109*, 651–659.

[68] V. Thampy, J. Kang, J. A. Rodriguez-Rivera, W. Bao, A. T. Savici, J. Hu, T. J. Liu, B. Qian, D. Fobes, Z. Q. Mao, C. B. Fu, W. C. Chen, Q. Ye, R. W. Erwin, T. R. Gentile, Z. Tesanovic, C. Broholm, *Phys. Rev. Lett.* **2012**, *108*, 107002.

[69] L. Liu, X. Bie, H. Ehrenberg, C. Wang, Y. Wei, G. Chen, F. Du, *J. Appl. Phys.* **2011**, *110*, 093912.

[70] H. Lin, R. Kang, L. Kong, X. Zhu, H.-H. Wen, *Sci. China Phys. Mech. Astron.* **2016**, *60*, 027411.

[71] B. Lei, Z. J. Xiang, X. F. Lu, N. Z. Wang, J. R. Chang, C. Shang, A. M. Zhang, Q. M. Zhang, X. G. Luo, T. Wu, Z. Sun, X. H. Chen, *Phys. Rev. B* **2016**, *93*, 060501(R).

[72] S. J. Sedlmaier, S. J. Cassidy, R. G. Morris, M. Drakopoulos, C. Reinhard, S. J. Moorhouse, D. O'Hare, P. Manuel, D. Khalyavin, S. J. Clarke, *J. Am. Chem. Soc.* **2014**, *136*, 630–633.

# 4. Magnetic and electronic properties of $CaFeO_2Cl$

Bettina Rendenbach, Steffen Klenner, Rainer Pöttgen and Dirk Johrendt

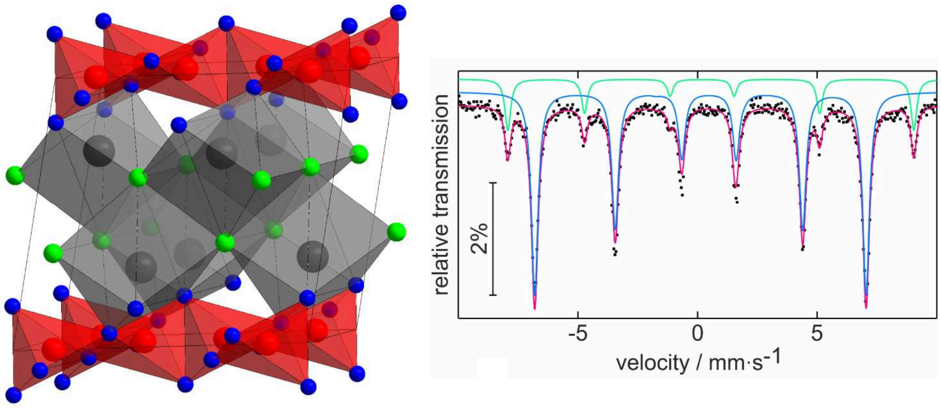

published in: *Zeitschrift für Naturforschung B* **2020**, *75*, 105–110.

Reprinted with permission from De Gruyter.

## Abstract

$CaFeO_2Cl$ is a unique exception in the family of the iron oxyhalides. Its crystal structure is not related to the Ruddlesden-Popper phases as known for the other members, but contains layers of edge-sharing $FeO_{2/2}O_{3/3}$ pyramids without Fe–Cl contacts. The iron atoms form a distorted honeycomb lattice. Magnetization measurements on single crystals show an unexpected weak anisotropy and indicate antiferromagnetic ordering of the iron moments already at room temperature. $^{57}$Fe Mössbauer spectra confirm the trivalent oxidation state of iron and the presence of magnetic order. DFT calculations using the LDA+$U$ approach support a Mott-insulating antiferromagnetic ground state and indicate a Néel-type ordered antiferromagnetic state in the honeycomb-layer. The band gap from optical measurements is 1.3 eV and agrees with the red-brown colour as well as with the theoretical calculations.

## Introduction

The search for new layered materials developed various mixed anion compounds,[1-2] such as oxide carbonates[3], oxide borates[4] and oxide halides[5-6]. Especially layered oxyhalides represent a promising field for studies of new materials with various properties,[7] such as superconductors[8], frustrated magnets[9], or possible two-dimensional magnetism challenging the Mermin-Wagner theorem[10]. The research also led to an awaking interest in the oxyhalides as high $T_C$-multiferroics[11], and especially in high-$T_c$ materials, resulting in several copper oxide halide superconductors.[12-15]

Iron oxyhalides with alkaline-earth cations have been reported with different structure types, among them $A_2FeO_3X$ ($A$ = Ca, Sr, $X$ = F, Cl, Br) or $Sr_3Fe_2O_5Cl_2$. These derivatives of the tetragonal $K_2NiF_4$-type or Ruddlesden-Popper phases[16-17] contain layers or double layers of $Fe(O,X)_6$ octahedra with the halides $X$ at the apical positions. Neutron scattering experiments revealed antiferromagnetic ordering with magnetic moments oriented parallel to the layers, e.g. G-type antiferromagnetism in $Sr_3Fe_2O_5Cl_2$.[18] Belonging to this class of layered transition metal halides, monoclinic $CaFeO_2Cl$[19-20] is exceptional because the structure contains no octahedra but consists of layers of edge-sharing $FeO_{2/2}O_{3/3}$ square pyramids separated by CaCl-sheets; no Fe–Cl contacts occur (Figure 4-1). The iron atoms form a distorted honeycomb-lattice on the *ab*-plane.

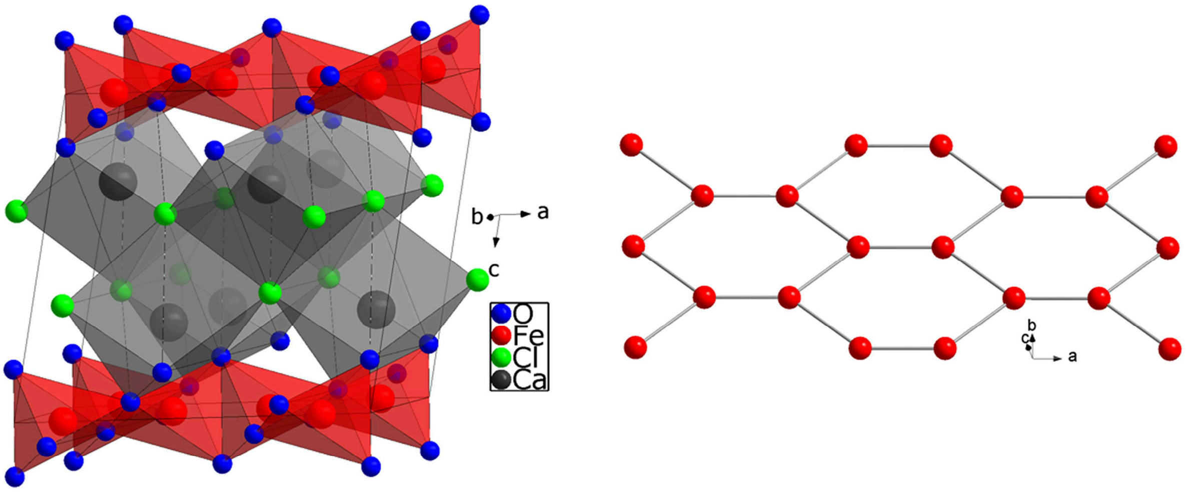

**Figure 4-1.** Crystal structure of monoclinic $CaFeO_2Cl$. The layers of $FeO_{2/2}O_{3/3}$ square pyramids (red polyhedra) are emphasized and distorted honeycomb lattice of the iron atoms.

In spite of the exceptional crystal structure, the physical properties of $CaFeO_2Cl$ are currently unknown. We have optimized the synthesis procedure given in the literature[19] and achieved samples with purities above 90 %. In this paper, we report results of magnetic and optical measurements, along with quantum chemical calculations. We show that $CaFeO_2Cl$ is an antiferromagnetic Mott insulator and propose a probable magnetic ordering pattern.

## Experimental

$CaFeO_2Cl$ was synthesized by a modified procedure of the protocol reported one by J. Ackermann[19]. The starting materials $Fe_2O_3$ (ALFA AESAR, 99.99 %,) and $CaCl_2$ (ABCR, 99.99 %,) were mixed in a ratio 1:100 and ground in an agate mortar in air. The samples were prepared in alumina crucibles under air by heating to 850 °C for 12 h, then cooled to 350 °C for 5 h, and finally cooled to room temperature (step 1). After grounding the samples obtained in step one, the procedure from step one was repeated with a slower cooling rate of 20 K/h (step 2). Washing the product several times with distilled water removed all excess $CaCl_2$. The resulting samples were dried under vacuum and stored under argon. This approach yielded a polycrystalline red-brown powder with brown plate-like single-crystals. The samples contained the desired product $CaFeO_2Cl$ and $Fe_2O_3$. Through this optimized synthesis, yields up to 92 % were achieved. The powder X-Ray patterns were obtained with a Stoe Stadi-P diffractometer (Mo-$K_{\alpha1}$) equipped with a Stoe Mythen 1k detector. Rietveld refinement were done with TOPAS.[21] Single-crystal diffraction data were recorded with a Stoe IPDS-I diffractometer at room temperature using Mo-$K_{\alpha1}$ radiation ($\lambda = 0.71069$ Å). Reflection intensity integration, data reductions, and multi-scan absorption corrections were done with APEX2[22] and SADABS[23]. The structure was solved with JANA2006[24] and refined with SHELXL crystallographic software package[25]. CCDC 1957141 contains the supplementary crystallographic data for this paper. These data can be obtained free of charge from The Cambridge Crystallographic Data Centre via www.ccdc.cam.ac.uk/data_request/cif. Magnetic measurements with $CaFeO_2Cl$ single crystals were carried out with a vibrating sample magnetometer (VSM) option in a Quantum Design Physical-Property-Measurement-System (PPMS-9). Crystals were selected manually from the samples, aligned parallel to the *ab* crystal plane of $CaFeO_2Cl$ in a parquet-like pattern and glued with low temperature varnish. Magnetization measurements were carried out with the ab crystal plane parallel and perpendicular to the magnetic field. Electronic structure calculations were performed using the Vienna ab initio simulation package (VASP)[26-27] which is based on density functional theory (DFT) and plane wave basis sets. Projector-augmented waves (PAW)[28] were used and contributions of correlation and exchange were treated in the generalized-gradient approximation (GGA)[29]. The strongly correlated iron 3*d*-states were corrected using the LDA+*U* method in the rotationally invariant approach by Dudarev *et al.*[30]. Diffuse reflectance spectra were measured with powder samples on a UV/Vis Jasco V-650 spectrophotometer (200–800 nm). The spectra were converted to absorption spectra based on the Kubelka-Munk[31] theory to determine the optical bandgap. A $^{57}$Co source in an Rh matrix was used for the $^{57}$Fe Mössbauer spectroscopic investigation of $CaFeO_2Cl$. The measurement was performed in a continuous flow cryostat system (Janis Research Co LLC). The usual transmission geometry was used. The source was kept at room temperature while the sample was cooled to $T = 6$ K. The optimal absorber thickness was calculated according to the work of Long *et al* [32] The sample was placed in a thin-walled PMMA container and diluted with potassium chloride for a complete distribution of the sample within the container volume. Fitting of the experimental data was performed with the WINNORMOS for IGOR6 program package.[33]

### Results and discussion

$CaFeO_2Cl$ was synthesized in a $CaCl_2$-flux in an open system from $Fe_2O_3$ as a red-brown, moisture and air stable product. Single-crystal X-Ray diffraction confirmed the structure in the monoclinic centrosymmetric space group *C*2/*m* (No. 12) with the lattice parameters $a = 9.969(2)$ Å, $b = 3.811(8)$ Å, $c = 8.735(17)$ Å and $\beta = 103.62(3)°$. The single-crystal X-Ray data was used to refine the powder X-Ray pattern (Figure 4-2). The Rietveld-fit yielded $CaFeO_2Cl$ as the main component (ca. 92 wt. %) with $Fe_2O_3$ as impurity.

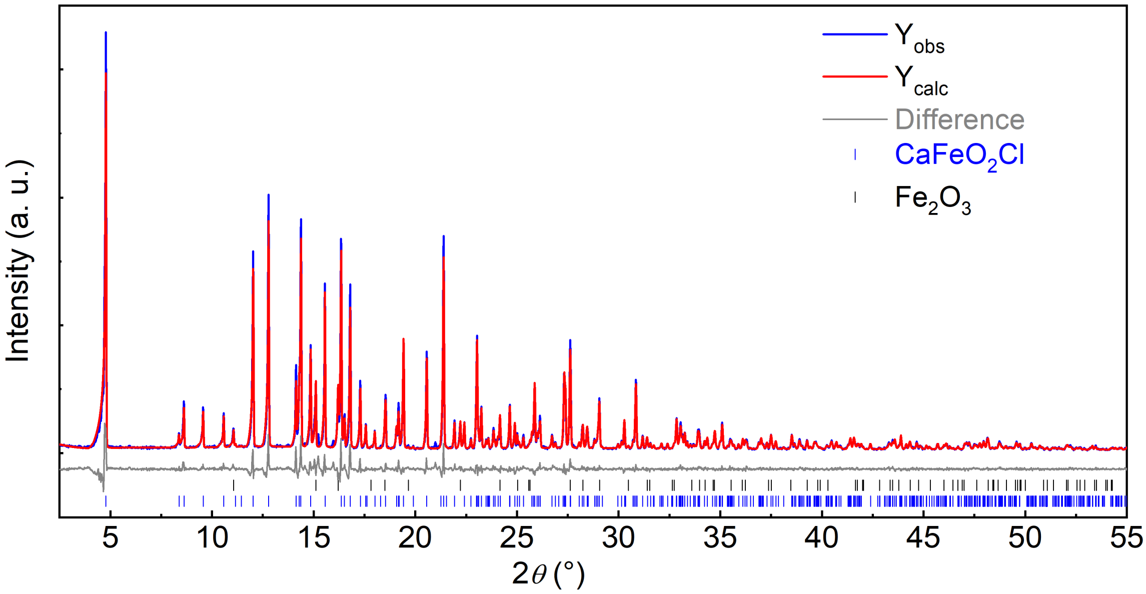

**Figure 4-2**. Powder X-Ray pattern of $CaFeO_2Cl$ (Mo-$K_{\alpha1}$) sample (blue line) with Rietveld-fit (red line) and difference (grey line).

Figure 4-1 shows the crystal structure of $CaFeO_2Cl$. Layers of edge-sharing $FeO_{2/2}O_{3/3}$ polyhedra alternate with regions of CaCl. The $FeO_5$-pyramid is slightly distorted with four different Fe-O distances ranging from 1.89 to 2.00 Å. The Addison $\tau$-parameter ($\tau = (\beta\text{-}\alpha)/60$; $\alpha$, $\beta$ = largest bond angles)[34] of

0.1 confirms the square pyramidal coordination. Calcium has three oxygen and four chlorine neighbours. The iron sublattice is a planar but slightly elongated honeycomb-net with Fe-Fe distances of 2.743 and 2.959 Å.

## Optical properties

Figure 4-3 shows results of the optical reflection measurements of the $CaFeO_2Cl$ powder ($\lambda$ = 500–800 nm). Because weak signals in absorbance spectra are enhanced in reflected spectra, reflectance spectra in absorbance units cannot be compared directly. Analysing reflection spectra using the Kubelka-Munk function makes them similar to absorbance spectra and allows the determination of the bandgap energy $E_g$.[31]

$$F(R_\infty) = \frac{(1-R_\infty)^2}{2R_\infty} = \frac{K(\lambda)}{s(\lambda)} \propto \alpha = \frac{\left(h\nu - E_g\right)^2}{h\nu}$$

$R_\infty$ is the diffuse reflectance of an infinitely thick sample, K($\lambda$) is the absorption coefficient and s($\lambda$) is the scattering coefficient.

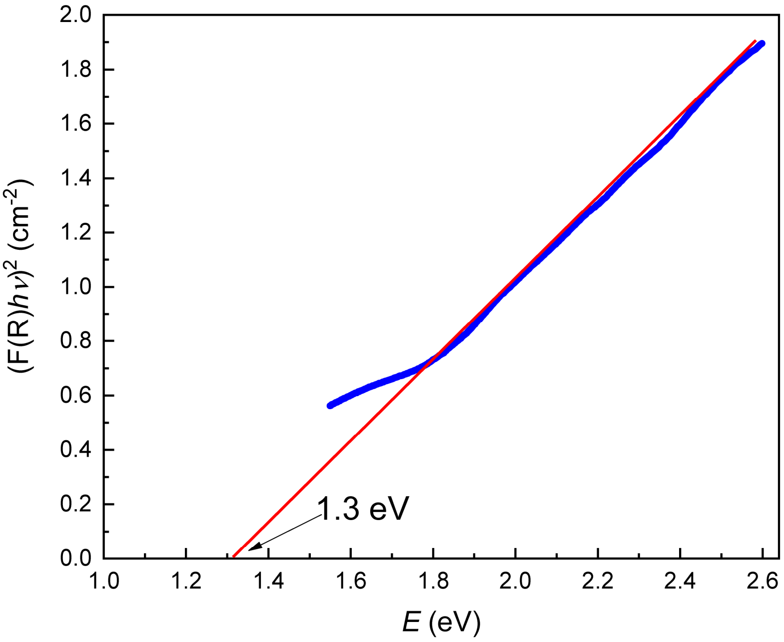

**Figure 4-3**. Bandgap calculation using the Kubleka-Munk function.

The direct bandgap is determined by the extrapolation from the linear portion of the plot of $[F(R_\infty)h\nu]^2$ against hν (Tauc plot for direct bandgap). The estimated bandgap is 1.3 eV (Figure 4-3), which is consistent with the red-brown colour of $CaFeO_2Cl$.

## Magnetism

Selected plate-like single crystals of $CaFeO_2Cl$ were arranged parallel on the sample holder in order to measure the magnetization in fields applied either perpendicular (⊥) or parallel (//) to the layers. Note that the crystals were not aligned along the directions perpendicular to the layers. Figure 4-4 shows magnetization isotherms at temperatures between 5 K and 305 K.

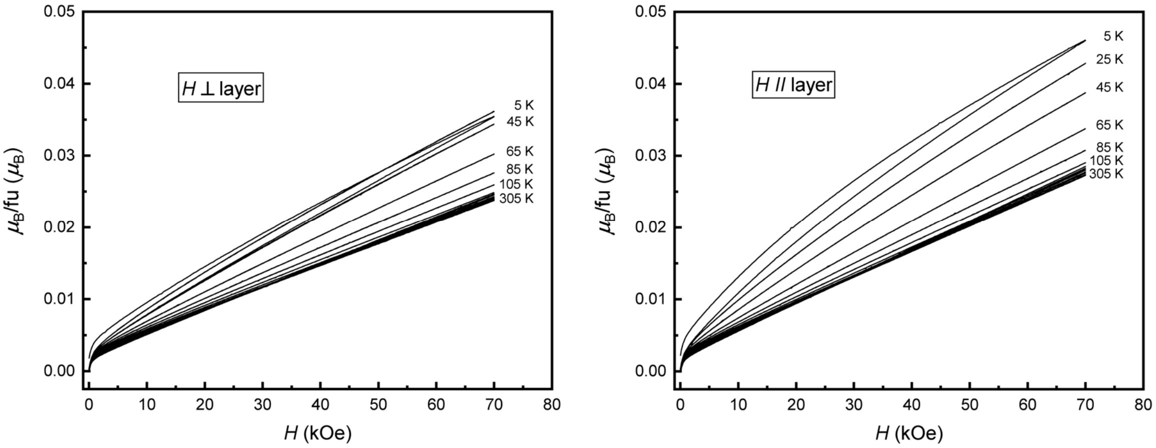

**Figure 4-4**. Magnetization isotherms of $CaFeO_2Cl$ between 5 and 305 K with fields aligned perpendicular (left) and parallel to the $FeO_2$ layers (right).

The magnetization increases linearly with the field but remains below 0.05 $\mu_B$ per formula unit $CaFeO_2Cl$, which indicates that the magnetic moments of the $Fe^{3+}$ ions ($S = 5/2$) are antiferromagnetically ordered in the considered temperature range (5–300 K). The magnetization increases at lower temperatures, which is contrary to the expected either constant values if the field is perpendicular or decrease if it is parallel to the magnetization direction (easy axis) of an antiferromagnet[35]. Given that the magnetization remains very small even at low temperatures, the increase may be the result of traces of paramagnetic impurities. The anisotropy of the magnetization is relatively small with respect to the layered crystal structure. Assuming that the paramagnetic contributions (from impurities) are isotropic, we find that the magnetization at $T = 5$ K is about 25 % higher if the field is parallel to the $FeO_{2/2}O_{3/3}$ layers. This indicates that the alignment of the magnetic moments, or easy axis, should be perpendicular to the layers.

### Mössbauer spectroscopy

The $^{57}$Fe spectrum of polycrystalline $CaFeO_2Cl$ at $T = 6$ K is shown in Figure 4-5. The corresponding fitting parameters for the most reliable fit are listed in Table 4-1.

**Table 4-1.** Fitting parameters of the 6 K $^{57}$Fe Mössbauer spectroscopic measurements of $CaFeO_2Cl$. $\delta$ = isomer shift, $\Delta E_Q$ = quadrupole splitting, $\Gamma$ = experimental line width, $B_{hf}$ = magnetic hyperfine field, $\theta$ = tensor between the principle axis of the electrical field gradient and the direction of the magnetic hyperfine field.

| | $\delta$/ mm·s$^{-1}$ | $\Delta E_Q$/mm·s$^{-1}$ | $\Gamma$/mm·s$^{-1}$ | $B_{hf}$/T | $\theta$/° | area/% |
|---|---|---|---|---|---|---|
| $CaFeO_2Cl$ | 0.30(1) | -0.97(1) | 0.337(3) | 42.6(1) | 39.9(2) | 82(1) |
| $Fe_2O_3$ | 0.37(1) | 0.37(1) | 0.287(12) | 52.6(1) | - | 18(1) |

Figure 4-5 shows two different fitting approaches. Two overlapping sextet signals are visible in the recorded spectrum. The less intense one corresponds to the by-product $Fe_2O_3$ and the other one to $CaFeO_2Cl$. The top spectrum of Figure 4-5 shows a fit with two regular sextets, the bottom one a fitting with a full Hamiltonian.

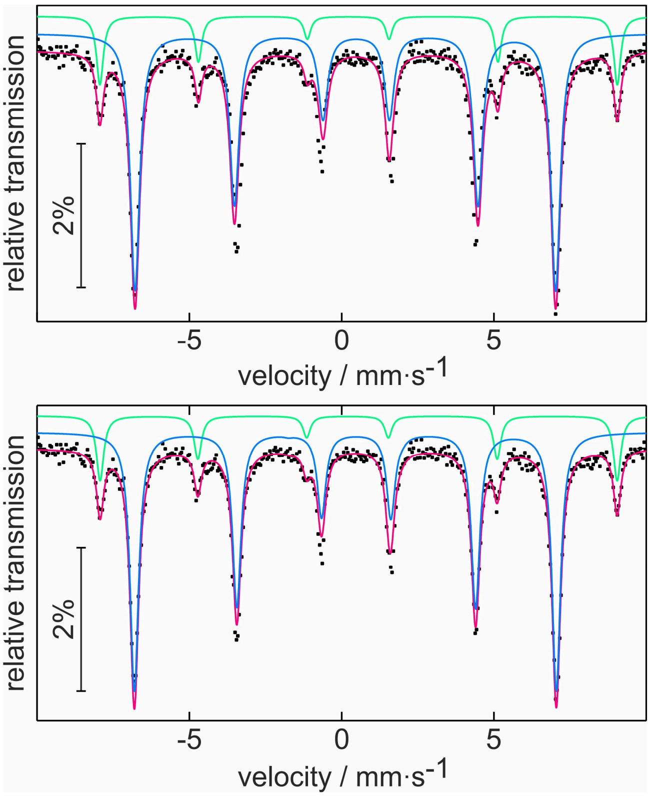

**Figure 4-5.** Experimental (black dots) and simulated (coloured lines) $^{57}$Fe Mössbauer spectra of $CaFeO_2Cl$ at 6 K. Top: $CaFeO_2Cl$ signal fitted with a sextet model; bottom: $CaFeO_2Cl$ fitted with a complete Hamiltonian.

No impurity phases other than $Fe_2O_3$ can be observed in the experimental spectrum, in accordance with the PXRD data. It is clearly apparent that the fit for the top spectrum is slightly off-centred from the normal sextet splitting. The full Hamiltonian fit with the inclusion of the parameter $\theta$, which describes the angle between the direction of the magnetic hyperfine field and the tensor of the electrical field gradient, gives a more satisfactory fitting. Similar results have recently been reported for the brownmillerite phase $Sr_2Fe_2O_5$.[36] The obtained isomer shift of 0.30 mm $s^{-1}$ indicates iron in the oxidation state +3 as can be expected from the empirical formula. This is in agreement with a large summary of $^{57}$Fe data of iron oxides compiled by Menil[37]. The square pyramidal coordination of Fe(III) is rare; however, our $^{57}$Fe Mössbauer spectroscopic data is in good agreement with the series of iron substituted chromates $RETiCr_{1-x}Fe_xO_5$.[38] The slightly negative quadrupole splitting of –0.97 mm $s^{-1}$ results from the asymmetric coordination environment of the iron site (distorted square pyramid). Full magnetic hyperfine field splitting is observed with a field of 42.6 T. The parameter $\theta$ mentioned above leads to the conclusion that the magnetic moments are aligned along a preferred crystallographic direction.

### DFT calculations

The electronic band structure was calculated using the VASP package. Due to the actually unknown magnetic structure, the total energies of different trial magnetic ordering patterns were compared in order to identify a probable magnetic state. The primitive unit cell of $CaFeO_2Cl$ contains four iron positions. The trial magnetic structures were either ferromagnetic (FM ↑↑↑↑), or antiferromagnetic (AF1 ↑↓↑↓; AF2 ↑↓↓↑; AF3 ↑↑↓↓). The calculations reveal that AF1 is the most stable configuration, followed by AF2 (+0.1 eV), AF3 (+0.36 eV) and FM (+0.4 eV). AF1 correspond to a Néel-type magnetic structure where all moments of the iron atoms within the honeycomb-layer are alternating spin up and down as shown in Figure 4-6.

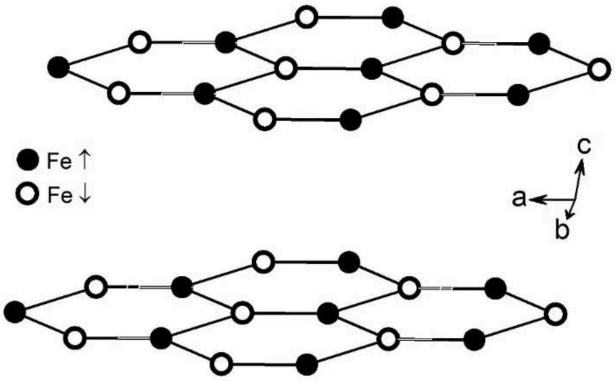

**Figure 4-6.** Most stable trial AF magnetic structure in the honeycomb Fe-layer of $CaFeO_2Cl$. Filled and open circles mark spin up and down, respectively.

The spin polarized band structure shown in Figure 4-7 was calculated using this model of the antiferromagnetic ordering and the LDA+$U$ approach with a $U_{eff}$ (= $U$–$J$; $J$ = 0) of 4 eV in order to account for the strongly correlated Fe-3$d$ states.

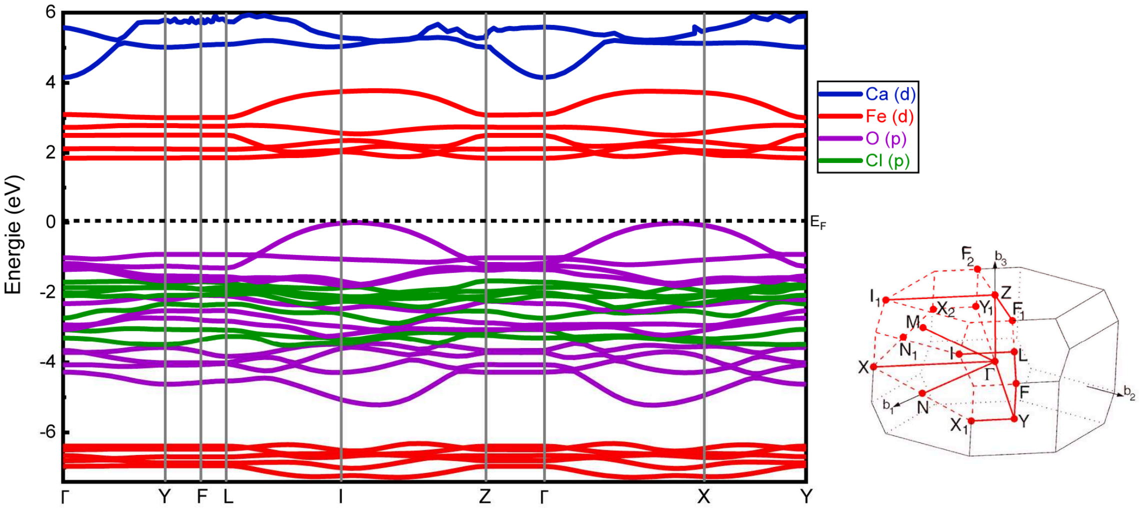

**Figure 4-7.** Spin polarized LDA+$U$ band structure of the antiferromagnetic $CaFeO_2Cl$.

The calculated band gap $E_g$ occurs between the O-2$p$ valence- and Fe-3$d$ conduction bands. $E_g$ correlates linearly with the effective $U$ parameter and results in 1.96 eV for $U$ = 4 eV and 1.59 eV for $U$ = 3 eV. The calculated ordered magnetic moment of 4.2–4.3 $\mu_B$/Fe is smaller than the expected 5 $\mu_B$/Fe for the $S$ = 5/2 state. This may have its origin in the special magnetic properties of the honeycomb-lattice with only three neighbours. It has been shown that the magnetization in a threefold connected $S$ = ½ system is reduced by a factor of 0.87 compared to the square lattice[39]. A reduced ordered magnetic moment of 2.3 $\mu_B$ has also been found in the $S = 3/2$ antiferromagnetic honeycomb-lattice of $Li_2MnO_3$.[40]

## Conclusion

$CaFeO_2Cl$ was obtained in an open system synthesis from $Fe_2O_3$ in a $CaCl_2$-flux. The single-crystal X-Ray and powder data confirm the layered crystal structure with fivefold coordinated iron described earlier. Magnetic measurements with oriented single crystals indicate that the magnetic moments at the iron atoms are antiferromagnetically ordered at room temperature and suggest that the magnetic easy axis is perpendicular to the layers. $^{57}$Fe Mössbauer spectra confirm the 3+ state of iron and the magnetic ordering showing full magnetic hyperfine splitting with a field of 42.6 T at 6 K. $CaFeO_2Cl$ is a Mott insulator with an optical band gap of ~1.3 eV. DFT electronic band structure calculations using the LDA+$U$ approach confirm the measured properties and suggest that the magnetic ordering pattern is Néel-type within a honeycomb-like layer of iron atoms.

## References

[1] M. T. Weller, C. S. Knee, *J. Mater. Chem.* **2001**, *11*, 701–712.

[2] G. M. Veith, M. Greenblatt, M. Croft, J. B. Goodenough, *Mater. Res. Bull.* **2001**, *36*, 1521–1530.

[3] K. Yamaura, Q. Huang, J. W. Lynn, R. W. Erwin, R. J. Cava, *J. Solid State Chem.* **2000**, *152*, 374–380.

[4] D. Pelloquin, M. Hervieu, C. Michel, N. Nguyen, B. Raveau, *J. Solid State Chem.* **1997**, *134*, 395–408.

[5] W. Leib, H. Müller-Buschbaum, *Z. Anorg. Allg. Chem.* **1984**, *518*, 115–119.

[6] J. Huang, R. D. Hoffmann, A. W. Sleight, *Mater. Res. Bull.* **1990**, *25*, 1085–1090.

[7] M. Al-Mamouri, P. P. Edwards, C. Greaves, M. Slaski, *Nature* **1994**, *369*, 382–384.

[8] S. Adachi, T. Tatsuki, T. Tamura, K. Tanabe, *Chem. Mater.* **1998**, *10*, 2860–2869.

[9] A. A. Tsirlin, H. Rosner, *Phys. Rev. B* **2009**, *79*, 214416.

[10] N. D. Mermin, H. Wagner, *Phys. Rev. Lett.* **1966**, *17*, 1133–1136.

[11] L. Zhao, M. T. Fernández-Díaz, L. H. Tjeng, A. C. Komarek, *Sci. Adv.* **2016**, *2*, e1600353.

[12] S. M. Loureiro, C. Felser, Q. Huang, R. J. Cava, *Chem. Mater.* **2000**, *12*, 3181–3185.

[13] N. D. Zhigadlo, J. Karpinski, S. Weyeneth, R. Khasanov, S. Katrych, P. Wägli, H. Keller, *J. Phys. Conf. Ser.* **2008**, *97*, 012121.

[14] X. J. Wu, C. Q. Jin, P. Laffez, T. Tatsuki, T. Tamura, S. Adachi, H. Yamauchi, N. Koshizuka, *Physica C Supercond.* **1996**, *258*, 143–152.

[15] Q. Q. Liu, X. M. Qin, Y. Yu, F. Y. Li, C. Dong, C. Q. Jin, *Physica C Supercond.* **2005**, *420*, 23–29.

[16] S. N. Ruddlesden, P. Popper, *Acta Crystallogr.* **1957**, *10*, 538–539.

[17] S. N. Ruddlesden, P. Popper, *Acta Crystallogr.* **1958**, *11*, 54–55.

[18] C. S. Knee, M. A. L. Field, M. T. Weller, *Solid State Sci.* **2004**, *6*, 443–450.

[19] J. F. Ackerman, *J. Solid State Chem.* **1991**, *92*, 496–513.

[20] E. Parthé, S. Hu, *J. Solid State Chem.* **2003**, *174*, 165–166.

[21] A. Coelho, *TOPAS-Academic*, Version 4.1, Coelho Software, Brisbane, Australia, **2007**.

[22] *APEX2* (Version 2012.12–0) ed., Bruker AXS Inc., Madison, WI, USA, **2007**.

[23] G. M. Sheldrick, *SADABS (Version 2012/1)*, Bruker AXS Inc., Madison, WI, USA, **2001**.

[24] V. Petricek, M. Dusek, L. Palatinus, *Jana2006 (Version 26/09/2012)*, Institute of Physics, Praha, Czech Republic, **2006**.

[25] G. Sheldrick, *Acta Crystallogr. Sec. A* **2008**, *64*, 112–122.

[26] G. Kresse, J. Furthmüller, *Comput. Mater. Sci.* **1996**, *6*, 15–50.

[27] G. Kresse, D. Joubert, *Phys. Rev. B* **1999**, *59*, 1758–1775.

[28] P. E. Blöchl, *Phys. Rev. B* **1994**, *50*, 17953–17979.

[29] J. P. Perdew, K. Burke, M. Ernzerhof, *Phys. Rev. Lett.* **1996**, *77*, 3865–3868.

[30] S. L. Dudarev, G. A. Botton, S. Y. Savrasov, C. J. Humphreys, A. P. Sutton, *Phys. Rev. B* **1998**, *57*, 1505–1509

[31] P. Kubelka, F. Munk, *Z. Tech. Phys.* **1931**, *12*, 593–601.

[32] G. J. Long, T. E. Cranshaw, G. Longworth, *Moessbauer Eff. Ref. Data J.* **1983** 6, 42.

[33] R. A. Brand, *WINNORMOS for IGOR6 (version for IGOR 6.2 or above: 22/02/2017)*, Universität Duisburg, Duisburg (Germany) **2017**.

[34] A. W. Addison, T. N. Rao, J. Reedijk, J. van Rijn, G. C. Verschoor, *J. Chem. Soc. Dalton Trans.* **1984**, 1349–1356.

[35] T. Nagamiya, K. Yosida, R. Kubo, *Adv. Phys.* **1955**, *4*, 1–112.

[36] J. C. Waerenborgh, E. V. Tsipis, J. E. Auckett, C. D. Ling, V. V. Kharton, *J. Solid State Chem.* **2013**, *205*, 5–9.

[37] F. Menil, *J. Phys. Chem. Solids* **1985**, *46*, 763–789.

[38] P. J. Schurer, A. H. Morrish, *Phys. Rev. B* **1977**, *16*, 951–959.

[39] R. F. Bishop, P. H. Y. Li, O. Götze, J. Richter, C. E. Campbell, *Phys. Rev. B* **2015**, *92*, 224434.

[40] S. Lee, S. Choi, J. Kim, H. Sim, C. Won, S. Lee, S. A. Kim, N. Hur, J.-G. Park, *J. Phys. Condens. Matter* **2012**, *24*, 456004.

# 5. Summary

The emphasis of this thesis is on the synthesis of layered iron chalcogenides and iron oxyhalides. It includes electrochemical intercalation, low temperature solid-state synthesis, and flux-mediated solid-state synthesis. The first part concentrates on the electrochemical intercalation approach for the synthesis of layered iron-chalcogenide superconductors. Constructional and experimental work for the setup, optimization and scalability of the electrolysis were successfully implemented. The insights into the critical parameters were acquired and for the first time a phase pure bulk superconductor $(TMA)_{0.5}Fe_2Se_2$ ($T_c$ = 43 K) was synthesized by electrochemical synthesis. The next part consists of a detailed analysis of the compound concerning its structural, magnetic and electronic properties. Further iron chalcogenide compounds, [(Li,Fe)OH]FeSe, were discovered by low temperature solid-state synthesis and analysed by means of changes in the crystal structure and physical properties. The last part includes additional studies on the magnetic and electronic properties of the layered iron oxyhalide $CaFeO_2Cl$ and determines the properties of this structurally unique oxyhalide. The compounds synthesized in this thesis were appropriately analysed by a broad range of analytical methods like powder and single crystal XRD, high temperature PXRD, elemental analysis (EDS, CHNS), infrared spectroscopy, UV/Vis spectroscopy, magnetic, resistivity and Mössbauer measurements. DFT calculations supported structure models and magnetic properties. A summary of each chapter is given below.

### Electrolysis – theoretical considerations and experimental procedure

The design and setup of this method is established with a galvanostatic electrolysis apparatus consisting of a tungsten anode and an amalgamated copper spoon connected to a platinum wire as cathode. The apparative and reaction parameters are considered and discussed under theoretical and experimental aspects. The following aspects are addressed: apparative requirements, electrode materials, electrolytes, supporting electrolytes and reaction conditions. Furthermore, an extensive experimental description of the electrolysis and the preparative steps is given. The modification by adding a new electrode port and using a mercury lake proved the scalability of the reaction and a higher amount of desired bulk product has been achieved.

### Electrochemical synthesis and crystal structure of the organic ion intercalated superconductor $(TMA)_{0.5}Fe_2Se_2$ with $T_c$ = 43 K

$(TMA)_{0.5}Fe_2Se_2$ was prepared through electrochemical intercalation of tetramethylammonium ($TMA^+$) ions into *β*-FeSe. The application of the established electrochemical method led to the new phase pure bulk superconductor with a critical temperature as high as 43 K. Powder X-Ray diffraction coupled with DFT calculations revealed a highly credible model of the crystal structure. The layered crystal structure represents a variant of the $ThCr_2Si_2$-type structure, where the $TMA^+$ ions are densely packed between the FeSe layers. The $TMA^+$ ions are disordered over two equivalent positions and in different orientations. The structure is closely related to "122-type" of the iron arsenide family of superconductors. Elemental analysis and infrared spectroscopy measurements confirmed the composition of $(TMA)_{0.5}Fe_2Se_2$. The intercalation of $TMA^+$ ions is topotactic and reversible by heating the compound up to 200 °C. Superconducting tetragonal FeSe is recovered after deintercalation. Magnetic and electrical resistivity measurements determine bulk superconductivity at 43 K. Typical for a hard type-II superconductor the isothermal magnetization measurements depict a "butterfly" pattern.

**Solid-state synthesized $[(Li_{0.88}Fe_{0.12})OH]FeSe$ and $[LiOH](Fe)_zFeSe$**

Two new phases of the [(Li,Fe)OH]FeSe family were prepared by low temperature solid-state synthesis starting from vapour-grown, superconducting *β*-FeSe and excess LiOH. $[(Li_{0.88}Fe_{0.12})OH]FeSe$ was obtained with minor side phases. $[LiOH](Fe)_zFeSe$ only forms with a huge excess of LiOH and faster heating rates. Both phases, $[(Li_{0.88}Fe_{0.12})OH]FeSe$ and $[LiOH](Fe)_zFeSe$, crystalize in the space group *P*4/*mmm* (no. 129) according to powder X-Ray diffraction data. The *c*-axis is strongly elongated in the $[LiOH](Fe)_zFeSe$ phase. This elongation is due to the distortion of the $LiO_{4/4}$ tetrahedra and maybe due to additional iron/lithium at interstitial sites. The higher lithium occupation in the $(Li_{0.88}Fe_{0.121})OH$ layer of $[(Li_{0.88}Fe_{0.12})OH]FeSe$ probably explains the absence of superconductivity due to a lower charge doping of the $FeSe_{4/4}$ layer.

**Magnetic and electronic properties of $CaFeO_2Cl$**

Monoclinic $CaFeO_2Cl$ was prepared with a flux-mediated open system solid-state synthesis from $Fe_2O_3$ in a $CaCl_2$-flux. It crystallizes in the space group $C2/m$ (no. 12) with a layered crystal structure containing layers of edge-sharing $FeO_{2/2}O_{3/3}$ pyramids without Fe–Cl contacts. Iron atoms form a distorted honeycomb lattice. The magnetic moments of the iron atoms are antiferromagnetically ordered at room temperature. Magnetic measurements with oriented single crystals indicated a magnetic easy axis perpendicular to the honeycomb layers. $^{57}$Fe Mössbauer spectroscopy revealed a trivalent oxidation state of the iron and a magnetic ordering with full magnetic hyperfine splitting (42.6 T and 6 K). The compound is a Mott insulator with a band gap of ~1.3 eV determined from the Kubelka-Munk function. Additional DFT calculations using the LDA+$U$ approach determined the measured properties and indicate Néel-type magnetic ordering pattern within the distorted honeycomb layer of iron atoms.

# 6. Conclusion

The main part of the thesis presents a synthesis approach for iron chalcogenide-based superconductors and reveals the potential of the electrochemical method for expanding the accessibility of iron-chalcogenide based superconductors. The electrochemical approach is thoroughly investigated regarding theoretical as well as experimental aspects. The feasibility is demonstrated by the successful synthesis of $(TMA)_{0.5}Fe_2Se_2$ with a critical temperature of 43 K. Furthermore, the synthesis strategy shows fascinating and promising results for a structural diversity and high yield bulk compounds with superconducting properties. The crystal structure insights combined with even higher yields, due to the modification of the electrolysis chamber, might lead to a deeper understanding of the mechanisms in FeSe-based superconductors and potentially higher critical temperatures in related compounds.

These results are only the starting point for the electrochemical synthesis method for bulk superconductors because the presented synthesis approach and compound family are extendable through some technical and chemical variations. With regard to the technical aspects, an additional water-cooling jacket could be added to the electrolysis chamber to reach constant and controllable reaction temperatures. Furthermore, a reference electrode could be inserted to record terminal voltages and actual electrode potentials to gain an even better reaction control. Additionally the starting material $\beta$-FeSe can be doped with other chalcogenides as well as longer chained alkylammonium salts can be utilized as supporting electrolyte.

The remaining part is about [(Li,Fe)OH]FeSe phases and the oxyhalide $CaFeO_2Cl$. They show that the recapture of known compound types is still a promising research field. Applying a low temperature solid-state synthesis to [(Li,Fe)OH]FeSe in contrast to the usually hydrothermal method led to the discovery of two new phases. These are $[(Li_{0.88}Fe_{0.12})OH]FeSe$ and $[LiOH](Fe)_zFeSe$. They expand the FeSe-based structure family. A possible explanation for elongation of the lattice parameter $c$ in $[LiOH](Fe)_zFeSe$ is given, but further structure investigations are necessary to validate the proposal. Regarding $CaFeO_2Cl$ the revisit of the know structure led to a thorough investigation of this Mott insulator with a proposed Néel-type magnetic ordering pattern. The outcome of this thesis demonstrates that there are still compounds left with yet unknown promising properties which only need to be (re)discovered.

# A Appendix

## A.1 Supporting Information of $(TMA)_{0.5}Fe_2Se_2$

### Powder X-Ray diffraction

Glass capillaries (0.3 mm in diameter, Hilgenberg GmbH) were filled with the samples and sealed. A Stoe Stadi-P diffracometer ($Mo_{K\alpha 1}$, Ge(111)-monochromator, Mythen 1k detector) was used to measure the patterns which were analysed and fitted using the Topas package.[1-2] After indexing the data with the SVD-algorithm, the space group *I*4/*mmm* was chosen.[3] Intensities were gathered using the Pawley method, and the structure was solved by charge-flipping.[1, 4-5] The trial structures were used in subsequent Rietveld refinements and visualized by the program Diamond.[6] Measurements at high temperatures performed on samples in silicia capillaries (diameter 0.5 mm, Hilgenberg GmbH, sealed with grease) on a Stoe Stadi-P diffractometer ($Mo_{K\alpha}$, Ge(111)-monochromator, IP-PSD detector) equipped with a graphite furnace. Data were visualized with WinXPOW.[7]

### DFT calculations

First-principles electronic structure calculations were performed using the Vienna ab initio simulation package (VASP 5.4.4)[8-9] based on density functional theory (DFT) and plane wave basis sets. Projector-augmented waves (PAW)[10] were used and contributions of correlation and exchange were treated using the strongly constrained and appropriately normed semi-local density functional (SCAN).[11] The *k*-space was sampled with the Monkhorst-Pack[12] scheme using an 11 × 11 × 11 grid based on the primitive unit cell. The AFLOW[13] utilities were used to transform between primitive and conventional unit cells, and FINDSYM[14] to determine the space group symmetry. Convergence criteria were $10^{-8}$ eV for the total energy and $10^{-4}$ eV/Å for the structural relaxations regarding ion positions, respectively, using a plane wave cut-off energy of 600 eV. The parameters of the fully relaxed structure of $(TMA)_{0.5}Fe_2Se_2$ in the space group $I\bar{4}2m$ are compiled in Table A-1.

**Table A-1.** Structure parameters of $(TMA)_{0.5}Fe_2Se_2$ (SG $I\bar{4}2m$) calculated with different functionals

| | $a$ (Å) | Δ % | $c$ (Å) | Δ % | $V$ (Å$^3$) | Δ % | $z_{SE}$ | Δ % | Fe-Se | Δ % | Se-Fe-Se | Δ % |
|---|---|---|---|---|---|---|---|---|---|---|---|---|
| Exptl. | 5.457 | | 20.377 | | 606.75 | | 0.3160 | | 2.352 | | 110.24 | |
| SCAN | 5.454 | -0.05 | 20.383 | 0.03 | 606.32 | -0.07 | 0.3203 | 1.36 | 2.403 | 2.18 | 110.62 | 0.35 |
| PBE | 5.393 | -1.16 | 20.7151 | 1.66 | 602.62 | -0.67 | 0.3175 | 0.47 | 2.365 | 0.55 | 105.04 | -4.71 |
| PBEsol | 5.260 | -3.60 | 20.0346 | -1.68 | 554.36 | -8.63 | 0.3180 | 0.62 | 2.306 | -1.97 | 110.55 | 0.28 |
| LDA | 5.189 | -4.91 | 19.3535 | -5.02 | 521.07 | -14.12 | 0.3178 | 0.58 | 2.256 | -4.06 | 111.88 | 1.48 |

The phonon dispersions and phonon DOS shown in Figure 2-7 were calculated from forces acting on displaced atoms in 2×2×2 supercells using PHONOPY[15] and plotted with the SUMO tools.[16] The structural parameters were previously optimized until all forces were smaller than $10^{-5}$ eV/Å and energy changes are below $10^{-9}$ eV. This fully relaxed structure was used to calculate the infrared absorptions using density functional perturbation theory (DFPT, Figure 2-7).

## Chemical analysis: EDS, CHN and infrared spectroscopy

CHN elemental analysis and energy-dispersive spectroscopy measurements (EDS) confirm the chemical composition $(TMA)_{0.5}Fe_2Se_2$ (see Tables A-2 and Table A-3). Figure A-1 shows the morphology of a crystallite after intercalation.

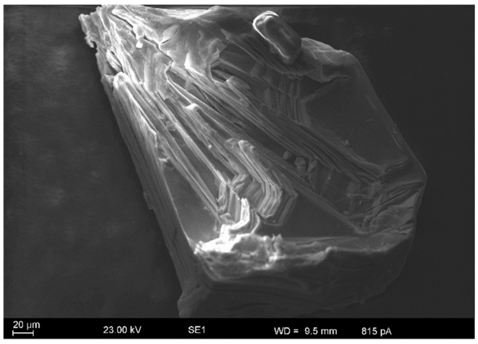

**Figure A-1**. SEM image of $(TMA)_{0.5}Fe_2Se_2$.

EDS measurments were performed on a Carl Zeiss Evo-Ma10 microscope with a Bruker Nano EDX detector (X-Flash detector 410 M). The controlling software is SmartSem for the detectors (SE and BSE)[17] and for the collections and evaluation of the spectra the program QUANTAX 200 was used.[18]

Any elements from the sample holder and the adhesive carbon pads were discounted. The CHN elemental analysis was single determined and therfore no standard deviations are given. FT-IR spectra were measured on a Bruker Vertex-80V FT-IR spectrometer ($\tilde{\nu}$ = 350 – 4000 $cm^{-1}$).

**Table A-2.** C:N:H ratios from elemental analysis normalized to N = 1.

| | C | H | N |
|---|---|---|---|
| **$(TMA)_{0.5}Fe_2Se_2$** | 4.1 | 13.1 | 1 |

**Table A-3.** Fe:Se ratio from EDS normalized to Se.

| | Fe | Se |
|---|---|---|
| **$(TMA)_{0.5}Fe_2Se_2$** | 1.1(1) | 1.0(1) |

## Magnetic susceptibility and dc resistivity measurements

Magnetic measurements of *β*-FeSe and $(TMA)_{0.5}Fe_2Se_2$ were carried out on a Physical Property Measurement System (PPMS-9, Quantum Design) with a vibrating sample magnetometer (VSM). Zero-field cooled and field-cooled measurements were conducted between 2 K and 100 K and an applied field of 15 Oe. The isothermal magnetization was measured at 2 K and 300 K ($H$ = ± 50 kOe). For the resistivity measurements, the samples were ground and pressed into pellets (diameter 5 mm, thickness ~ 0.8 mm). The pellets were contacted with the Wimbush press contact assembly for van der Pauw measurements.[18-19]

## Deintercalation of $(TMA)_{0.5}Fe_2Se_2$

A $(TMA)_{0.5}Fe_2Se_2$ sample was heated to 200 °C for 4 h under argon atmosphere. The residual black powder was analysed by powder diffraction and magnetic measurements. The powder pattern revealed single phase *β*-FeSe (see Figure A-2), thus $(TMA)_{0.5}Fe_2Se_2$ has been quantitatively deintercalated. Figure A-3 shows the ZFC/FC magnetic measurements the deintercalted sample.

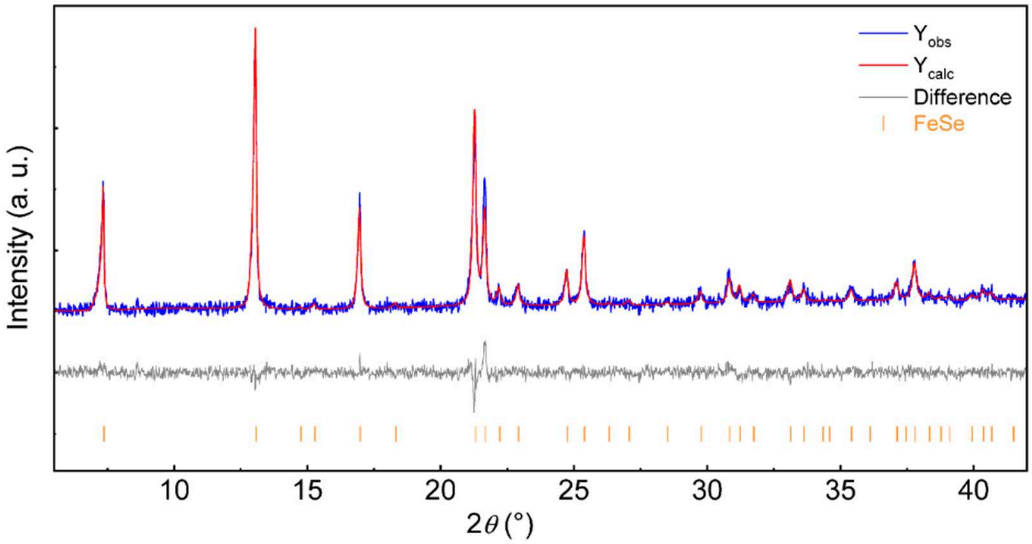

**Figure A-2.** PXRD pattern of the residue after heating at 200 °C with Rietveld fit (red) and difference curve (grey).

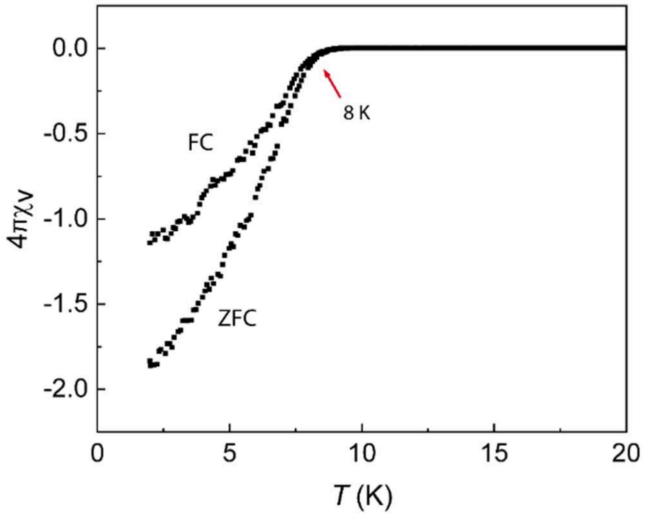

**Figure A-3.** Magnetic susceptibility of the residue after heating. FC is field cooled and ZFC is zero-field cooled.

## References

[1] A. Coelho, *TOPAS-Academic*, Version 4.1, Coelho Software, Brisbane, Australia, **2007**.

[2] A. Coelho, 6 ed., Coelho Software, Brisbane, Australia, **2016**.

[3] A. Coelho, *J. Appl. Crystallogr.* **2003**, *36*, 86–95.

[4] G. Pawley, *J. Appl. Crystallogr.* **1981**, *14*, 357–361.

[5] G. Oszlanyi, A. Suto, *Acta Crystallogr. Sec. A* **2008**, *64*, 123–134.

[6] K. Brandenburg, 3.2k ed., Crystal Impact GbR, Bonn, Germany, **2014**.

[7] Version 3.0.2.5 ed., STOE & Cie GmbH, Darmstadt, Germany, **2011**.

[8] G. Kresse, J. Furthmüller, *Phys. Rev. B* **1996**, *54*, 11169–11186.

[9] G. Kresse, J. Furthmüller, *Comput. Mater. Sci.* **1996**, *6*, 15–50.

[10] G. Kresse, D. Joubert, *Phys. Rev. B* **1999**, *59*, 1758–1775.

[11] J. Sun, A. Ruzsinszky, J. P. Perdew, *Phys. Rev. Lett.* **2015**, *115*, 036402.

[12] H. J. Monkhorst, J. D. Pack, *Phys. Rev. B* **1976**, *13*, 5188–5192.

[13] W. Setyawan, S. Curtarolo, *Comput. Mater. Sci.* **2010**, *49*, 299–312.

[14] H. T. Stokes, D. M. Hatch, *J. Appl. Crystallogr.* **2005**, *38*, 237–238.

[15] A. Togo, I. Tanaka, *Scripta Mater.* **2015**, *108*, 1–5.

[16] A. M. Ganose, A. J. Jackson, D. O. Scanlon, *Journal of Open Source Software* **2018**, *3*.

[17] Version 5.07 Beta ed., Carl Zeiss Microscopy Ltd., Cambridge, UK, **2014**.

[18] Version 1.9.4.3448 ed., Bruker Nano GmbH, Berlin, Germany, **2013**.

[19] Version 1.5.11 ed., Quantum Design Inc., San Diego, USA, **2013**.

# A.2 Supporting information of $[(Li_{0.88}Fe_{0.12})OH]FeSe$ and $[LiOH](Fe)_zFeSe$

## Crystallographic Data

**Table A-4.** Crystallographic data of $[(Li_{0.88}Fe_{0.12})OH]FeSe$ and $[LiOH](Fe)_zFeSe$ determined from PXRD data using Rietveld refinement.

| Chemical Formula | **$[(Li_{0.88}Fe_{0.12})OH]FeSe$** | **$[LiOH](Fe)_zFeSe$** |
|---|---|---|
| Crystal system, Space group | Tetragonal, *P*4/*nmm* O1 (no. 129) | Tetragonal, *P*4/*nmm* O1 (no. 129) |
| *T (K)* | 293 | 293 |
| *a* (Å), *c* (Å) | 3.80548(5), 9.3077(5) | 3.7774(4), *c* = 9.945(3) |
| $V$ *(Å³)* | 134.833(1) | 141.928(1) |
| *Z* | 2 | 2 |
| Radiation type | Mo-$K_{\alpha 1}$, $\lambda$ = 0.7093 Å | Cu-$K_{\alpha 1}$, $\lambda$ = 1.54056 Å |
| Diffractometer | Stoe Stadi P | Huber G670 |
| Monochromator | Ge-111 | Ge-111 |
| $R_p$ | 1.541 | 1.435 |
| $R_{wp}$ | 2.102 | 1.997 |
| GooF | 1.480 | 1.615 |

**Table A-5.** Atomic positions and displacement parameter $U_{iso}$ for $[(Li_{0.88}Fe_{0.12})OH]FeSe$

| **Atom** | ***x*** | ***y*** | ***z*** | **$U_{iso}$** | **occ** |
|---|---|---|---|---|---|
| Li | 0 | 0 | 0.043 | 0.050(15) | 0.879(5) |
| Fe1 | 0 | 0 | 0 | 0.05(11) | 0.121 |
| O | 0 | 1/2 | 0.076(12) | 0.022(9) | 1 |
| H | 0 | 1/2 | 0.18(3) | 0.05(9) | 1 |
| Fe2 | 0 | 0 | 1/2 | 0.056(2 | 1.000(2) |
| Se | 1/2 | 0 | 0.3405(5) | 0.0172(15) | 1 |

**Table A-6**. Selected bond distances (Å) and angles (°)for [($Li_{0.88}Fe_{0.12}$)OH]FeSe

| | | | |
|---|---|---|---|
| Li–O | 1.9228(8) | 2.1820(9) | |
| Fe1–O | 2.0173(9) | | |
| Fe2–Se | 2.4235(3) | | |
| φ O–Li–O | 164.1(8) | 121.6 (5) | 93.9(7) |
| φ O–Fe1–O | 139.2(4) | 96.96(5) | |
| φ Se–Fe2–Se | 112.1(1) | 104.2(3) | |

**Table A-7.** Atomic positions and displacement parameter $U_{iso}$ for [LiOH](Fe)$_z$FeSe

| **Atom** | ***x*** | ***y*** | ***z*** | $U_{iso}$ | **occ** |
|---|---|---|---|---|---|
| Li | 0 | 0 | 0.03(4) | 0.1(1) | 1.000(4) |
| Fe1 | 0 | 0 | 0 | 0.09(11) | 0 |
| O | 0 | 1/2 | 0.074(4) | 0.05(19) | 1 |
| H | 0 | 1/2 | 0.21(8) | 0.09(11) | 1 |
| Fe2 | 0 | 0 | 1/2 | 0.063(7) | 1.000(2) |
| Se | 1/2 | 0 | 0.3327(9) | 0.063(7) | 1 |

**Table A-8**. Selected bond distances (Å) and angles (°)for [LiOH](Fe)$_z$FeSe

| | | | |
|---|---|---|---|
| Li–O | 1.893(1) | 2.30(1) | |
| Fe2–Se | 2.4851(1) | | |
| φ O–Li–O | 169.9(2) | 109.6 (1) | 98.9(3) |
| φ Se–Fe2–Se | 115.1(1) | 98.7(1) | |

## Transmission electron microscopy (TEM) measurements

The transmission electron microscopy (TEM) measurements would be the ideal way to identify the crystal structure of both phases. TEM measurements were executed on a sample containing both main phases. The differences in the *c*-axis can only be determined via a different sample preparation. Due to the air instability, no distinction between the two phases could be accomplished and a complete high-resolution TEM was not possible, only the tetragonal structure could be validated (Figure A-4).

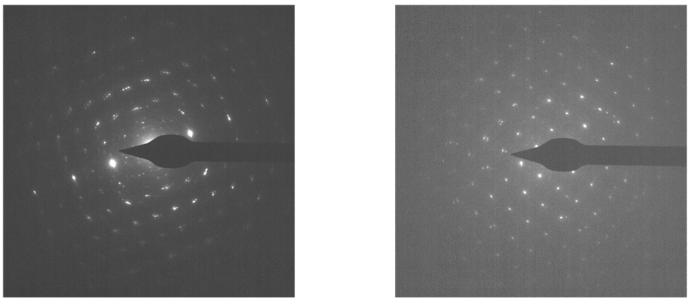

Figure A-4. Selected area diffraction pattern along [001].

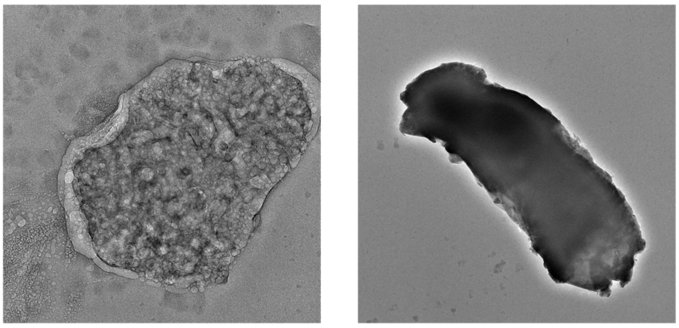

Figure A-5. Crystals chosen for EDS measurements Left: Oxidized crystal by air. Right: Still intact crystal.

EDS measurements were done on the various crystals but here it was also visible that some of the crystals were already oxidized (Figure A-5, left side). This was also noted in the values of the EDS measurements.

**Table A-9.** Fe : Se ratio from EDS analysis normalized to Se.

| | Fe | Se |
|---|---|---|
| $[(Li_{0.88}Fe_{0.12})OH]FeSe$ | 1.09(4) | 1.0(1) |
| $[LiOH](Fe)_zFeSe$ | 1.01(2) | 1.0(1) |

## Magnetic Properties

Figure A-7 and Figure A-8 shows the PXRD patterns of the magnetic measured samples. The samples contain the following impurities LiOH and $LiFeO_2$.

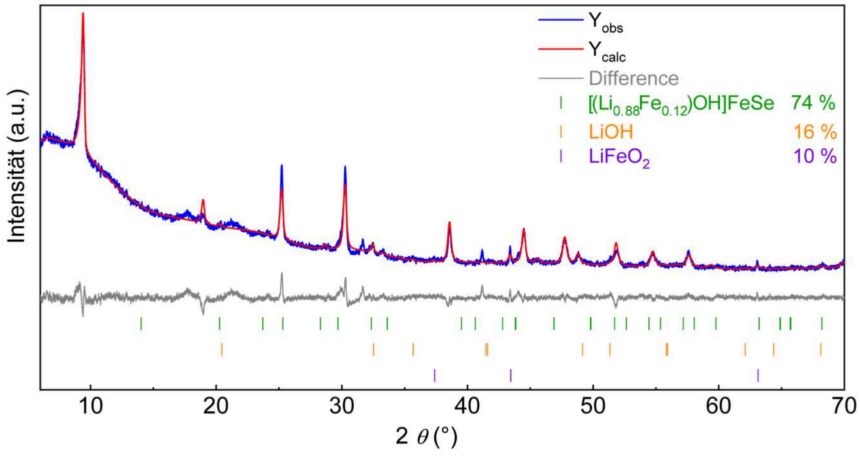

**Figure A-7.** PXRD pattern sample containing only [(Li$_{0.88}$Fe$_{0.12}$)OH]FeSe and LiOH and LiFeO$_2$ as side phases with Rietveld fit (red) and difference curve (grey).

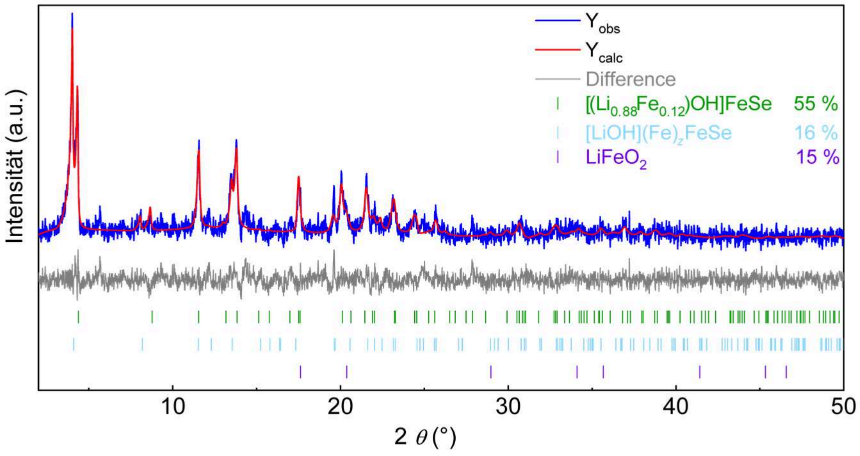

**Figure A-8.** PXRD pattern sample containing [Li$_{0.88}$Fe$_{0.12}$)OH]FeSe, [LiOH](Fe)$_z$FeSe and LiFeO$_2$ as side phase with Rietveld fit (red) and difference curve (grey).

Magnetic measurements for samples containing only the main phase [(Li$_{0.88}$Fe$_{0.12}$)OH]FeSe (Figure A-9) as well as measurements containing both phases were done (Figure 3-4). Isothermal magnetization curves at 300 and 1.9 K display small values of $\mu/\mu_B$ and show no hysteresis for both samples. The linearity of the inverse susceptibility in the sample with [(Li$_{0.88}$Fe$_{0.12}$)OH]FeSe and [LiOH](Fe)$_z$FeSe makes a paramagnetic ordered state probable. For the sample containing [(Li$_{0.88}$Fe$_{0.12}$)OH]FeSe and side phases, the inverse magnetic susceptibility curve is not linear. Therefore, no Curie-Weiss fit was done.

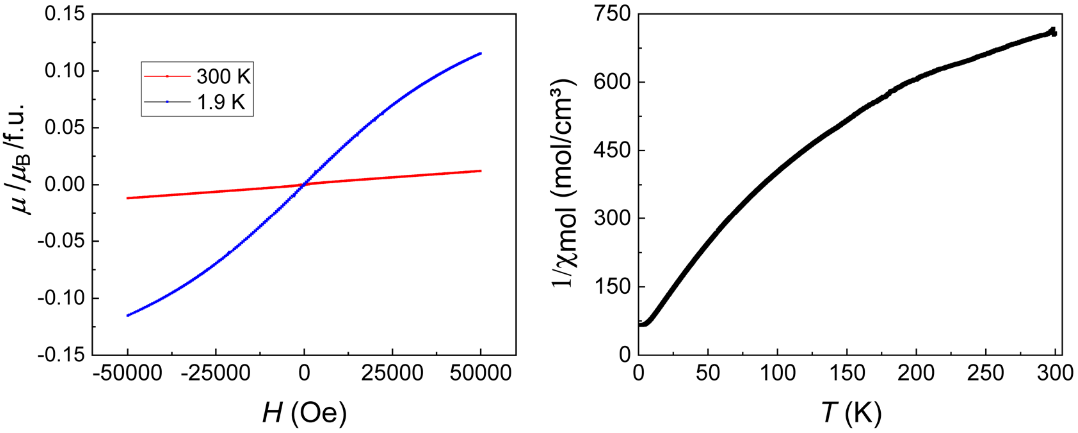

**Figure A-9.** Isothermal magnetization of $[(Li_{0.88}Fe_{0.12})OH]FeSe$ and side phases at 300 and 1.9 K (right) and inverse magnetic susceptibilities of $[(Li_{0.88}Fe_{0.12})OH]FeSe$ and side phases. $B = 3$ T.

## A.3 Crystallographic Data of $CaFeO_2Cl$

Table A-10, Table A-11 and Table A-12 show the data for the crystal structure solution of $CaFeO_2Cl$.

**Table A-10.** Crystal data, data collection parameters and refinement parameters for $CaFeO_2Cl$.

| **$CaFeO_2Cl$** | |
|---|---|
| **Crystal Data** | |
| Chemical formula | $CaFeO_2Cl$ |
| $M$ (g·mol$^{-1}$) | 163.37 |
| Crystal system, Space group (No.) | Monoclinic, $C2/m$ (no. 12) |
| $a$, $b$, $c$ (Å) | 9.969(2), 3.8105(8), 8.7350(17) |
| $\beta$ (°) | 103.62(3) |
| $V$ (Å$^3$), $\rho_{calc}$ (g·cm$^{-3}$) | 322.48(12), 3.365 |
| $T$ (K), $\mu$ (mm$^{-1}$) | 293, 6.851 |
| $Z$ | 4 |
| Radiation type | Mo-K$_\alpha$ ($\lambda$ = 0.71073 Å) |
| $\theta$ range (°) | 8.35–60.58 |
| **Data collection** | |
| Diffractometer, Monochromator | IPDS STOE |
| Absorption correction | Multi-scan *SADABS* 2014/5 |
| No. of reflections (measured, independent, with $I>3\sigma(I)$) | 1531, 507, 467 |
| $R_{int}$ | 0.0777 |
| Index range | $-13 \leq h \leq 13$, $-5 \leq k \leq 5$,$-12 \leq l \leq 12$ |
| $\theta$ range (°) | 4.207–29.746 |
| **Refinement** | |
| Refinement on | $F^2$ |
| Data, restraints, parameters, constraints | 507, 0, 31, 0 |
| $R_1$ ($I>2\sigma(I)$), $wR(F^2)$ ($I>2\sigma(I)$) | 0.0321, 0.0960 |
| Goodness of fit on $F^2$ | 1.224 |
| $\Delta\rho$ (max; min)(e· Å$^3$) | 0.92; −1.48 |

**Table A-11.** Fractional atomic coordinates, equivalent isotropic displacement parameters (Å$^2$) and site occupation for $CaFeO_2Cl$.

| **Atom** | ***x*** | ***y*** | ***z*** | $U_{eq}$ | **occ** |
|---|---|---|---|---|---|
| Fe1 | 0.13715(4) | 0 | 0.00029(6) | 0.0078(2) | 1 |
| Ca1 | 0.60820(7) | 0 | 0.29357(8) | 0.0104(3) | 1 |
| Cl1 | 0.33587(9) | 0 | 0.37571(11) | 0.0146(3) | 1 |
| O1 | 0.0239(2) | 0 | 0.1623(3) | 0.0087(5) | 1 |
| O2 | 0.6833(2) | 0 | 0.0542(3) | 0.0085(5) | 1 |

**Table A-12.** Atomic displacement parameters (Å$^2$) for $CaFeO_2Cl$.

| **Atom** | $U^{11}$ | $U^{22}$ | $U^{33}$ | $U^{12}$ | $U^{13}$ | $U^{23}$ |
|---|---|---|---|---|---|---|
| Fe1 | 0.0031(3) | 0.0066(3) | 0.0141(3) | 0 | 0.0029(2) | 0 |
| Ca1 | 0.0103(4) | 0.0078(4) | 0.0135(4) | 0 | 0.0032(3) | 0 |
| Cl1 | 0.0095(4) | 0.0171(5) | 0.0174(5) | 0 | 0.0033(3) | 0 |
| O1 | 0.0040(10) | 0.0100(14) | 0.0125(11) | 0 | 0.0026(9) | 0 |
| O2 | 0.0053(11) | 0.0048(13) | 0.0165(11) | 0 | 0.0049(9) | 0 |

## A.4 CCDC numbers

Crystallographic information files [CIF] of the investigated structures in this thesis have been deposited with the Cambridge Crystallographic Data Centre [CCDC]. Copies of the data can be obtained on quoting the depository numbers in Table A-13.

**Table A-13.** Deposition numbers for the Cambridge Crystallographic Data Centre.

| **Compound** | **Deposition Number** |
|---|---|
| $CaFeO_2Cl$ | 1957141 |
| $(TMA)_{0.5}Fe_2Se_2$ | 2052684 |

## A.5 Scientific Contributions

### Publications

**Magnetic and electronic properties of $CaFeO_2Cl$**

Bettina Rendenbach, Steffen Klenner, Rainer Pöttgen and Dirk Johrendt

*Zeitschrift für Naturforschung B* **2019**, *75*, 105-110.

**Bettina Rendenbach**: Conceptualization: Lead; Formal analysis: Lead; Investigation: Lead; Validation: Lead; Visualization: Lead; Writing – original draft: Lead; Writing –review & editing: Equal. **Steffen Klenner**: Formal analysis: Supporting; Investigation: Supporting; Validation: Supporting; Writing – original draft: Supporting; Writing – review & editing: Supporting.

**Rainer Pöttgen**: Formal analysis: Supporting; Investigation: Supporting; Validation: Supporting; Writing – original draft: Supporting; Writing – review & editing: Supporting.

**Dirk Johrendt**: Conceptualization: Equal; Formal analysis: Equal; Validation: Supporting; Funding acquisition: Lead; Project administration: Lead; Resources: Lead; Supervision: Lead; Visualization: Equal; Writing – original draft: Equal; Writing – review & editing: Equal.

**Temperature-dependent studies of exciton binding energy and phase-transition suppression in $(Cs,FA,MA)Pb(I,Br)_3$ perovskites**

Fabian Ruf, Meltem F. Aygüler, Nadja Giesbrecht, Bettina Rendenbach, Alice Magin, Pablo Docampo, Heinz Kalt and Michael Hetterich

*APL Materials* **2019**, *7*, 031113.

**Bettina Rendenbach**: Formal analysis: Supporting; Investigation: Supporting; Validation: Supporting; Writing – original draft: Supporting; Writing – review & editing: Supporting.

### Temperature and time-dependent luminescence of single crystals of $KTb_3F_{10}$

Patrick Pues, Florian Baur, Sebastian Schwung, Daniel Rytz, Rainer Pöttgen, Christian Paulsen, Oliver Janka, Bettina Rendenbach, Dirk Johrendt and Thomas Jüstel

*Journal of Luminescence* **2020**, *227*, 117523.

**Bettina Rendenbach**: Formal analysis: Supporting; Investigation: Supporting; Validation: Supporting; Writing – original draft: Supporting; Writing – review & editing: Supporting.

### Electrochemical synthesis and crystal structure of the organic ion intercalated superconductor $(TMA)_{0.5}Fe_2Se_2$ with $T_c = 43$ K

Bettina Rendenbach, Timotheus Hohl, Sascha Harm, Constantin Hoch and Dirk Johrendt

*Journal of the American Chemical Society* **2021**, *143*, 3043–3048.

**Bettina Rendenbach**: Conceptualization: Lead; Formal analysis: Lead; Investigation: Lead; Validation: Lead; Visualization: Lead; Writing – original draft: Lead; Writing –review & editing: Equal.

**Timotheus Hohl:** Conceptualization: Equal; Formal analysis: Supporting; Investigation: Supporting; Validation: Supporting; Writing – original draft: Supporting.

**Sascha Harm:** Conceptualization: Supporting; Formal analysis: Supporting; Investigation: Supporting; Validation: Supporting;

**Constantin Hoch**: Conceptualization: Equal; Formal analysis: Supporting; Investigation: Supporting; Validation: Supporting; Writing – original draft: Supporting. Writing – review & editing: Equal.

**Dirk Johrendt**: Conceptualization: Equal; Formal analysis: Equal; Validation: Supporting; Funding acquisition: Lead; Project administration: Lead; Resources: Lead; Supervision: Lead; Visualization: Equal; Writing – original draft: Equal; Writing – review & editing: Equal.

## Conference contributions

**Synthese und Charakterisierung von $CaFeO_2Cl$** [*talk*]

Bettina Rendenbach and Dirk Johrendt

*3. Obergurgl-Seminar Festkörperchemie*, Obergurgl, Austria, **2018**

**$CaFeO_2Cl$ – Zwischen Theorie und Praxis** [*talk*]

Bettina Rendenbach and Dirk Johrendt

*4. Obergurgl-Seminar Festkörperchemie*, Obergurgl, Austria, **2019**

**LiOHFeSe** [*talk*]

Bettina Rendenbach, Sebastian Ambach and Dirk Johrendt

*5. Obergurgl-Seminar Festkörperchemie*, Obergurgl, Austria, **2020**